HyGAL: Characterizing the Galactic ISM with observations of hydrides and other small molecules

II. The absorption line survey with the IRAM 30 m telescope

W.-J. Kim[1], P. Schilke[1], D. A. Neufeld[2], A. M. Jacob[2], Á. Sánchez-Monge[1], D. Seifried[1], B. Godard[3], K. M. Menten[4], S. Walch[1], E. Falgarone[5], V.S. Veena[4], S. Bialy[6], T. Möller[1], and F. Wyrowski[4]

[1] I. Physikalisches Institut, Universität zu Köln, Zülpicher Str. 77, 50937 Köln, Germany
   e-mail: `wonjukim@ph1.uni-koeln.de`
[2] William H. Miller III Department of Physics & Astronomy, Johns Hopkins University, Baltimore, MD 21218, USA
[3] LERMA, Observatoire de Paris, PSL Research University, CNRS, Sorbonne Universités, F-75014 Paris, France
[4] Max-Planck-Institut für Radioastronomie, Auf dem Hügel 69, 53121 Bonn, Germany
[5] Laboratoire de Physique de l'ENS, ENS, Université PSL, CNRS, Sorbonne Université, Université de Paris, 24 rue Lhomond, 75005 Paris, France
[6] Department of Astronomy, University of Maryland, College Park, MD 20742-2421, USA

ABSTRACT

As a complement to the HyGAL Stratospheric Observatory for Infrared Astronomy Legacy Program, we report the results of a ground-based absorption line survey of simple molecules in diffuse and translucent Galactic clouds. Using the Institut de Radioastronomie Millimétrique (IRAM) 30 m telescope, we surveyed molecular lines in the 2 mm and 3 mm wavelength ranges toward 15 millimeter continuum sources. These sources, which are all massive star-forming regions located mainly in the first and second quadrants of the Milky Way, form the subset of the HyGAL sample that can be observed by the IRAM 30 m telescope. We detected HCO$^+$ absorption lines toward 14 sightlines, toward which we identified 78 foreground cloud components, as well as lines from HCN, HNC, C$_2$H, and c-C$_3$H$_2$ toward most sightlines. In addition, CS and H$_2$S absorption lines are found toward at least half of the continuum sources. The spectral line data obtained were analyzed to characterize the chemical and physical properties of the absorbing interstellar medium statistically. The column density ratios of the seven molecular species observed are very similar to values found in previous absorption line studies carried out toward diffuse clouds at high latitudes. As expected, the C$_2$H and c-C$_3$H$_2$ column densities show a tight correlation with that of N(HCO$^+$), because of these all these molecules are considered to be proxies for the H$_2$ column density toward diffuse and translucent clouds. The HCN and HNC column densities, by contrast, exhibit nonlinear correlations with those of C$_2$H, c-C$_3$H$_2$, and HCO$^+$, increasing rapidly at $A_\mathrm{v} \approx 1$ in translucent clouds. Static Meudon photodissociation region (PDR) isobaric models that consider ultraviolet-dominated chemistry were unable to reproduce the column densities of all seven molecular species by just a factor of a few, except for H$_2$S. The inclusion of other formation routes driven by turbulent dissipation could possibly explain the observed high column densities of these species in diffuse clouds. There is a tentative trend for H$_2$S and CS abundances relative to H$_2$ to be larger in diffuse clouds (X(H$_2$S) and X(CS) $\sim 10^{-8} - 10^{-7}$) than in translucent clouds (X(H$_2$S) and X(CS) $\sim 10^{-9} - 10^{-8}$) toward a small sample; however, a larger sample is required in order to confirm this trend. The derived H$_2$S column densities are higher than the values predicted from the isobaric PDR models, suggesting that chemical desorption of H$_2$S from sulfur-containing ice mantles may play a role in increasing the H$_2$S abundance.

Key words. astrochemistry – techniques: spectroscopic – ISM: molecules

1. Introduction

Our understanding of the interstellar medium (ISM) has significantly improved in the past decade, through extensive observational efforts in absorption line spectroscopy performed at millimeter (mm) and submillimeter (submm) wavelengths toward background continuum sources. These observations have revealed both physical complexity and chemical richness as evidenced by the detection of various diatomic (e.g., CN, CO; Liszt & Lucas 2001; Liszt et al. 2019), triatomic, and even polyatomic molecules (e.g., C$_3$H$^+$, CH$_2$, H$_2$O, HCO$^+$, C$_2$H, c-C$_3$H, l-C$_3$H, HCN, HNC, CH$_3$CN, NH$_3$, H$_2$CO, and c-C$_3$H$_2$; Polehampton et al. 2005; Flagey et al. 2013; Gerin et al. 2011, 2019; Godard et al. 2010; Liszt et al. 2006, 2014, 2018). The ISM has been shown to consist of multiphase gas combining a cold neutral medium (CNM) and warm neutral medium (WNM) (Bialy & Sternberg 2019; Bellomi et al. 2020) in diffuse clouds where chemistry begins with the formation of simple molecules. These diffuse clouds contain CO-dark H$_2$ gas, in which CO is not detected in emission, but it can still be detected at a low abundance in absorption. Thus, diffuse clouds (defined as those in which the local fraction of gas-phase carbon in C$^+$, $f_{\mathrm{C}^+}^n$, exceeds 0.5) and translucent clouds (defined as those in which $f_{\mathrm{C}^+}^n < 0.5$ but the local fraction of gas-phase carbon in CO, f_{CO}^n, remains less than 0.9) in the Milky Way are excellent laboratories to study the formation and destruction of molecular clouds. The very different conditions in dense molecular clouds, where eventually star formation occurs, lead to a substantially different molecular composition. Significant efforts have been undertaken to determine

the physical parameters that characterize the gas properties of high latitude diffuse clouds and solar neighborhood clouds (e.g., Liszt & Lucas 2001, 2004; Lucas & Liszt 2000, 2002) as well as for a few specific sightlines in the Galactic plane (e.g., Godard et al. 2010; Gerin et al. 2011; Neufeld et al. 2015). In contrast to high latitude clouds, the ISM in the disk of the Milky Way has many more complicated structures of atomic and molecular gas. Differing in their physical and chemical properties, diffuse and translucent clouds have, for example, different molecular gas fractions and different abundances of carbon-bearing species (see Snow & McCall 2006, and references therein). In particular, if only the total visual extinction (A_v) is known, distinguishing translucent clouds from the superposition of multiple diffuse clouds yielding similar fractions of integrated column densities for atomic (f_H^N) or molecular ($f_{H_2}^N$) hydrogen is not straightforward. Nonetheless, the chemistry in the two types of clouds is certainly different as the primary reservoirs of gas-phase carbon vary from diffuse clouds to translucent clouds.

Absorption lines of HCO^+ sample low-density regions, which can neither be observed in molecular emission nor in CO millimeter absorption because of both low excitation and the absence of CO (Hogerheijde et al. 1995; Liszt et al. 2018, 2019), making them an excellent tracer of H_2 (Gerin et al. 2019) that is not directly detectable except through ultraviolet (UV) observations toward nearby hot stars in very diffuse clouds. At millimeter and submillimeter wavelengths, where observations are unaffected by dust absorption, background sources (and foreground clouds) can be observed at large distances within the Galactic plane, and at higher visual extinctions, that are higher column densities. As carbon is a key element in interstellar chemistry, we also explored absorption by carbon-bearing molecules (HCN, HNC, C_2H, and $c-C_3H_2$) that have been observed to be surprisingly as abundant (e.g., Godard et al. 2010; Gerin et al. 2011) as HCO^+ in diffuse and translucent clouds. Their observed abundances are much higher than predicted from simple photodissociation region (PDR) models (e.g., Godard et al. 2010; Gerin et al. 2011).

The unexpectedly large column densities and broad line widths of the HCO^+ and HCN molecules observed at millimeter wavelengths can be explained by their formation being enhanced by the dissipation of interstellar turbulence; this creates small regions of elevated temperature and large ion-neutral drift that enables endothermic reactions not possible under the standard conditions typical of the CNM (e.g., Hogerheijde et al. 1995; Godard et al. 2010, 2014). For similar reasons, the observed abundances of sulfur-bearing molecules (such as H_2S, CS, SO, and SH) greatly exceed values predicted by standard models of cold diffuse molecular clouds, providing further evidence for the enhancement of endothermic reaction rates by elevated temperatures or ion-neutral drift (Neufeld et al. 2015). Therefore, observations of these molecules provide important constraints on shock and turbulent dissipation region (TDR) models.

By combining observations of multiple species, examining correlations and measuring abundance ratios, it has been possible to determine the distribution function for the H_2 fraction within the diffuse and translucent ISM. This provides an important constraint on global models for the formation and destruction of molecular hydrogen in a turbulent medium (e.g., Bialy et al. 2017, 2019; Bialy & Burkhart 2020), as the differing abundances and kinematics of these molecules studied here demonstrate the importance of considering gas dynamical processes that enhance the formation rate of some of their progenitor species.
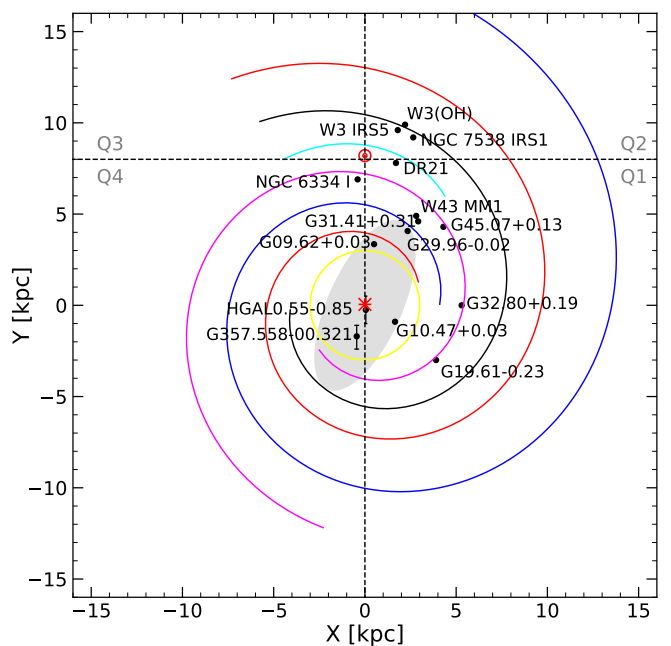
Fig. 1: Positions of fifteen sightlines (black dots with names) from the HyGAL program in the Galactic plane. This distribution plot is reproduced based on the Figure 3 of Paper I. Colored curves represent different Milky Way spiral arms; the 3-kpc arm is in yellow, the Norma and outer arms are in red, the Scutum-Centaurus arm is in blue, the Sagittarius-Carina arm is in purple, the Perseus arm is in black, and the local arm is in cyan. The Sun and the Galactic center (GC) are marked with the red Sun and asterisk symbols, respectively. The gray-shaded ellipse around the GC represents the long bar.

This paper presents an absorption line survey, in the 2 mm and 3 mm wavelength regions, carried out using the Institut de Radioastronomie Millimétrique (IRAM) 30 m telescope, as a complement to the HyGAL Stratospheric Observatory for Infrared Astronomy (SOFIA) Legacy Program (see Jacob et al. 2022, hereafter Paper I, for an overview of the HyGAL program) that surveys six hydride species (i.e., ArH^+, OH^+, H_2O^+, SH, OH, and CH), C^+, and O toward 25 bright Galactic continuum background sources at submillimeter wavelengths. This millimeter absorption line program surveys 15 sightlines targeted by the HyGAL program. Here we will explore the absorption line data and investigate associations between simple molecules and the hydrides studied in Paper I. Section 2 describes the acquisition of the spectroscopic data, and the calibration and data reduction procedures employed. In Sect. 3, we present the spectra of lines from HCO^+, HCN, HNC, CS, H_2S, C_2H, and $c-C_3H_2$ that are detected in absorption toward the different sightlines; here we discuss both their general properties and the CO emission counterparts that have previously been observed along some of these sightlines. The determination of the column densities of these molecular species will be explained in Sect. 4, together with a principal component analysis for all species reported both in this paper and in Paper I toward W3(OH) and W3 IRS5. In Sect. 5, we discuss the results of the principal component analysis and the derived observational quantities (column densities and abundances), and we compare these measurements with the results of isobaric PDR models, trying to understand the chemical and physical properties of diffuse and translucent clouds across the

Table 1: Source summary.

Source	R.A. (J2000) (hh:mm:ss)	Dec. (J2000) (dd:mm:ss)	Gal. Long. (deg)	Gal. Lat. (deg)	d (kpc)	R_{GAL} (kpc)	v_{sys} (km s^{-1})
W3 IRS5	02:25:40.5	+62:05:51.4	133.715	+1.215	2.3	9.9	−39.0
W3(OH)	02:27:04.1	+61:52:22.1	133.948	+1.064	2.0	9.6	−47.0
NGC 6334 I	17:20:53.4	−35:47:01.5	351.417	+0.645	1.3	7.0	−7.6
HGAL0.55−0.85	17:50:14.5	−28:54:30.7	0.546	−0.851	7.7−9.2	0.4−1.0	17.5
G09.62+0.19	18:06:14.9	−20:31:37.0	9.620	+0.194	5.2	3.1	4.4
G10.47+0.03	18:08:38.4	−19:51:52.0	10.472	+0.026	8.6	1.6	66.9
G19.61−0.23	18:27:38.0	−11:56:39.5	19.608	−0.234	12.6	4.4	41.8
*G29.96−0.02	18:46:03.7	−02:39:21.2	29.954	−0.016	4.8	4.7	97.0
*W43 MM1	18:47:47.0	−01:54:28.0	30.817	−0.057	3.1	5.7	98.0
*G31.41+0.31	18:47:34.1	−01:12:49.0	31.411	+0.307	3.7	5.4	97.0
*G32.80+0.19	18:50:30.6	−00:02:00.0	32.796	+0.191	9.7	5.3	15.0
*G45.07+0.13	19:13:22.0	+10:50:54.0	45.071	+0.133	7.8	6.1	60.0
DR21	20:39:01.6	+42:19:37.9	81.681	+0.537	1.5	7.4	−3.0
NGC 7538 IRS1	23:13:45.3	+61:28:11.7	111.542	+0.777	2.6	9.8	−59.0
G357.558−00.321	17:40:57.2	−31:10:59.3	357.557	−0.321	9.0−11.8	1.0−3.6	5.3

Notes. Except for the sources whose names are preceded by an asterisk, heliocentric and galactocentric distances are the values listed by Paper I. For those five sources, revised distances are taken from Reid et al. (2019), who cite the primary references. The systemic velocity, v_{sys}, refers to the velocity at which the H^{13}CO$^+$ emission line peaks, for each source in our sample as per the observations presented here.

Milky Way. Finally, we conclude and summarize all the results from this study in Sect. 6.
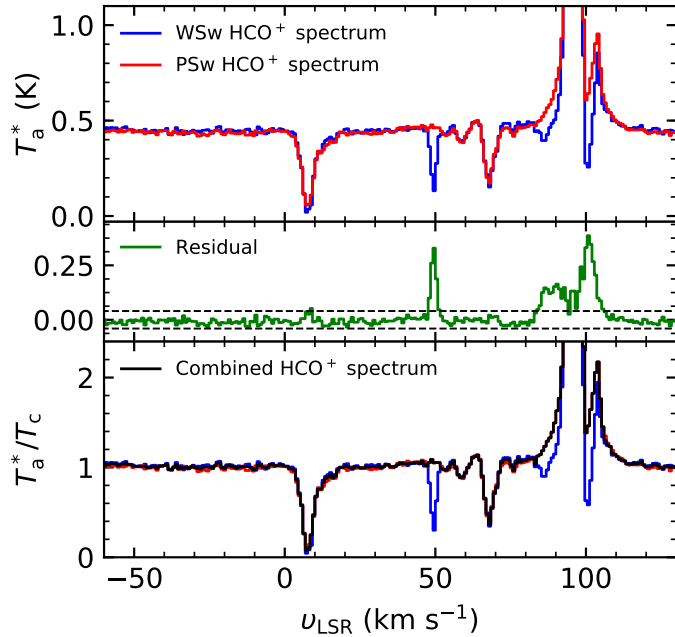
Fig. 2: Comparison of the HCO$^+$ spectra from observations with wobbler switching and position switching modes. The top panel shows the HCO$^+$ spectra (velocities relative to the local standard of rest, LSR) taken with WSw (blue) and PSw (red) modes toward G29.96−0.02. The middle panel shows the residual spectrum (green) after fitting the WSw and PSw spectra. Black horizontal dashed lines mark the 3 rms level. The bottom panel presents the combined spectrum (black) of the WSw and rescaled PSw (AT_a^*(PSw) + B, where A and B are the slope and y-intercept of a linear least-squares regression fit, respectively), with the individual WSw and PSw spectra in the same colors as in the top panel.

2. Observations and data reduction

We carried out observations of a molecular absorption line survey (Project ID: 003–20) in the 2 mm and 3 mm wavelength regions, during the period of 2020 June 23−30, with the Eight MIxer Receiver (EMIR)[1] on the IRAM 30 m telescope, toward the 15 HyGAL continuum sources listed in Table 1. The continuum sources observed here cover slightly more than half of the entire HyGAL source sample (see Paper I) and are mostly located in the first and second quadrants of the Milky Way as shown in Fig. 1, except for two sources, NGC6334 I and G357.558−00.321, which are located in the fourth quadrant. For a given column density of a target species, the signal-to-noise ratio for absorption line features is proportional to the continuum flux at the relevant wavelength. The Herschel InfraRed Galactic Plane Survey (Hi-GAL, Molinari et al. 2016) provides a compact source catalog (Elia et al. 2017, 2021) with continuum fluxes at 70, 160, 250, 350, and 500 μm coinciding with the wavelengths of transitions targeted with HyGAL (approximately spanning 149–494 μm). The HyGAL program selected 25 submillimeter sources with flux limits over 2000 Jy at 160 μm for sources in the inner Galaxy and > 1000 Jy for sources in the outer Galaxy (see Paper I for more details on the source selection).

The observations were done with two different receiver setups: the first configuration combines the E090 and E150 receivers (covering 92−99.7 GHz and 166.5−174.2 GHz) and the other uses the E090 receiver alone (covering 83.2−90.9 GHz and 98.9−106.6 GHz). These setups allowed us to target a number of molecular transitions with a total bandwidth coverage of 15 GHz (including a 1 GHz bandwidth overlap between the two setups); they proved ideal for obtaining widespread absorption line features arising from foreground clouds at different velocities. Both receiver setups are connected to the FTS200 backend offering a frequency channel resolution of 200 kHz (equivalent to $\Delta v \sim 0.35$ km s^{-1} for H$_2$S and 0.62−0.66 km s^{-1} for the other transitions). For our analysis, we resampled all the spectral line data to a fixed velocity resolution of 0.8 km s^{-1}, except H$_2$S for

Table 2: Observed molecular transitions.

Molecule	Transition	Rest Frequency (GHz)	Beam Size ($''$)	E_u/k (K)	E_l/k (K)	A_{ul} (s^{-1})
HCO$^+$	$J = 1 \leftarrow 0$	89.1885	27.6	4.28	0.0	4.19×10^{-5}
HCN	$J = 1 \leftarrow 0, F = 1 \leftarrow 1$	88.6304	27.8	4.25	0.0	2.41×10^{-5}
	$J = 1 \leftarrow 0, F = 2 \leftarrow 1^\dagger$	88.6318	27.8	4.25	0.0	2.41×10^{-5}
	$J = 1 \leftarrow 0, F = 0 \leftarrow 1$	88.6339	27.8	4.25	0.0	2.41×10^{-5}
HNC	$J = 1 \leftarrow 0$	90.6635	27.1	4.35	0.0	2.69×10^{-5}
CS	$J = 2 \leftarrow 1$	97.9809	25.1	7.05	2.35	1.68×10^{-5}
H$_2$S	$J_{K_a,K_c} = 1_{1,0} \leftarrow 1_{0,1}$	168.7627	14.6	8.10	0.0	2.68×10^{-5}
C$_2$H	$N = 1 \leftarrow 0, J = 3/2 \leftarrow 1/2, F = 1 \leftarrow 1$	87.2841	28.2	4.19	0.0	2.60×10^{-7}
	$N = 1 \leftarrow 0, J = 3/2 \leftarrow 1/2, F = 2 \leftarrow 1^\dagger$	87.3168	28.2	4.19	0.0	1.53×10^{-6}
	$N = 1 \leftarrow 0, J = 3/2 \leftarrow 1/2, F = 1 \leftarrow 0$	87.3285	28.2	4.19	0.0	1.27×10^{-6}
	$N = 1 \leftarrow 0, J = 1/2 \leftarrow 1/2, F = 1 \leftarrow 1$	87.4019	28.1	4.20	0.0	1.27×10^{-6}
	$N = 1 \leftarrow 0, J = 1/2 \leftarrow 1/2, F = 0 \leftarrow 1$	87.4071	28.1	4.20	0.0	1.54×10^{-6}
	$N = 1 \leftarrow 0, J = 1/2 \leftarrow 1/2, F = 1 \leftarrow 0$	87.4464	28.1	4.20	0.0	2.61×10^{-7}
c-C$_3$H$_2$	$J_{K_a,K_c} = 2_{1,2} \leftarrow 1_{0,1}$	85.3388	28.8	4.10	0.0	2.32×10^{-5}

Notes. The dagger ($\dagger$) marks the reference frequency corresponding to the reference velocity (v_{sys}) for a given sightline. The spectroscopic information on these transitions is taken from Jet Propulsion Laboratory (JPL)[a] and the Cologne Database for Molecular Spectroscopy (CDMS)[b] catalogs. The frequencies of H$_2$S and c-C$_3$H$_2$ transitions correspond to that of their ortho spin state, and so the subsequently derived column densities and abundances for these species refer to ortho-H$_2$S and ortho-c-C$_3$H$_2$. The upper energy levels of ortho-H$_2$S and ortho-c-C$_3$H$_2$ listed in the table are relative to the ground state of the orhto species; without that, for ortho-H$_2$S, $E_u/k = 27.88$ K and $E_l/k = 19.78$ K, and for ortho-c-C$_3$H$_2$, $E_u/k = 6.45$ K and $E_l/k = 2.35$ K.

[a] https://spec.jpl.nasa.gov
[b] https://cdms.astro.uni-koeln.de

Table 3: Coefficients from linear regression fits.

Source	HCO$^+$		HCN		HNC		CS		H$_2$S		C$_2$H		c-C$_3$H$_2$	
	A	B	A	B	A	B	A	B	A	B	A	B	A	B
W3 IRS5	0.977	−0.225	0.963	−0.199	0.942	−0.218		···	···	···	0.944	−0.217	0.800	−0.128
W3(OH)	1.163	−0.441	0.960	−0.281	0.856	−0.280		···	···	···	0.869	−0.168	0.620	0.005
NGC 6334 I	0.605	−2.148	0.716	−2.538	0.670	−2.438	···	···	···	···	0.454	−1.577	0.520	−1.904
HGAL0.55−0.85	···	···	···	···	···	···	···	···	···	···	···	···	···	···
G09.62+0.19	0.987	−1.133	1.033	−1.188	1.015	−1.145	···	···	···	···	0.486	−0.539	0.156	−0.126
G10.47+0.03	1.013	−0.047	1.037	−0.043	0.896	−0.014	···	···	···	···	0.907	−0.033	0.907	−0.021
G19.61−0.23	1.049	0.867	1.050	0.862	1.024	0.887	···	···	···	···	0.889	0.836	0.819	0.807
G29.96−0.02	0.976	−0.681	0.969	−0.663	0.942	−0.644	0.580	−0.235	0.112	−0.028	0.922	−0.633	0.928	−0.655
W43 MM1	0.626	−0.185	0.749	−0.229	0.628	−0.185	0.763	−0.038	0.700	0.184	0.809	−0.264	0.891	−0.288
G31.41+0.31	1.018	0.098	1.042	0.089	0.902	0.099	0.977	−0.117	0.942	−0.228	1.029	0.080	1.074	0.073
G32.80+0.19	1.075	−0.015	1.072	−0.005	1.100	−0.323	0.931	0.212	0.592	0.421	1.080	−0.287	1.031	−0.238
G45.07+0.13	0.946	0.193	0.906	0.184	0.260	0.199	···	···	···	···	0.930	0.212	0.625	0.220
DR21	0.847	−0.322	0.851	0.293	0.919	−0.505	···	···	···	···	0.906	0.220	1.010	−0.306
NGC 7538 IRS1	0.761	0.224	0.932	0.238	0.536	0.283	···	···	···	···	0.761	0.225	0.278	0.342

Notes. The coefficients A and B refer to the slope and y-intercept of a linear least-square regression fit. The molecular transitions with blank A and B values correspond to WSw mode-only observations with noncontaminated WSw off positions.

which we use a better resampled resolution of 0.36 km s^{-1}. We utilized the Continuum and Line Analysis Single-dish Software (CLASS) software[2] of the Grenoble Image and Line Data Analysis Software (GILDAS) package (Pety 2005) for the initial data reduction of the molecular line data, and further post-processed the data using Python (e.g., when combining the observations made in two different switching modes).

2.1. Calibration for PSw and WSw mode observations

The observed data sets consist of wobbler switching (WSw) and position switching (PSw) On-Off mode observations. For WSw mode observations, all sources were observed with throw angles of ±120$''$. In active star-forming regions, which often exhibit ex-

tended emission structures, these relatively small throw angles can result in reference positions that are significantly contaminated by emission in the stronger lines such as HCO$^+$ (1→0). This causes artificial absorption features in the final calibrated spectra. On the other hand, standing waves are often generated in the PSw mode as the telescope slews to distant reference positions while the WSw mode provides reliable continuum level measurements and flat baselines. Since standing waves distort the emission and absorption line profiles, we carefully investigated all the PSw spectra and excluded those scans that are severely affected by standing wave effects before averaging all observational scans.

Figure 2 shows an example of the HCO$^+$ spectra obtained with WSw and PSw mode observations toward G29.96−0.02. In the top panel of Fig. 2, the WSw spectrum shows additional apparent absorption features; these are found, for example, at LSR velocities of 50 km s^{-1} and 85 km s^{-1}, the latter lying close to

[2] https://www.iram.fr/IRAMFR/GILDAS/doc/html/class-html/class.html

Table 4: Continuum levels and rms noise of the spectra.

Source	HCO$^+$		HCN		HNC		CS		H$_2$S		C$_2$H		c-C$_3$H$_2$	
	T_c (K)	T_{rms} (K)	T_c (K)	T_{rms} (K)	T_c (K)	T_{rms} (K)	T_c (K)	T_{rms} (K)	T_c (K)	T_{rms} (K)	T_c (K)	T_{rms} (K)	T_c (K)	T_{rms} (K)
W3 IRS5	0.525	0.007	0.514	0.008	0.509	0.007	0.418	0.005	0.181	0.012	0.566	0.010	0.606	0.008
W3(OH)	0.626	0.006	0.626	0.009	0.647	0.008	0.589	0.005	0.551	0.011	0.638	0.009	0.629	0.009
NGC 6334 I	0.427	0.010	0.531	0.013	0.464	0.014	0.677	0.017	1.031	0.048	0.455	0.014	0.438	0.013
HGAL0.55−0.85	0.116	0.008	0.111	0.008	0.116	0.009	0.141	0.006	0.257	0.014	0.112	0.009	0.109	0.009
G09.62+0.19	0.075	0.008	0.073	0.008	0.077	0.009	0.075	0.005	0.098	0.013	0.076	0.009	0.076	0.009
G10.47+0.03	0.117	0.006	0.122	0.009	0.121	0.008	0.159	0.005	0.367	0.015	0.115	0.011	0.115	0.007
G19.61−0.23	0.353	0.004	0.353	0.007	0.366	0.006	0.384	0.005	0.325	0.011	0.370	0.006	0.379	0.006
G29.96−0.02	0.439	0.004	0.439	0.008	0.458	0.007	0.390	0.008	0.182	0.024	0.456	0.007	0.472	0.007
W43 MM1	0.059	0.004	0.059	0.009	0.069	0.005	0.116	0.010	0.256	0.024	0.065	0.006	0.060	0.005
G31.41+0.31	0.155	0.006	0.155	0.009	0.158	0.006	0.167	0.006	0.271	0.013	0.167	0.008	0.161	0.007
G32.80+0.19	0.497	0.004	0.486	0.007	0.506	0.008	0.480	0.003	0.330	0.008	0.516	0.008	0.523	0.007
G45.07+0.13	0.194	0.004	0.194	0.005	0.201	0.006	0.191	0.004	0.183	0.011	0.199	0.005	0.198	0.005
DR21	1.500	0.005	1.490	0.009	1.496	0.009	1.540	0.006	0.751	0.012	1.563	0.008	1.590	0.008
NGC 7538 IRS1	0.408	0.005	0.401	0.008	0.415	0.008	0.387	0.005	0.369	0.011	0.406	0.009	0.402	0.008

Notes. The continuum and rms noise levels are on the T_a^* scale, with a spectral resolution (Δv) of 0.8 km s^{-1} for all species except for H$_2$S for which Δv =0.36 km s^{-1}.

Table 5: Summary of detected species in absorption.

Source	HCO$^+$	HCN	HNC	CS	H$_2$S	C$_2$H	c-C$_3$H$_2$
W3 IRS5	Y	Y	N	N	N	Y	Y
W3(OH)	Y	Y	Y	Y	Y	Y	Y
NGC 6334 I	Y	Y	Y	N	N	Y	Y
HGAL0.55−0.85	Y	N	N	N	N	N	N
G09.62+0.19	Y	Y	Y	N	Y	Y	N
G10.47+0.03	Y	Y	Y	Y	C	Y	C
G19.61−0.23	Y	Y	Y	Y	Y	Y	Y
G29.96−0.02	Y	Y	Y	Y	C	Y	Y
W43 MM1	Y	Y	Y	C	C	Y	N
G31.41+0.31	Y	Y	Y	Y	C	Y	Y
G32.80+0.19	Y	Y	Y	Y	Y	Y	Y
G45.07+0.13	Y	Y	Y	Y	Y	Y	Y
DR21	Y	Y	Y	Y	Y	Y	Y
NGC 7538 IRS1	Y	N	N	N	N	N	N

Notes. Clear detection of absorption features, which are either widely separated from the emission lines associated with background continuum sources or superposed on emission features, are marked with "Y". Less secure detections, due to either poor S/N or severe contamination from unidentified or identified transitions, are marked with "C" and nondetections with "N".

the velocity of the background continuum source (97 km s^{-1}). These components are not detected in the PSw spectrum, implying that they may be dismissed as artifacts arising from contamination in the reference position. To identify such artifacts, we rescaled the PSw spectrum to the WSw spectrum, allowing for both multiplicative and additive offsets, by using the relationship of AT_a^*(PSw) + B, where A and B are constants, representing the slope and y-intercept, respectively, of the linear least-squares regression on both the spectra. We note that there are some values of A that are lower than 1, which may be caused by the significant contamination from the WSw reference positions or the less flat baselines from the PSw modes. The coefficients used for rescaling the PSw spectra are listed in Table 3. We have examined if any excessive residual spectral features remain after subtracting a rescaled PSw spectrum from a WSw spectrum, as shown in the green profile in the middle panel of Fig. 2. If the residual value in any velocity channel exceeds three times the rms value (marked by black horizontal dashed lines), the WSw value at the selected velocity channel is replaced by the PSw value at the same velocity because the high residual components are regarded not to be real but due to the reference position contamination. The continuum levels and rms noise of

the spectra for the seven species toward each source are listed in Table 4. Subsequently, we combined the rescaled PSw and the WSw spectra corrected to exclude the WSw spectral range with the counterfeit absorption features. Since the WSw mode was used as the primary observing mode, observations made in this mode have a longer integration time (about 1.5 hours per source) and in turn a larger number of scans than observations taken in the PSw mode. Thus, before combining both data sets, the spectra are weighted by the inverse squares of their measured rms noise levels. The plot in the bottom panel shows the combined spectrum in black along with the WSw and PSw spectra in blue and red, respectively. The combined spectrum appears to be well-calibrated, with a higher signal-to-noise ratio than spectra obtained in the individual modes, and without any false absorption features (like the 50 km s^{-1} component). We used the combined spectra of all observed transitions in all following analyses.

Table 6: Summary of identified spiral arms and their velocity ranges along to the observed sightlines.

Source	Local	Aquila-Rift	Perseus	Sagittarius-Carina	Scutum-Centaurus	3-kpc (Galactic bar/center)	Inter-arm	Unidentified clouds or envelope
	(km s^{-1})	(km s^{-1})	(km s^{-1})	(km s^{-1})	(km s^{-1})	(km s^{-1})	(km s^{-1})	(km s^{-1})
W3 IRS5	−11.8, 3.6	⋯	−35.8, −16.1	⋯	⋯	⋯	⋯	⋯
W3(OH)	−16.0, 3.6	⋯	−35.6, −16.0	⋯	⋯	⋯	⋯	⋯
NGC 6334 I	⋯	⋯	⋯	⋯	⋯	⋯	⋯	4.0, 10.0
HGAL0.55−0.85	⋯	⋯	⋯	⋯	⋯	⋯	⋯	−10.0, −4.6
G09.62+0.19	⋯	⋯	⋯	⋯	10.0, 40.0	⋯	⋯	60.0, 75.0
G10.47+0.03	⋯	⋯	⋯	3.2, 20.0	20.0, 50.0	80.0, 180^a	−14.4, 2.4	⋯
G19.61−0.23	⋯	⋯	⋯	35.0, 93.0	105.8, 113.9	93.0, 127.0	−10.0, 20.0	28.0, 40.0
G29.96−0.02	⋯	1.6, 18.4	⋯	37.0, 85.0	⋯	⋯	⋯	⋯
W43 MM1	−5.0, 5.0	5.0, 21.4	⋯	21.4, 50.0	⋯	⋯	⋯	50.0, 100.0
G31.41+0.31	0.0, 20.0	⋯	⋯	30.0, 58.0	⋯	⋯	⋯	⋯
*G32.80+0.19	⋯	5.0, 6.0	⋯	15.0, 57.0	58.0, 120.0	⋯	⋯	⋯
G45.07+0.13	−2.0, 20.0	⋯	⋯	20.0, 60.0	⋯	⋯	⋯	60.0, 79.0
DR21	⋯	⋯	⋯	⋯	⋯	⋯	⋯	5.0, 20.0
NGC 7538 IRS1	−12.2, 4.4	⋯	⋯	⋯	⋯	⋯	⋯	⋯

Notes. In the last column, "envelope" refers to the diffuse and translucent molecular gas layers surrounding dense molecular gas regions associated with the background continuum sources. For the source (G32.80+0.19) marked by an asterisk, its velocity intervals of crossing spiral arms are based on Reid et al. 2019.
^{a} The velocities from 120 − 180 km s^{-1} belong to the 135 km s^{-1} arm situated beyond the GC.
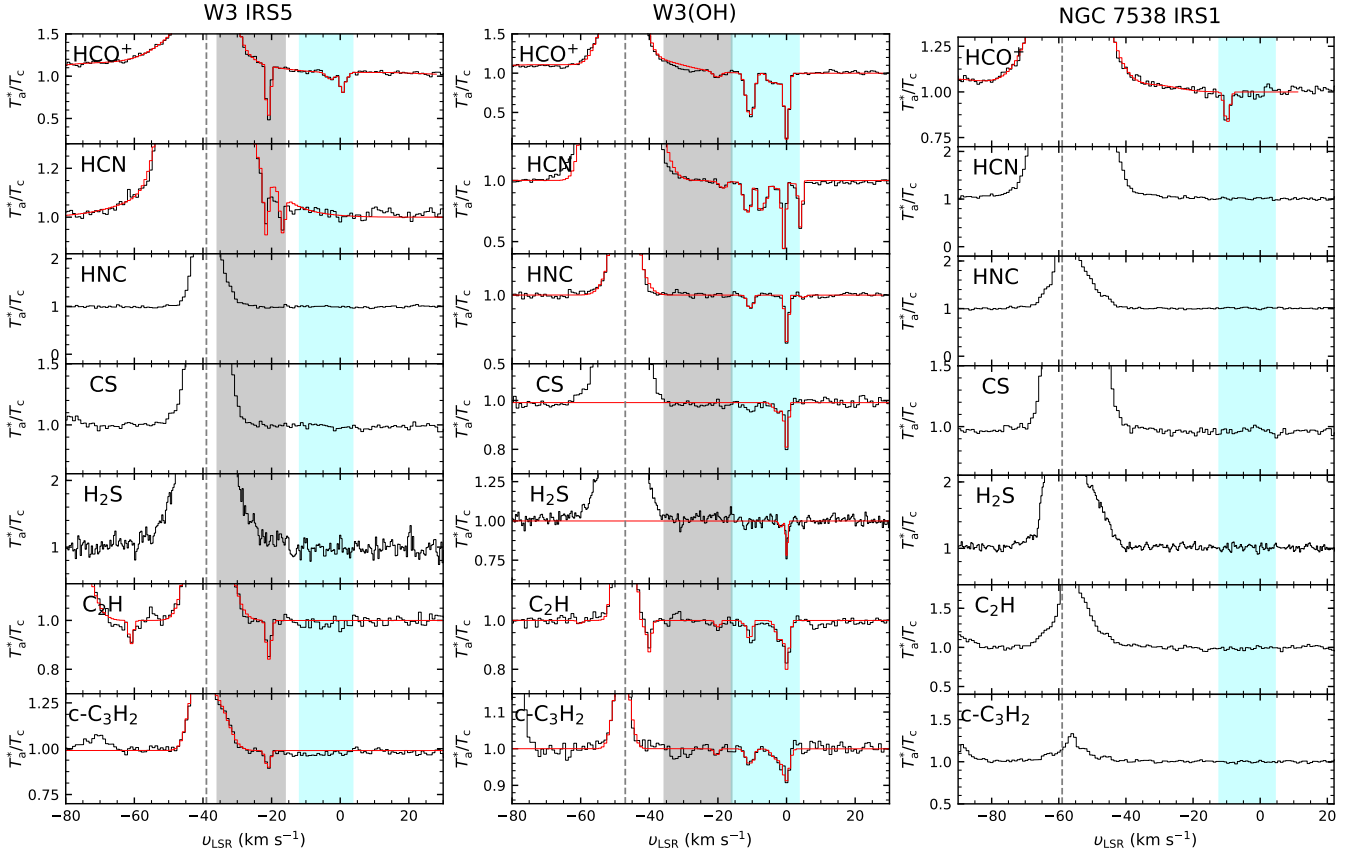
Fig. 3: Observed spectra (black) and the XCLASS modeled spectra (red) in a T_a^*/T_c scale, toward W3 IRS5, W3(OH), and NGC 7538 IRS1 from left to right. The spectra in each panel correspond to HCO$^+$, HCN, HNC, CS, H$_2$S, C$_2$H, and c-C$_3$H$_2$, from top to bottom. The shaded areas indicate velocity intervals of the local arm in cyan and the Perseus arm in gray. The v_{sys} of the continuum sources are indicated using vertical dashed lines.

3. Results

3.1. Detected absorption lines

Table 5 lists the molecular species detected in absorption observed toward 14 out of the 15 millimeter continuum sources. The spectra obtained toward the last target listed in Table 1,

G357.558−00.321, are not shown because the observations were not sensitive enough to detect the millimeter wave continuum from this weakest of the 15 sources. Some continuum sources have broad emission features of HCO$^+$, HCN, HNC, CS, and H$_2$S at their v_{sys}, spanning a few tens of km s^{-1}. Several absorption lines are detected at the LSR velocities of such emission line wings and/or emission lines at v_{sys}. It is not clear if the absorp-

tion lines arise from physically unrelated foreground clouds or if they are associated with the molecular gas of the star forming regions in which the continuum sources reside, in particular their dense envelopes. In some cases (see for e.g., Fig. 9 toward G19.61−0.23 and G32.80+0.19) the absorption line components have distinct offsets in velocity from the emission lines and these components unambiguously trace foreground diffuse or translucent clouds.

The continuum sources observed here are Hɪɪ regions and massive star-forming regions (see Paper I for the details of the HyGAL program). Some of them (e.g., G31.41+0.31) are chemically rich environments whose submillimeter and millimeter spectra exhibit a multitude of molecular emission lines associated with star-formation (e.g., outflows and hot molecular cores, Nony et al. 2018; Gorai et al. 2021). The CS, H_2S, and c-C_3H_2 spectra are severely contaminated molecular lines emitted by the background continuum source, various of them unidentified. As a result, the detection rates of absorption features for these transitions are lower than those of the other species. Moreover, the c-C_3H_2 transition we targeted lies close to the HCS^+ ($J = 2 \rightarrow 1$) transition at 85.3479 GHz (Margulès et al. 2003), with a velocity separation of only −31.6 km s^{-1}, and the H_2S transition is relatively close to the ^{34}SO ($J = 4_4 \rightarrow 3_3$) transition at 168.8151 GHz. At negative velocities with respect to the source systemic velocity, some c-C_3H_2 and H_2S absorption components – the presence of which is suggested by corresponding absorption lines of the other molecular species (mainly HCO^+) – are blended with the emission lines of HCS^+ and ^{34}SO. For these cases, we simultaneously fit the HCS^+ and ^{34}SO emission lines with the c-C_3H_2 and H_2S absorption lines, respectively. In total, we have detected HCO^+ absorption features in the spectra of all 14 sightlines listed in Table 5 and so velocities of HCO^+ absorption components were used as a reference for identifying absorption line features in the six other molecular line transitions studied. A significant number of sightlines also have detectable absorption lines of HCN (12 sightlines), HNC (11 sightlines), C_2H (12 sightlines), and c-C_3H_2 (nine sightlines) transitions. CS and H_2S are only detected toward eight and six sources, respectively, because of the poorer S/N at the higher H_2S transition frequency or significant emission line contamination.

Figures 3 - 9 present the observed spectra, normalized with respect to the continuum flux and displayed as a function of v_{LSR}. Fits to the spectra, obtained with the eXtended CASA Line Analysis Software Suite (XCLASS, Möller et al. 2017), are overlaid in red. The shaded areas designate the velocity intervals of specific spiral arms, inter-arm regions, and unidentified foreground clouds or the envelope layers of dense molecular cloud associated with the continuum sources; their velocity intervals, defined by previous observational studies (see Paper I and references therein), are tabulated in Table 6. In emission, HCN ($J = 1 \leftarrow 0$) has three hyperfine components ($F = 1 \leftarrow 1$, $F = 2 \leftarrow 1$, and $F = 0 \leftarrow 1$) that are completely blended, leading to even broader observed line widths. In absorption, however, the narrower intrinsic line widths in diffuse and translucent clouds often permit all three hyperfine structure (hfs) components to be individually discerned. We see blended HCN hfs profiles in absorption toward some sightlines because several superposed foreground clouds have similar velocity ranges. C_2H ($J = 1 \leftarrow 0$) is another molecular transition with multiple hyperfine components. This line has six hfs components, with the two weakest components being well separated and each of the two brightest components being blended to the remaining two components. We defined the frequency of the brightest component ($J = 3/2 \leftarrow 1/2$, $F = 2 \leftarrow 1$, 87.3168 GHz) of C_2H as the rest frequency for

purposes of computing the v_{LSR}. C_2H is found to be ubiquitous in the Milky Way, and thus it often traces multiple velocity components. HCO^+ ($\mu_A = 3.90$), HCN ($\mu_A = 2.984$) and HNC ($\mu_A = 3.04$) have much larger dipole moments than CO ($\mu_A = 0.110$) and can therefore be detected in absorption far more easily than CO in low-density clouds.

3.2. Detected absorption line profiles

3.2.1. W3 IRS5, W3(OH), and NGC 7538 IRS1

The second quadrant sources W3 IRS5, W3(OH), and NGC 7538 IRS1 are located in the Perseus arm in the outer Galaxy. W3 IRS5 and W3(OH) harbor high mass young stellar objects in different evolutionary stages that belong to the W3 molecular clouds and Hɪɪ region complex, while NGC 7538 IRS1 is the most prominent of several such sources in the NGC 7538 region. As in the host arm of the background sources, the Perseus arm, the sightlines toward these three sources are also aligned along the local arm where they cover a velocity range from ~ -16 km s^{-1} to 7 km s^{-1}. In the spectra toward W3 IRS5 shown in the left panel of Fig. 3, three components in HCO^+ absorption are detected at velocities of −20, −3, and 0.7 km s^{-1}, respectively, where the −20 km s^{-1} component is the deepest one. Only the −20 km s^{-1} component appears in HCN, C_2H, and c-C_3H_2. Toward W3(OH) (the middle panel of Fig. 3), we find three HCO^+ components at velocities (−20, −2 and 0 km s^{-1}) similar to those seen toward W3 IRS5 and also notice an additional component at −10 km s^{-1}, not detected in the sightline to W3 IRS5. The deepest feature along this sightline is at 0 km s^{-1}, with that at −10 km s^{-1} being the next deepest. These velocity components are also detected in the spectra of the six other species except for the −20 km s^{-1} feature, which is not observed in the HNC and H_2S spectra.

Toward NGC 7538 IRS1, we only detect a single HCO^+ component at −10 km s^{-1}, as shown in the right panel of Fig. 3. All the detected absorption components toward these three sightlines are associated with the local arm, except for the −20 km s^{-1} component toward W3 IRS5. This −20 km s^{-1} feature likely arises from diffuse clouds belonging to the Perseus arm rather than the envelope of the molecular cloud as C_2H and c-C_3H_2 absorption lines show a clear separation from the background emission. In addition, the spectra of CH, OH, OH^+, O, C^+, and ArH^+ from the SOFIA HyGAL observations in Paper I all show absorption line dips around this velocity. The hydride, O, and C^+ absorption lines show variations in absorption line profiles for W3(OH) and W3 IRS5, also seen here in the millimeter spectra.

3.2.2. NGC 6334 I and DR21

NGC 6334 I and DR21 are in the vicinity of the solar neighborhood with heliocentric distances of 1.3 and 1.5 kpc, respectively. However, these sources reside in different spiral arms, namely the Sagittarius arm and the local arm, respectively. Toward NGC 6334 I (upper panel of Fig. 4), we find two distinct HCO^+ absorption components at +7 km s^{-1} and +14 km s^{-1}, respectively, of which the first is the most prominent one, while the latter has a significantly broader profile ($\Delta v \sim 8$ km s^{-1}). HF (an excellent tracer of molecular gas, including CO-dark gas) absorption at 243 μm (van der Wiel et al. 2016), shows foreground clouds at +6 and +8 km s^{-1} that are not considered to be physically associated to the NGC 6334 molecular cloud. The HCO^+ absorption component at +7 km s^{-1} is believed to arise from the same clouds in which HF is detected. The richness of molecular emis-
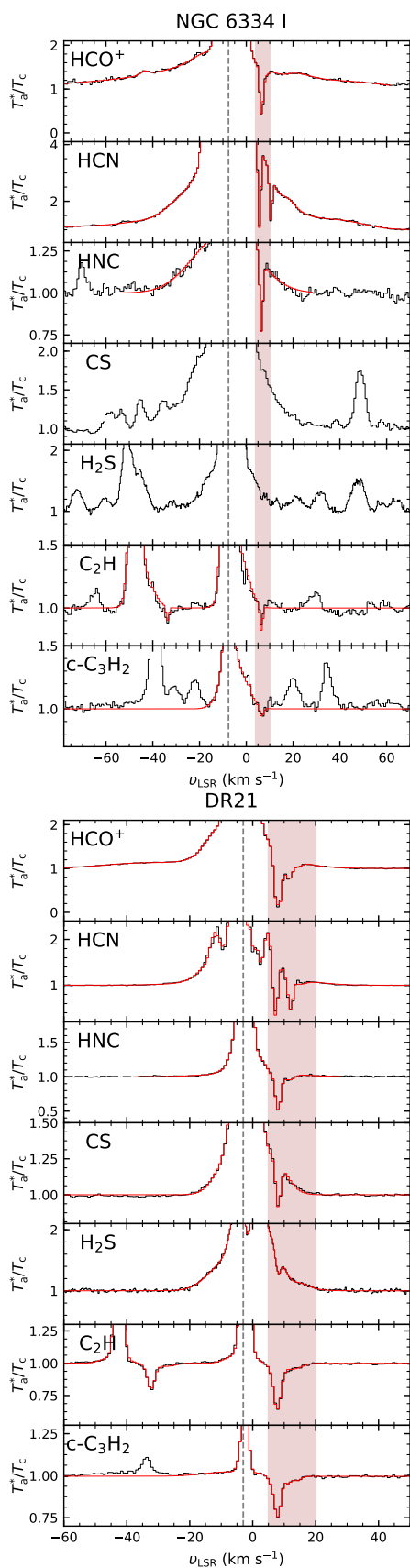
Fig. 4: Same as Fig. 3 but toward NGC 6334 I and DR21. The brown shaded areas indicate velocity intervals of the molecular cloud envelope layers or unidentified foreground clouds toward these sightlines.

sion lines prohibits a convincing absorption line detection in the CS and H_2S spectral windows while the other species show an absorption feature close to the $+7\,km\,s^{-1}$ velocity of HCO^+.

Toward DR21 (lower panel of Fig. 4), we detected absorption features for all seven species, of which the two small hydrocarbons (C_2H, c-C_3H_2) show a broader line shape than the other species without a red-shifted emission wing indicating an outflow as traced by HCN, CS, and H_2S. The deepest absorption lines seen at $+8.4\,km\,s^{-1}$ for all species originate from diffuse, extended gas surrounding the W75N cloud for which the majority of the emission is seen at $+9\,km\,s^{-1}$ (Schneider et al. 2010).

3.2.3. HGAL0.55−0.85 and G09.62+0.19

HGAL0.55−0.85 is located in the Galactic Center region and shows broad emission wings in lines from the HCO^+, HCN, and CS molecules. As seen in the upper panel of Fig. 5, only two narrow absorption components are found in the HCO^+ spectrum at −7 and −10 km s^{-1}, respectively, in the blue-shifted HCO^+ emission wing.

G09.62+0.19 lies in the Norma spiral arm near the expanding 3 kpc arm. In addition, the sightline crosses the Scutum-Centaurus and Sagittarius arms over a range of velocities from +10 to +40 km s^{-1}. Our mm band survey detected three distinct HCO^+ absorption features at +16, +23, and +69 km s^{-1} as shown in the lower panel of Fig. 5 toward G09.62+0.19. The first two features have a large velocity shift from the systemic velocity of the embedded Hɪɪ regions (−5–0 km s^{-1}), which is close to velocities of dense molecular cores (+2 to +5km s^{-1}, Liu et al. 2017, 2020) belonging to the Scutum-Centaurus arm. For all other transitions except for CS and c-C_3H_2 which we fail to fit because of the broad line emission from the background source, only a single absorption component is detected at +23 km s^{-1}. The weak absorption feature at +69 km s^{-1} only appears in HCO^+ and does not match any identified spiral arm.

3.2.4. G10.47+0.03

This background source lies in the inner Galaxy, behind the GC and the Galactic bar. Thus, several spiral arms pass through its sightline and they cause HCO^+ absorption features spanning a wide velocity range from −28 to +179 km s^{-1}, while background emission ranges between +52 and +83 km s^{-1}, as shown in Fig. 6. Such widespread absorption line features are also detected in the hydrides (ArH$^+$, o-H_2O^+, OH$^+$, and CH; Jacob et al. 2020), but the hydride absorption lines are broadly continuous, unlike what is seen in the HCO^+ absorption line profiles, which shows well separated components in distinct velocity intervals. The millimeter absorption lines in the velocity interval between −28 and +52 km s^{-1} originate from foreground clouds in inter-arm gas (−28 to +2.4 km s^{-1}), the near-side crossing of the Sagittarius arm (+3.2 to +20 km s^{-1}), and the Scutum-Centaurus arm (+20 to +52 km s^{-1}). Surprisingly, the inter-arm HCO^+ absorption feature shows a similar absorption depth, T_a^*/T_c, when compared to absorption lines arising in the spiral arms. However, the HCO^+ absorption lines belonging to the Scutum-Centaurus arm and the near-side of the Sagittarius arm display flat absorption dip profiles close to being saturated. Such broad features are also seen in the HCN spectra, while the spectra of the other species have mostly narrow absorption features. We notice that these HCO^+ absorption line features cover similar velocities as the OH$^+$ line at 1033 GHz line (Jacob et al. 2020) but have much narrower widths. The absorption around
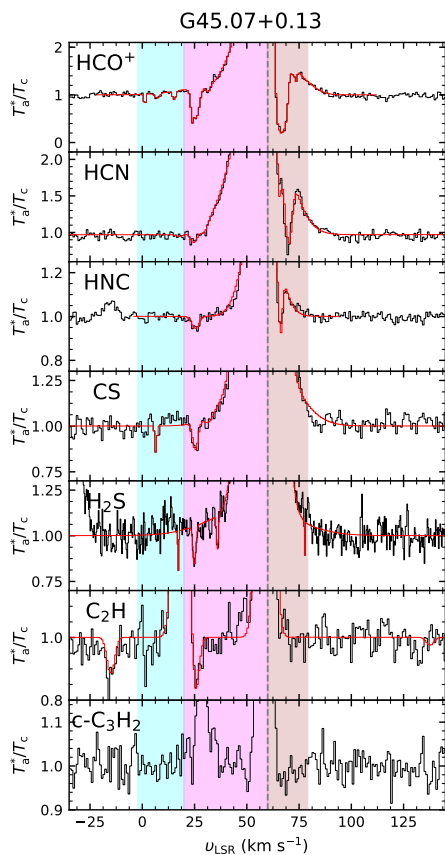
Fig. 6: Same as Fig. 3 but toward G10.47+0.03. The shaded areas indicate the velocity intervals of specific spiral arms (Sagittarius-Carina arm in magenta, Scutum-Centaurus arm in blue, inter-arm gas in orange, the GC/bar in yellow, and the 135 km s^{-1} arm located beyond the GC in blue-green).

Fig. 5: Same as Fig. 3 but toward HGAL0.55−0.85 and G09.62+0.19. The brown and blue shaded areas indicate velocity intervals corresponding to the molecular cloud envelope layers or unidentified foreground clouds, and the Scutum-Centaurus arm, respectively.

120 km s^{-1} is likely related to diffuse gas in the 3 kpc arm and the Galactic bar ($v > +80$ km s^{-1}), whereas the components at velocities greater than 120 km s^{-1} are believed to be associated with the +135 km s^{-1} spiral arm (Sormani & Magorrian 2015) located beyond the GC. Between these two velocity features, the HCO$^+$ 154 km s^{-1} feature is deeper than that belonging to the 3 kpc arm, while the deepest absorption component of OH$^+$ is at 120 km s^{-1} (Jacob et al. 2020). The 154 km s^{-1} component identified in HCO$^+$ is also detected in the spectra of HCN, HNC, C$_2$H, CS, and H$_2$S. However, the 120 km s^{-1} feature is barely seen in HCN, CS, and C$_2$H partly due to emission line contamination. As a well known hot core source, G10.47+0.03 is rich in complex molecules (Widicus Weaver et al. 2017). For the H$_2$S and c-C$_3$H$_2$ spectra, we detect multiple, strong emission components that further complicates the assignment and fitting of absorption line features.

3.2.5. G45.07+0.13

This background source lies in the Sagittarius arm and has an outflow, causing a broad blue-shifted wing (Hunter et al. 1997) in the emission profiles of lines from the HCO$^+$, HCN, and CS molecules. The absorption feature seen at 24 km s^{-1} in the millimeter transitions, displayed in Fig. 7 is believed to belong to its host spiral arm spanning a velocity interval between 20 and 60 km s^{-1}. The conspicuous absorption component at 67 km s^{-1} being red-shifted from the v_{sys} (60 km s^{-1}) in HCO$^+$, HCN, and

Fig. 7: Same as Fig. 3 but toward G45.07+0.13. The shaded areas indicate the velocity intervals of specific spiral arms (local arm in cyan and Sagittarius-Carina arm in magenta), and the molecular cloud envelope or unidentified foreground clouds in brown.

HNC likely traces infalling foreground gas toward the continuum source as it is similar to that of the CS ($2\leftarrow1$) absorption feature (Hunter et al. 1997) near $65-67.3\,\mathrm{km\,s^{-1}}$ obtained from interferometric observations revealing infalling gas motion. In addition, we also detect weak absorption lines related to the local arm (0 to $20\,\mathrm{km\,s^{-1}}$) at 1, 8, and $15\,\mathrm{km\,s^{-1}}$ in the HCO$^+$ spectrum.

3.2.6. G29.96−0.02, W43 MM1, and G31.41+0.31

The sightlines toward these three background sources, located in the Scutum-Centaurus arm, are in a similar direction. Along the sightline toward G29.96−0.02 (left panel of Fig. 8), we detected broad, deep absorption features from -0.6 to $+23\,\mathrm{km\,s^{-1}}$ in the HCO$^+$ spectrum, related to the Aquila Rift (Paper I), while multiple absorption components in the range from $+49$ to $+79\,\mathrm{km\,s^{-1}}$ correspond to the near-side crossings of the Sagittarius spiral arm. All of these components are found in other millimeter transitions, except those originating in the Sagittarius arm, which are not detected in the H$_2$S, and c-C$_3$H$_2$ spectra at rms levels, 12.5 and 7.5 mK, respectively. The HCO$^+$ absorption line at $8\,\mathrm{km\,s^{-1}}$ has a significantly broader profile, while the absorption profiles of HNC, CS, and the two small hydrocarbons show multiple dips within the velocity interval of the Aquila-Rift region. Such multiple dips are also found in H I absorption spectrum (Fish et al. 2003) between -0.6 and $+23\,\mathrm{km\,s^{-1}}$, showing at least four well separate absorption components. All detected absorption features in these millimeter transitions have coun-

terparts of absorption components in the spectrum of o-H$_2$Cl$^+$ (Neufeld et al. 2015).

W43 MM1 and G31.41+0.31 are situated in the Scutum-Centaurus spiral arm and classified as hot cores (Nony et al. 2018; Widicus Weaver et al. 2017) which give rise to a variety of emission line features at millimeter wavelengths. Due to forests of emission lines blending into the absorption features, we only fit certain absorption features, causing that the model fits to some of the absorption features have greater uncertainties others. HCO$^+$ absorption features toward W43 MM1 (the middle panel of Fig. 8) appear intermittently from $+1$ to $+85\,\mathrm{km\,s^{-1}}$ and among them, the absorption components with a dip at $11\,\mathrm{km\,s^{-1}}$ traces diffuse gas from the Aquila Rift. Some of the HCO$^+$ absorption features within this velocity range partly correspond to the near-side crossing of the Sagittarius arm (roughly $+24$ to $+50\,\mathrm{km\,s^{-1}}$) and are possibly related to local diffuse gas from its host spiral arm, the Scutum-Centaurus arm ($+50$ to $+100\,\mathrm{km\,s^{-1}}$) with $v_{\mathrm{sys}} = +98\,\mathrm{km\,s^{-1}}$. It is, however, not clear whether all the absorption features arise in the Scutum-Centaurus arm or partly related to inter-arm gas or to some other region.

Several absorption lines in the observed transitions are detected along the sightline toward G31.41+0.31 (right panel of Fig. 8), but we have only fit components associated with the local arm (0 to $20\,\mathrm{km\,s^{-1}}$) because its velocity range is less affected by emission contamination. In the HCO$^+$ spectra, both absorption components at 7 and $13\,\mathrm{kms}$ have a similar depth, but for other molecular species, the features at $7\,\mathrm{km\,s^{-1}}$ are much weaker than those at $13\,\mathrm{km\,s^{-1}}$.

3.2.7. G19.61−0.23 and G32.80+0.19

These two sources are inferred to lie in the first quadrant of the Milky Way in the Perseus and Sagittarius-Carina spiral arms at distances of 12.6 kpc and 9.7 kpc respectively. Such large distances allow several spiral arms to be intercepted by the sightlines, resulting in multiple absorption components in the molecular spectra observed toward these sources. Along the sightline toward G19.61−0.23 (upper panel of Fig. 9), the HCO$^+$ spectrum shows absorption features spanning a wide velocity range from $-7\,\mathrm{km\,s^{-1}}$ to $130\,\mathrm{km\,s^{-1}}$. Several features absorb parts of the emission line arising from the molecular gas related to the background continuum source, which drives an outflows that produces broad red- and blue-shifted emission wings for optically thick transitions (Furuya et al. 2011). The HCO$^+$ absorption dip at $46\,\mathrm{km\,s^{-1}}$ appears at the velocity of an absorption component of C^{18}O ($3\leftarrow2$) (Furuya et al. 2011), observed with the Submillimeter Array (SMA), implying infalling gas in the low-density outer layers of the central core, which may be interpreted as self-absorption in the background source. On the other hand, another prominent feature at $51\,\mathrm{km\,s^{-1}}$ in the absorption spectrum of HCO$^+$ is absent in the ^{13}CO ($3\leftarrow2$) absorption spectrum, unlike that at $46\,\mathrm{km\,s^{-1}}$. Prominent absorption components at $51\,\mathrm{km\,s^{-1}}$ and also at higher velocities, 71, 100, and $119\,\mathrm{km\,s^{-1}}$, have corresponding H I absorption features (Kolpak et al. 2003). Absorption features at these four velocities appear in millimeter transitions and, therefore, seem to be arising in intervening clouds along the sightline. The first two features at 51 and $71\,\mathrm{km\,s^{-1}}$ are associated with the near- and far-side crossings of the Sagittarius spiral arm (spanning from ~ 35 to $74\,\mathrm{km\,s^{-1}}$), and the latter, at 100 and $119\,\mathrm{km\,s^{-1}}$, are believed to be located on the 3 kpc arm. We also find red-shifted absorption features with respect to the v_{sys} of $41.8\,\mathrm{km\,s^{-1}}$ for this source and assume that these absorption lines are unrelated-foreground clouds as H I absorption line components are also detected in this velocity range
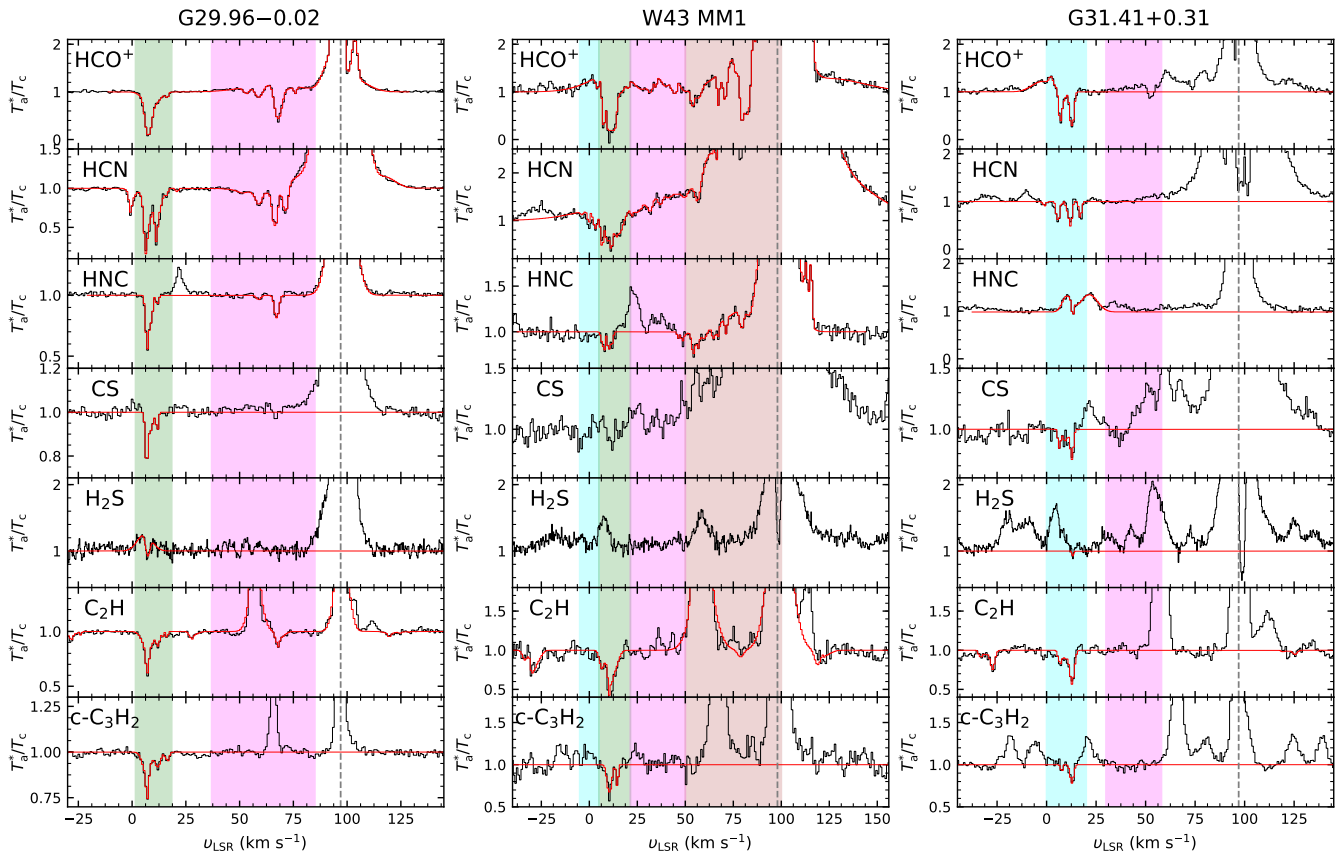
Fig. 8: Same as Fig. 3 but toward G29.96−0.02, W43 MM1, and G31.41+0.31. The shaded areas indicate the velocity intervals of specific spiral arms (local arm in cyan, Sagittarius-Carina arm in magenta, Aquila-Rift in green), and the molecular cloud envelope or unidentified foreground clouds in brown.

(Kolpak et al. 2003). The HCN, HNC, C_2H, and c-C_3H_2 lines show similar absorption features as the HCO^+ spectrum. In the CS and H_2S spectra fewer absorption features are identified, for H_2S spectrum this is caused by its ragged baseline, possibly the result of a number of emission lines.

Toward G32.80+0.19 (lower panel of Fig. 9), for all seven species, we detect widespread absorption features spanning a broad range of velocities from 2 to 110 km s^{-1} with the v_{sys} of 15 km s^{-1} and emission spanning 1− 28 km s^{-1} from the background source. Apart from the red-shifted components with respect to v_{sys}, the blue-shifted absorption features in the HCO^+, HCN, C_2H, and c-C_3H_2 spectra are detected in the velocity interval between 4 and 15 km s^{-1} which is close to the velocity range of the Aquila-Rift. These absorption lines are possibly associated with foreground cloud components. As seen in the HCO^+ spectra toward the other background continuum sources, the HCO^+ spectrum toward G32.80+0.19 clearly shows absorption features that are broader than those of the other six species. Absorption features in the velocity interval between 58 and 120 km s^{-1} trace the Scutum-Centaurus spiral arm and show four prominent dips at 70, 81, 85, and 89 km s^{-1}. The deepest dip for HCO^+, HCN, HNC, and the two small hydrocarbons are at 89 km s^{-1}. On the other hand, CS and H_2S show the deepest dips at 85 km s^{-1}. Absorption in the $N_{k_a,k_c} = 1_{1,0} \leftarrow 1_{1,1}$ line of H_2CO at a frequency of 4.83 GHz (wavelength 6.2 cm)) is observed by (Araya et al. 2002) against the radio continuum emission of the same background source at similar velocities as the CS and H_2S line with its deepest absorption appearing at $\sim$ 85 km s^{-1}. The Sagittarius arm and the Aquila Rift also cross this sightline and correspond

to velocity ranges of 15−57 km s^{-1} and 5−6 km s^{-1}, respectively. The red-shifted absorption features with respect to the source's systemic velocity at 15 km s^{-1} could arise from low-density diffuse gas associated with the molecular clouds of the continuum source as the H_2CO absorption features (Araya et al. 2002) correspond to the features seen in the HCO^+, C_2H, and c-C_3H_2 spectra. However, as its velocities correspond to Aquila Rift as well.

3.3. CO emission counterparts

As described in the previous section, the millimeter absorption components of simple molecules detected in this survey generally have narrower line features than those those of the hydride molecular ions (e.g., OH^+ or ArH^+, Schilke et al. 2014; Jacob et al. 2020), whose submillimeter absorption spectra have continuous broad line profiles over wide velocity ranges. Such narrow spectral line shapes might imply that the millimeter absorption lines of neutral species and HCO^+ trace denser gas than that traced by hydride molecular ions. To investigate whether any of the CO emission from dense molecular clouds is detected at the velocities of HCO^+ absorption, we utilized archival data from available CO emission surveys: for ^{13}CO (2→1) data mapped with an angular resolution of 30′′, the Structure, Excitation and Dynamics of the Inner Galactic Interstellar Medium (SEDIGSM, Schuller et al. 2021) program obtained with the SHeFI single-pixel instrument at the 12 m diameter Atacama Pathfinder Experiment submillimeter telescope; for ^{13}CO (1→0) data obtained with an angular resolution of 46′′ in the inner Galaxy, the Boston
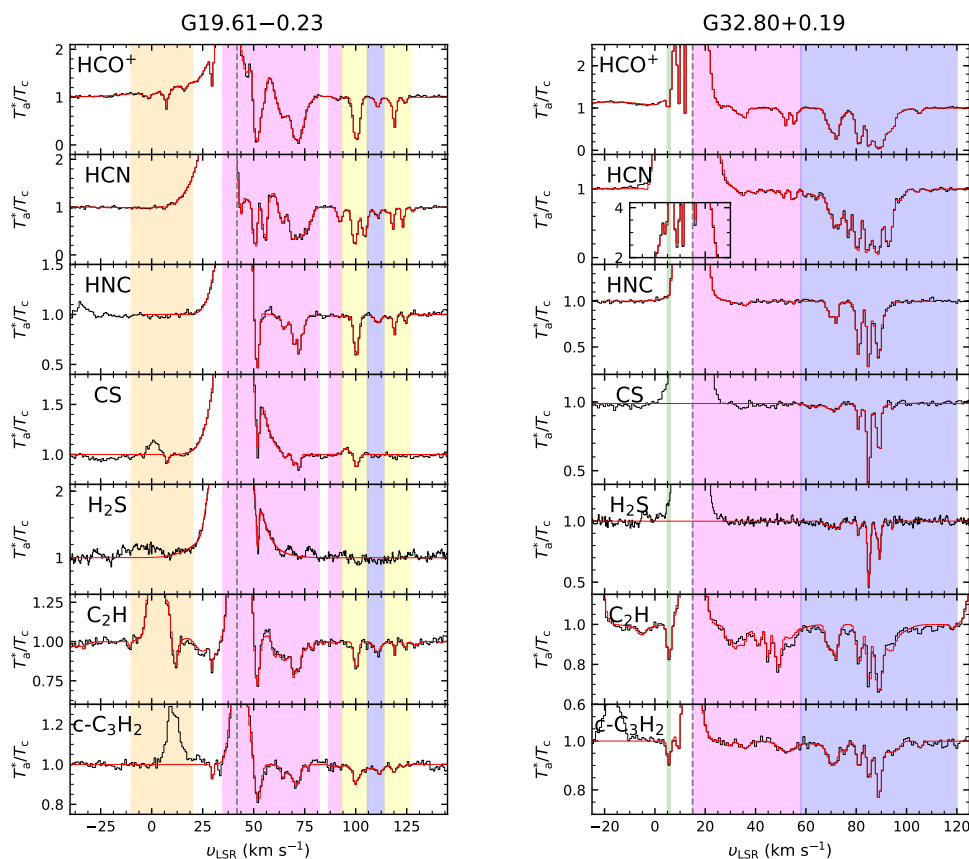
Fig. 9: Same as Fig. 3 but toward G19.61−0.12 and G32.80+0.19. The shaded areas indicate velocity intervals of specific spiral arms (Aquila-Rift in green, Sagittarius-Carina arm in magenta, Scutum-Centaurus arm in blue, inter-arm gas in orange, the GC/bar in yellow), and the molecular cloud envelope or unidentified foreground clouds in brown. Toward G32.80+0.19, the insert in the HCN panel zooms in on the HCN absorption features on top of the emission within a velocity window between $-10\,\mathrm{km\,s^{-1}}$ and $30\,\mathrm{km\,s^{-1}}$.

University-FCRAO Galactic Ring Survey (GRS, Jackson et al. 2006) that used the SEcond QUabbin Optical Imaging Array (SEQUOIA) at the Five College Radio Astronomy Observatory 14 m telescope; and for ^{12}CO (1→0) and ^{13}CO (1→0) observed with an angular resolution of 20″ the FOREST Unbiased Galactic plane Imaging survey performed with the Nobeyama 45 m telescope (FUGIN, Umemoto et al. 2017) and the telescope's four-beam, dual-polarization, sideband-separating SIS receiver. Figure 10 displays the CO emission spectra toward eight of our sources obtained from the surveys mentioned above; they are G09.62+0.19, G10.47+0.03, G19.61−0.23, G29.96−0.02, W43 MM1, G31.41+0.31, G32.80+0.19, and G45.07+0.13. The upper panels show the ^{12}CO (1→0) emission (in black) and ^{13}CO (1→0) or (2→1) (in red) on the main-beam temperature (T_{mb}) scale, and the lower panels show HCO$^+$ absorption spectra (in blue) normalized relative to the continuum. The vertical dotted lines indicate representative absorption dips. For G09.62+0.19, only the ^{13}CO (2→1) data from the SEDIGIM survey is available, and G10.47+0.03 is observed only in the FUGIN survey, but not the GRS survey. Since the rms noise level of the FUGIN ^{13}CO (1→0) data is higher than that of the GRS survey, we mainly use the ^{13}CO (1→0) data of the GRS survey for the remaining sightlines observed in our survey. After extracting the CO spectrum within an area covered by a 20″ radius, we resampled the spectral data to 0.6 km s^{-1} velocity bins that are 2.4 − 6 times broader than the original spectral resolutions of the SEDIGIM and GRS surveys. For the FUGIN data, we smoothed

the spectral channel resolution to 1.3 km s^{-1} to improve S/N levels.

In Fig. 10, the most prominent absorption features have CO emission counterparts while weak absorption lines tend be not to have a detection of CO emission except for the absorption features around $0 - 20$ km s^{-1} toward G45.07+0.13. In addition, not all deep absorption features have clear CO emission lines at their velocity ranges. For some velocity components toward some sources, CO emission features have different intensities, although the HCO$^+$ absorption line depths are comparable. For example, toward G10.47+0.03, the depth of the absorption feature at around 154 km s^{-1} is similar to that of the absorption components spanning $0 - 50$ km s^{-1}, but its CO emission counterpart is weaker. Frequently, compared to HCO$^+$ with narrow line profiles, broad HCO$^+$ absorption features tend to have CO emission counterparts.

4. Analysis

4.1. Line parameter determination with XCLASS

The spectral lines observed were modeled using the eXtended CASA Line Analysis Software Suite (XCLASS[3], Möller et al. 2017) by solving the 1-dimensional radiative transfer equation with the assumption of local thermal equilibrium (LTE) for an

---

[3] https://xclass.astro.uni-koeln.de
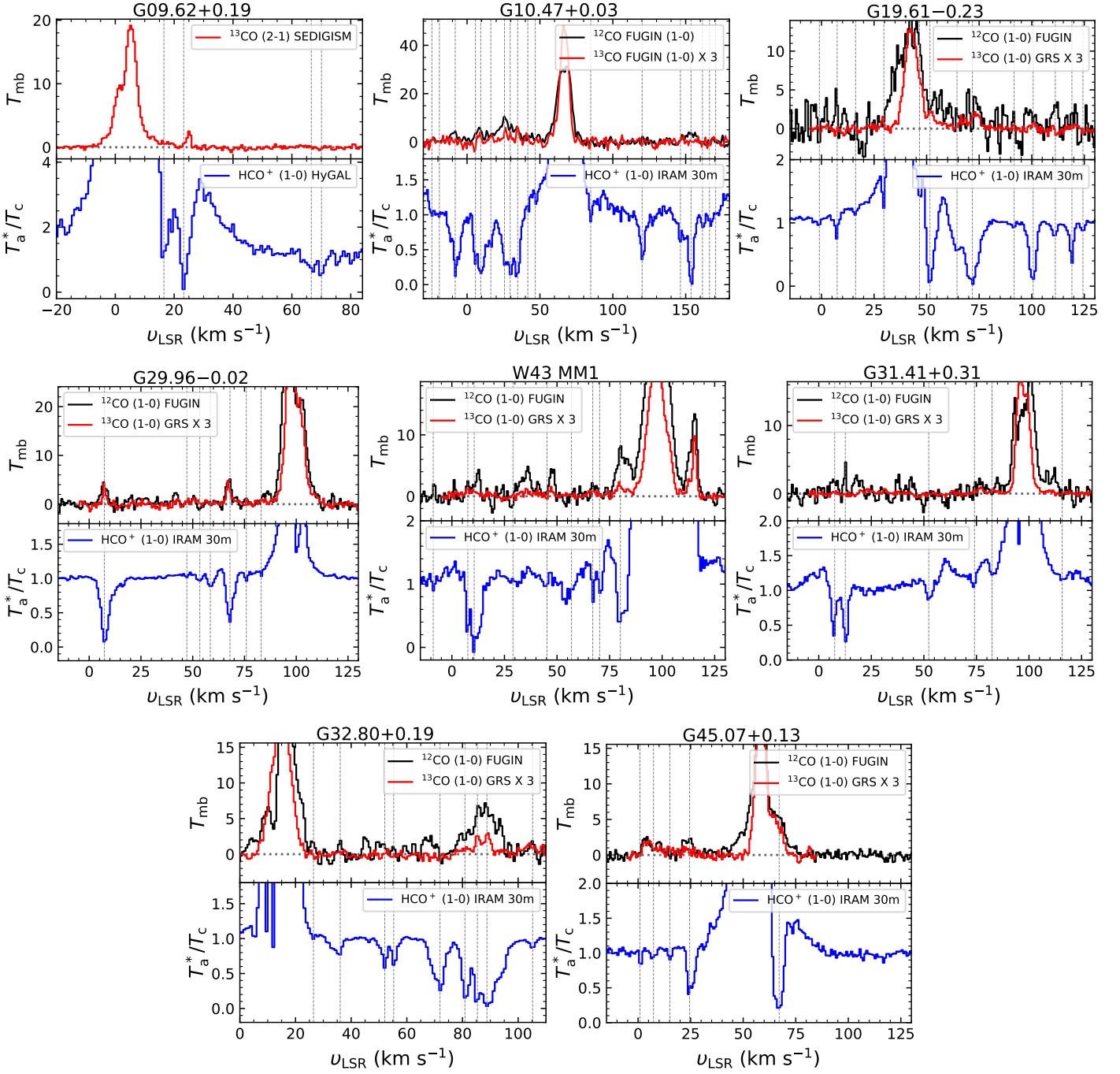
Fig. 10: Spectra lines of CO and HCO$^+$ toward the eight sightlines. The upper panel for each plot shows ^{12}CO emission lines $(1 \rightarrow 0)$ in black, obtained from the FUGIN survey (Umemoto et al. 2017), and ^{13}CO $(1 \rightarrow 0)$ emission lines in red from the GRS survey (Jackson et al. 2006). For only G09.62+0.19, the ^{12}CO $(2 \rightarrow 1)$ is taken from the SEDIGISM survey (Schuller et al. 2021). The lower panel for each plot shows absorption and emission lines in HCO$^+$ spectra in blue from this survey. In the both panels, the vertical dotted lines indicate significant absorption features.

isothermal source. The `myXCLASSFit` program computes synthetic spectra, by fitting the spectral lines with Gaussian profiles, thereby ensuring that opacity effects on the line shapes are properly taken into account. The fit is performed using optimization package `MAGIX` (Möller et al. 2013), which provides an interface between the input codes and an iterating engine. It minimizes the deviation between the modeled outputs from the observational data. Molecular properties (e.g., Einstein A coefficients, partition functions, etc.) are taken from an embedded SQLite database containing entries from the Cologne Database for Molecular

Spectroscopy (CDMS, Müller et al. 2001, 2005) and the Jet Propulsion Laboratory database (JPL, Pickett et al. 1998) in its Virtual Atomic and Molecular Data Center (VAMDC, Endres et al. 2016) implementation, along with an extended set of partition function calculations. The parameter set fitted for each absorption line component consists of the excitation temperature (T_{ex}), the total column density (N_{tot}), the line width (Δv), and the velocity offset (v_{off}) from the systemic velocity. The column density per velocity interval, dN/dv for each velocity channel, i,
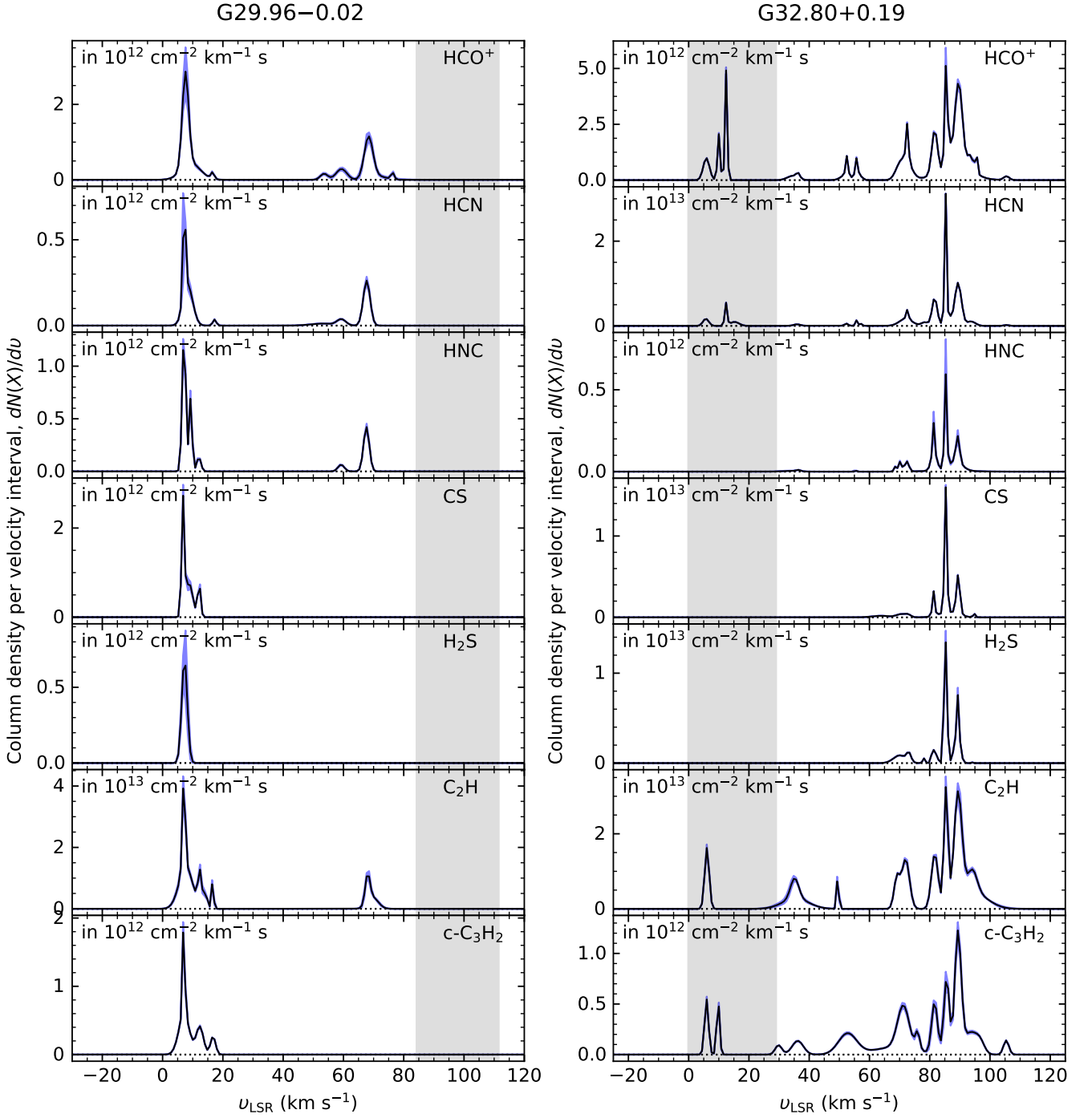
Fig. 11: Channel-wise column density spectra (dN/dv) as a function of velocity toward G29.96−0.02 and G32.80+0.19. The dN/dv in each panel shows HCO⁺, HCN, HNC, CS, H₂S, C₂H, and c-C₃H₂ from top to bottom. The gray shaded area indicates velocity range of the HCO⁺ emission lines. The blue shaded regions represent 2σ confidence intervals for the derived column densities (per velocity interval).

is related to the optical depth, τ_i, (Paper I) by

$$\left(\frac{dN}{dv}\right)_i = \frac{8\pi\nu^3}{c^3}\frac{Q(T_{\text{ex}})}{g_u A_{ul}}\frac{\exp(E_u/kT_{\text{ex}})}{\exp(h\nu/kT_{\text{ex}})-1}\tau_i, \quad (1)$$

where E_u is the energy of the upper state for the selected transition, g_u is the upper state degeneracy, and ν is the frequency of a molecular transition. The quantity A_{ul} is the Einstein coefficient for spontaneous emission, and $Q(T_{\text{ex}})$ and k are the partition function and Boltzmann constant, respectively. For the absorption components, we adopt a fixed excitation temperature

for all observed molecular transitions equivalent to the cosmic microwave background temperature of 2.73 K. This is motivated by the high dipole moments of most of the species, which lead to critical densities for the observed transitions that lie a few orders of magnitude above the typical number density of hydrogen molecules (n_{H_2}) in translucent clouds of a few hundred cm⁻³ (e.g., Snow & McCall 2006; Gerin et al. 2016). Thus, the excitation temperature of these transitions are determined by the 2.73 K cosmic background radiation field. XCLASS offers various algorithms to find the best-fit parameters by minimizing the
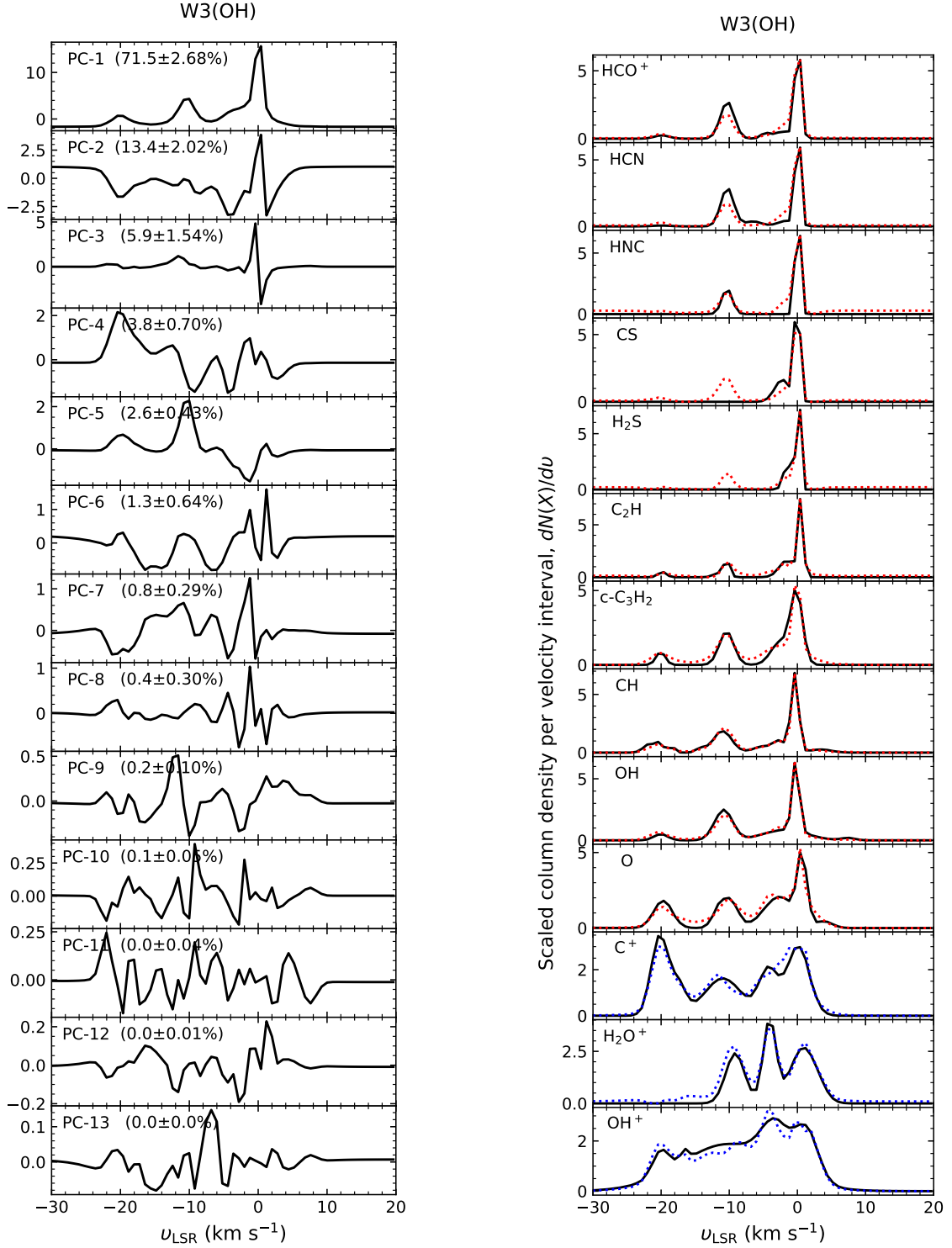
Fig. 12: *Left*: Eigen spectra of thirteen principal components with percentage of variances as well as uncertainties (2σ), toward W3(OH). *Right*: Scaled channel-wise column density spectra for the thirteen species (HCO^+, HCN, HNC, CS, H_2S, C_2H, c-C_3H_2, CH, OH, O, C^+, H_2O^+, and OH^+) as a function of v_{LSR}. Black curves represent the observational data, and red dotted curves are the spectra reproduced with only the first three principal components (PC-1, PC-2, and PC-3). For C^+, H_2O^+, and OH^+, the reproduced spectra indicated by blue dotted curves include one or two more PCs, i.e., PC-4 and PC-5.

χ^2 value, and in this work, we used the Levenberg-Marquardt algorithm. In addition, in the fitting procedure, all the hfs splitting transitions of HCN and C_2H are taken into account, and the fitting deconvolves the hfs of these molecular transitions. We note that we only consider the ortho transitions of H_2S and c-C_3H_2, and thus the derived column densities of these molecules only

apply to their ortho species, not to the sum of their ortho and para species. The spectral line profiles observed are the combination of emission and absorption features. We have performed simultaneous fitting of the emission and absorption lines to determine the background for the absorption lines and derive accurate physical properties for the absorption components. How-

ever, since the focus of this paper is the absorption system (rather than deriving reliable physical parameters of the emission lines), we do not present the fit parameters of the emission lines. For uncertainties of column densities derived here, we perform the error estimation by sampling a posterior distribution of the optical depths ($\propto \ln(T_a^*/T_c)$). The sampling was performed using XCLASS fits to multiple realizations of sample spectra that were generated by adding independent pseudorandom noise to the observed spectra. For the XCLASS fits, as done to the main fitting for the original data sets, we also fit emission and absorption components simultaneously on the noise-added spectra in order to take into account variability of the posterior distributions caused by emission components.

Figures 11 and A.1–A.5 display the column density per velocity interval, $dN(X)/dv$, determined for all seven species studied and toward all sources, with uncertainties indicated as blue shaded areas. The gray parts indicate the velocity ranges of the emission lines that partly overlap with the absorption lines. As a result, the column densities of the absorption components within the gray velocity ranges might have higher uncertainties than those implied by the blue shaded areas because of additional errors that may arise when emission components are simultaneously fitted with the absorption components.

4.2. Principal component analysis

Principal component analysis (PCA) has been used to investigate differences and similarities in the distributions of multiple species detected in absorption spectra (e.g., Sect. 4.2 in Neufeld et al. 2015). Here, we carried out PCA of our W3(OH) data for 13 species (HCO$^+$, HCN, HNC, CS, H$_2$S, C$_2$H, c-C$_3$H$_2$, CH, OH, O, C$^+$, H$_2$O$^+$, and OH$^+$) and for W3 IRS5 for 11 species (same as for W3(OH) except with the addition of ArH$^+$ and the omission of HNC, CS, and H$_2$S). The lattermost six species listed for W3(OH) were observed with SOFIA (Paper I). The SOFIA results published to date provide spectra of these species toward three sightlines, W3(OH), W3 IRS5, and NGC 7538 IRS1. Since only HCO$^+$ was detected toward NGC 7538 IRS1 in the present work, this sightline was not considered in our PCA analysis. Moreover, the SH absorption features detected with SOFIA toward these sightlines are all associated with the background continuum source; toward them foreground absorption is detected. Therefore, SH is not included in this PCA analysis. Instead of using transmission (T_a^*/T_c) or optical depth spectra, we used column densities, dN/dv, as the input to the PCA, thereby minimizing contributions from the emission features and avoiding complications caused by hfs. All the column density spectra were computed with a common channel width of 0.8 km s^{-1}. As discussed further below, we also accounted for uncertainties in the derived column densities, which can significantly affect the results of the PCA.

Prior to performing the PCA analysis, standardization is imperative: this involves rescaling the spectra so that their variations have a mean of zero and a variance of unity. PCA involves writing the column density for each species, i, as a linear combination of orthogonal eigenfunctions (a.k.a. principal components), $f_j(v)$

$$N_i(v) = a_i + b_i \sum_{j=1}^{k} C_{ij} f_j(v), \qquad (2)$$

where a_i and b_i and C_{ij} are coefficients, and k is the number of species included (13 for W3(OH) or 11 for W3 IRS5). The

C_{ij} obey a normalization constraint, $\sum_{j=1}^{k} C_{ij}^2 = 1$. To examine the reliability of the PCA results, uncertainty estimates are essential. Therefore, we made use of 1000 realizations obtained by random sampling within the column density probability distribution function and then for each realization of the 1000 realizations, we created a data set containing PCA results for all used species from the each PCA performance toward W3(OH) and W3 IRS5, respectively. From these multiple realizations, we obtained a distribution of the PCA results for each species. Using the posterior distributions for all considered species from the PCA performances for the 1000 realization, we obtained 2σ confidence intervals for all the PCA results; these are included in the results presented in the following section.

In Figures 12 and C.1, the left panels show eigen spectra of principle components with percentage of variances and uncertainties (2σ), toward W3(OH) and W3 IRS5, respectively. As the first component ($f_1(v)$, labeled PC-1) accounts for more than half of the variance for each source, its profile resembles the column density distributions of most of the species included in the PCA. However, there are significant differences between the W3(OH) (Fig.12) and W3 IRS5 (Fig. C.1) sightlines in regard to the fraction of the variance accounted for by each component. For W3(OH), PC-1 and PC-2 account respectively for 71.5±2.6 % and 13.4±2.0 % of the total variance, Toward W3 IRS5, PC-2 accounts for a more significant fraction of the total variance, 22.6±2.0 %, and PC-1 accounts for only slightly more than half (56.9±2.2 %) of the total. The right panel of Figs. 12 and C.1 represent scaled channel-wise column density spectra as black curves for the observed species (for W3(OH), HCO$^+$, HCN, HNC, CS, H$_2$S, C$_2$H, c-C$_3$H$_2$, CH, OH, O, C$^+$, H$_2$O$^+$, and OH$^+$; for W3 IRS5, HCO$^+$, HCN, C$_2$H, c-C$_3$H$_2$, CH, OH, O, C$^+$, H$_2$O$^+$, OH$^+$, and ArH$^+$). The column density spectra reproduced (red and blue dotted lines) by summing the first three terms in the expansion, for most of the species but for C$^+$, H$_2$O$^+$, OH$^+$, and ArH$^+$ by summing up to the first five terms : $C_{i1} f_1(v)$, $C_{i2} f_2(v)$ and $C_{i3} f_3(v)$, and additionally $C_{i4} f_4(v)$ and $C_{i5} f_5(v)$ for the mentioned species above. For both sources, the first three principal components account for $\sim$ 90% of the total variance, and the sum of their contributions provides a reasonable approximation to the column densities of the observed species.

5. Discussion

### 5.1. Correlations between species for W3(OH) and W3 IRS5

Figures 13 and 14 show the coefficients C_{ij} in the PCA expansion for each observed species. These are sometimes referred to as h-plots (e.g., Ungerechts et al. 1997). Figure 13 shows the coefficients, C_{i1} and C_{i2}, for the first and second components, PC-1 and PC-2, obtained for W3(OH) (left panel) and W3 IRS5 (right panel), while Fig. 14 shows the coefficients for the second and third terms in the expansion. Each colored vector corresponds to a different species as indicated, and the normalization condition for the C_{ij} coefficients implies that all the plotted vectors must lie within the unit circle (black). Colored ellipses indicate the uncertainties (corresponding to 2σ confidence intervals) for each vector.

The angle (θ) between any two vectors (corresponding to two different species) indicates how well the two species of a given pair are correlated with each other. The similarity between any two vectors may be characterized by the cosine of the angle between the vectors (known as cosine similarity); $\cos\theta = \mathbf{A} \cdot \mathbf{B}/\|\mathbf{A}\| \|\mathbf{B}\|$. Figures 15 and 16 present similarity coefficients estimated for each pair of species, with $\cos\theta$ represented
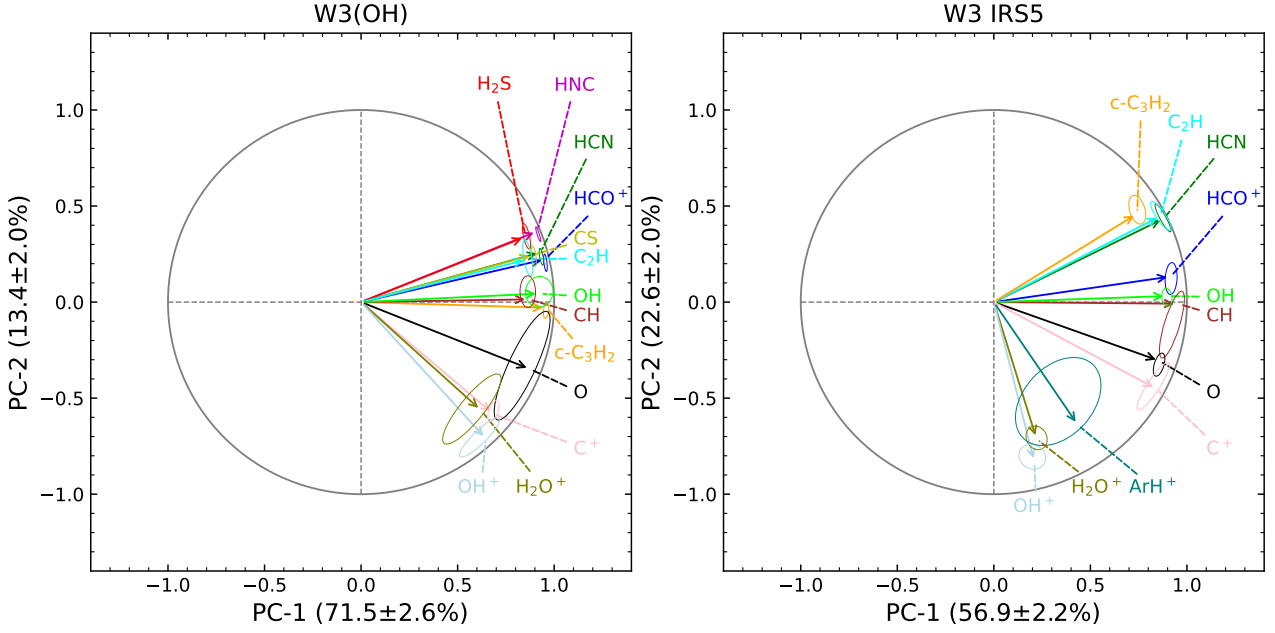
Fig. 13: Variable correlation circle plots for the first and second PCs toward W3(OH) in the left panel and W3 IRS5 in the right panel. The solid straight lines close to the unit circle imply PC-1 and PC-2 contain the most information about the variables. Different colors are used to denote the different species analyzed. Each colored ellipse is a 2σ confidence interval for the uncertainty of the PCA results for the corresponding species.
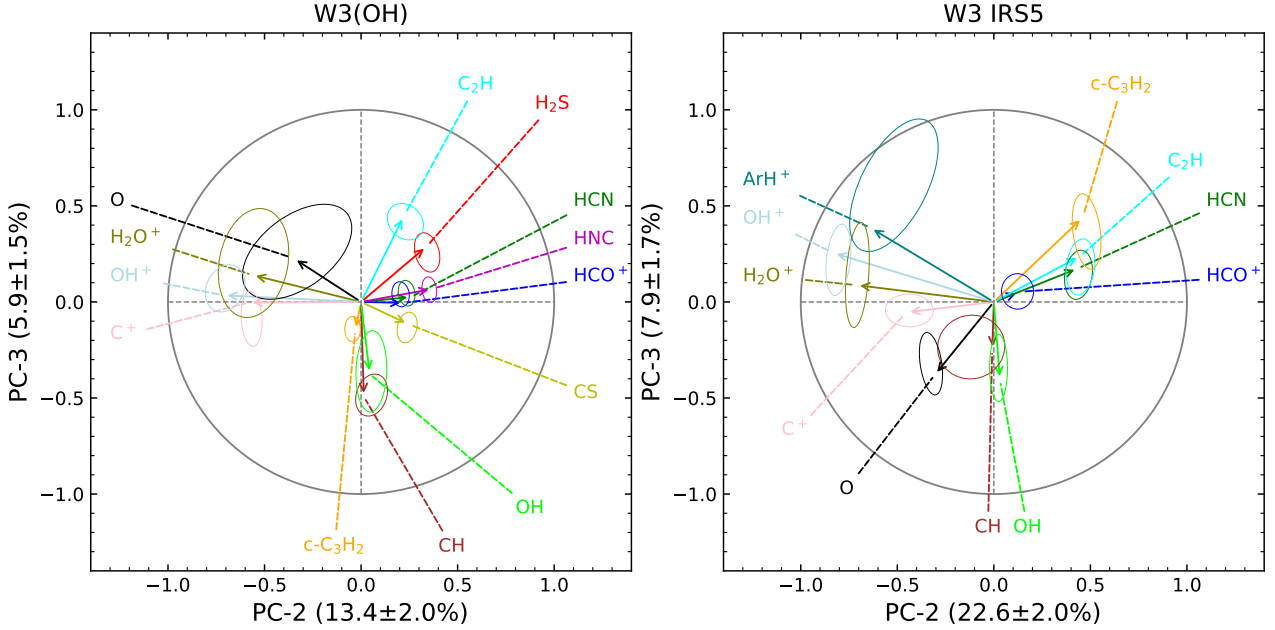

Fig. 14: Same as Fig. 13 but for the second and third PCs (PC-2 and PC-3) toward the same sources, from left to right.

as percentages; acute angles in the h-plots indicate a strong similarity ($\sim 100\,\%$ as noted in Figs. 15 and 16), orthogonal ($90°$) angles mean no similarity ($0\,\%$, i.e., lack of correlation), and opposite vectors with an angle of $180°$ represent negative similarity ($\sim -100\,\%$, i.e., anticorrelation). Although the sets of species detected are not exactly identical toward these sightlines, the relative positions of the vectors appear to be similar for most of the species, as shown in Fig. 13. In addition, we note that when we recompute the vector positions for the same set of species (HCO$^+$, HCN, C$_2$H, c-C$_3$H$_2$, CH, OH, O, C$^+$, H$_2$O$^+$, and OH$^+$) for both sightlines, the relative positions stay almost the similar as shown as in Figs. 13 and 14, and the PCA h-plots for the re-

computed results are presented in D.1. From these plots, which present the PCA results, we observe three notable trends summarized below.

First, the molecular ions OH$^+$, H$_2$O$^+$, and ArH$^+$ and C$^+$ lie away from neutral molecular species HCN, HNC, CS, H$_2$S, C$_2$H, and c-C$_3$H$_2$ and HCO$^+$ in the h-plots. The first three mentioned molecular ions and C$^+$ are considered to be tracers of gas with small molecular fractions, especially ArH$^+$, which traces gas with a molecular fraction $\lesssim 10^{-3}$ (Schilke et al. 2014; Jacob et al. 2020). In Figs. 15 and 16, the similarity coefficients between the group of hydride ions and the group of neutral molecules show that these two groups are poorly correlated (cooler colors).

W3(OH), PC-1 vs. PC-2
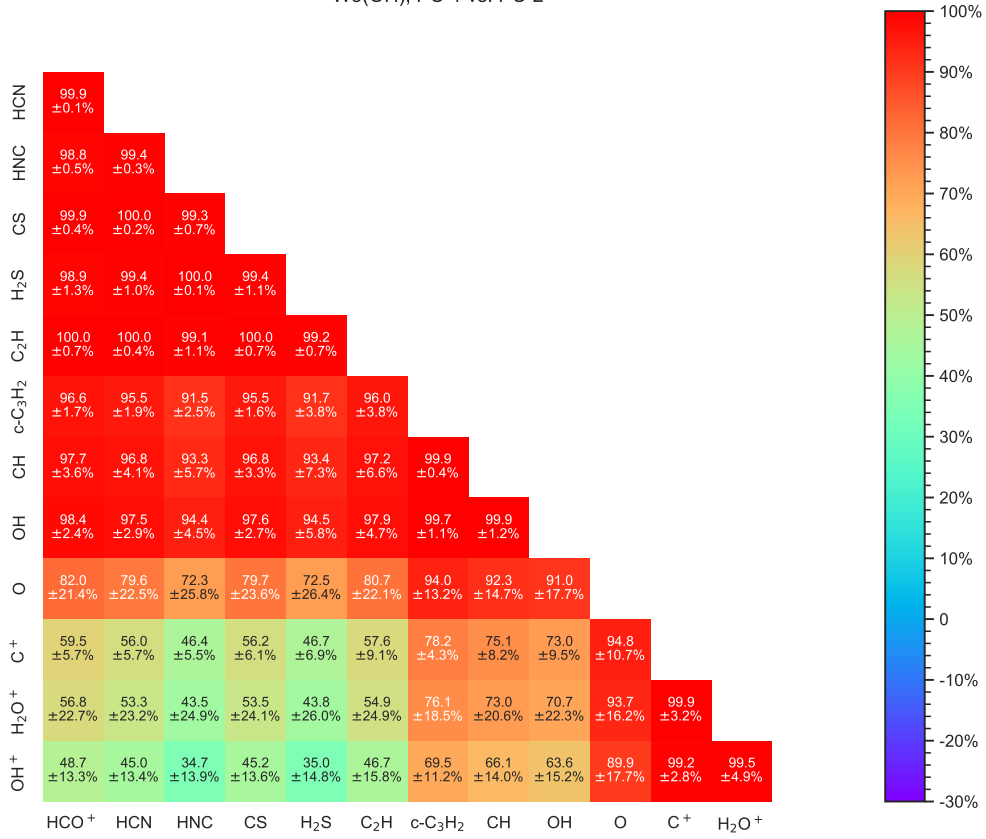
W3 IRS5, PC-1 vs. PC-2
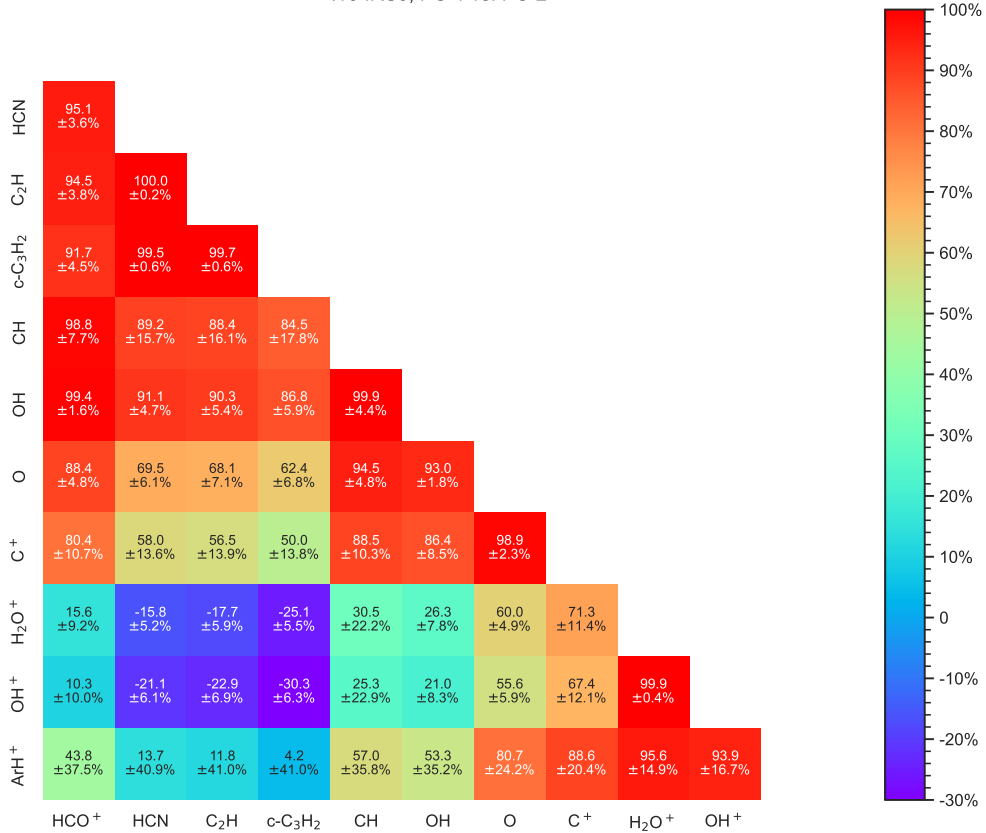
Fig. 15: Cosine similarities showing correlation between two pairs of species in the circle plots for PC-1 versus PC-2 toward W3(OH) (top) and W3 IRS5 (bottom).
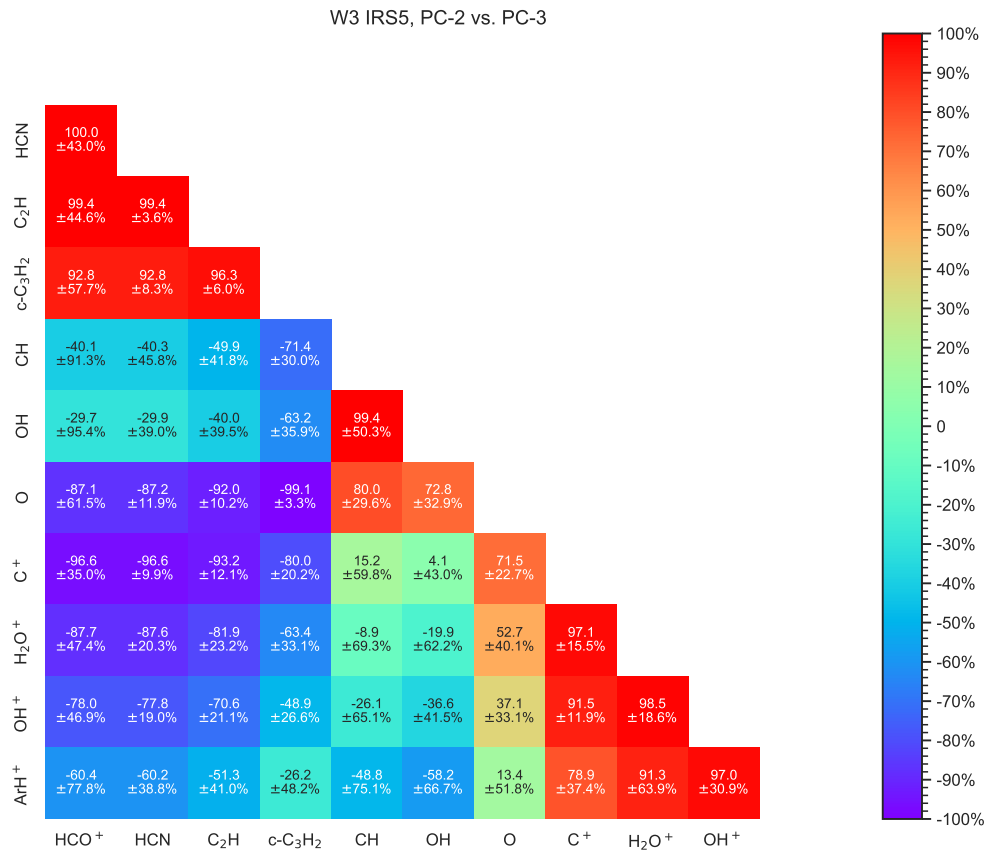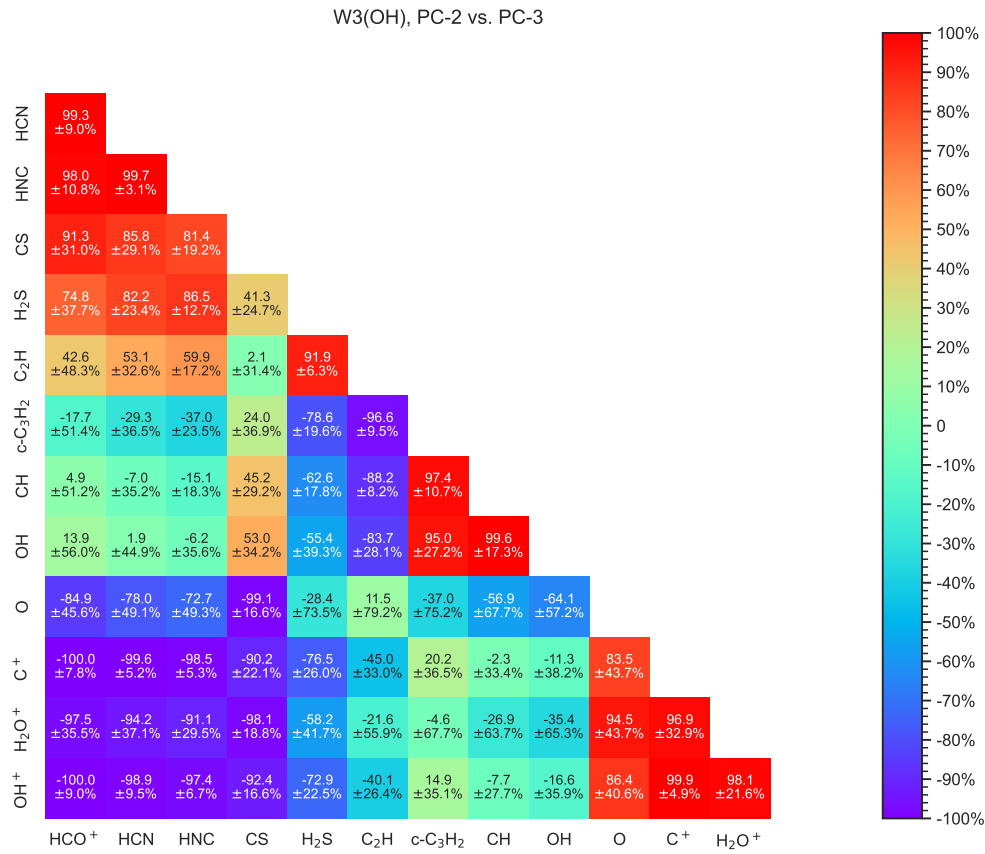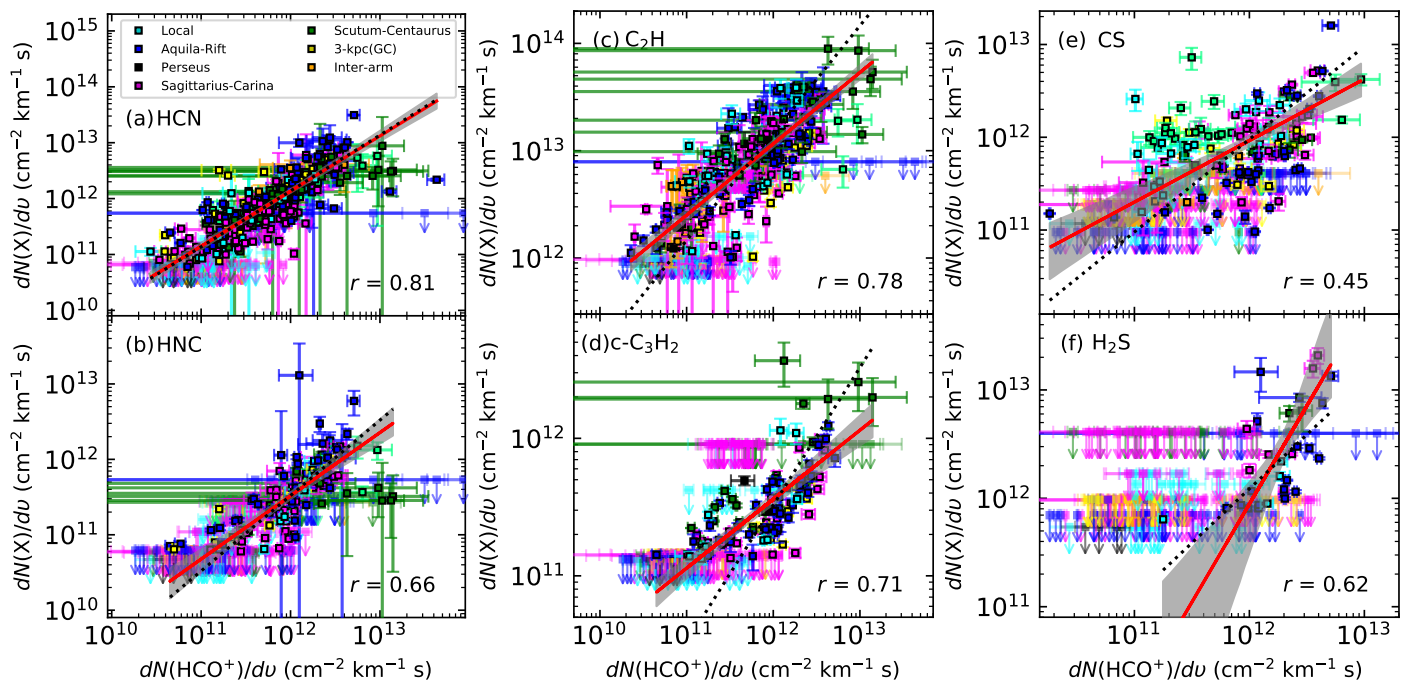
Fig. 16: Cosine similarities showing correlation between two pairs of species in the circle plots for PC-2 versus PC-3 toward W3(OH) (top) and W3 IRS5 (bottom).

Fig. 17: Comparisons of column densities in $0.8\,\mathrm{km\,s^{-1}}$ velocity channel bins for seven molecular species; (a) HCN versus HCO$^+$, (b) HNC versus HCO$^+$, (c) C$_2$H versus HCO$^+$, (d) c-C$_3$H$_2$ versus HCO$^+$, (e) CS versus HCO$^+$, and (f) H$_2$S versus HCO$^+$. The color codes correspond to specific spiral arms (local arm in cyan, Perseus arm in black, Aquila-Rift in blue, Sagittarius-Carina arm in magenta, Scutum-Centaurus arm in green, inter-arm regions in orange). All symbols without black edges indicate upper limits for nondetections, while the data points above the detection threshold are marked with black edges. In addition, the blue-green colored points indicate clouds that belong to the $135\,\mathrm{km\,s^{-1}}$ arm located beyond the Galactic center, toward G10.47+0.03. The black dotted lines represent the median value of the column density ratio in each panel. Uncertainties in the derived channel-wise column densities are presented as error bars. The red lines present a best-fit taking into account uncertainties of column densities. The gray areas are 2σ confidence interval for the best fit (red lines) with errors.
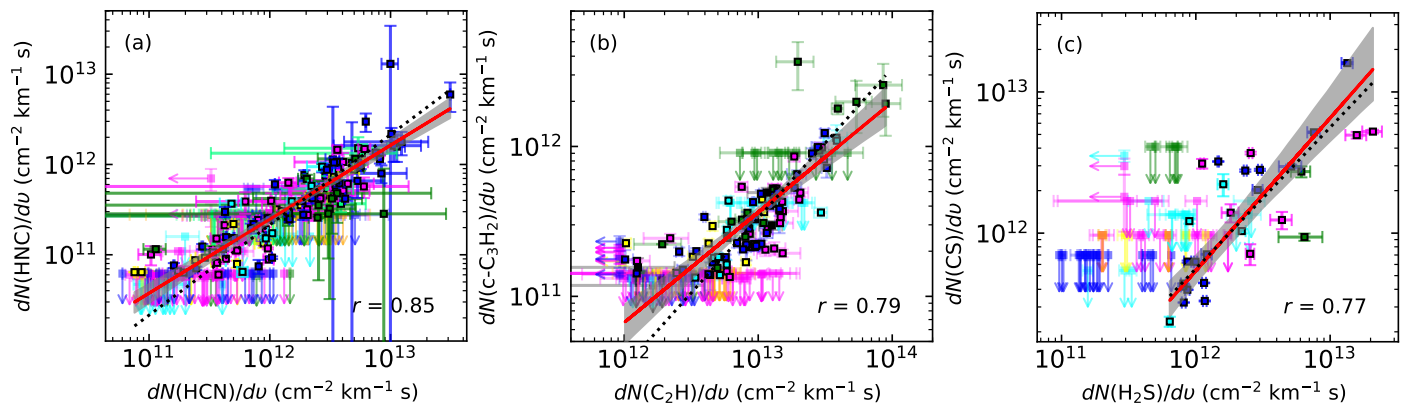
Fig. 18: Same as Fig. 17 but for (a) HCN versus HNC, (b) C$_2$H versus c-C$_3$H$_2$, and (c) CS versus H$_2$S.

On the other hand, all the species *within* each group have very similar distributions, as shown by the warm colors in the heat maps. Clearly, HCO$^+$ traces the same gas as that traced by neutral molecules, showing correlation coefficients higher than 92 % in the PC-1 versus PC-2 heat map.

Second, the sulfur-bearing species, CS and H$_2$S, lie close to the neutral molecular species rather than to the molecular ions in the h-plots, and exhibit significant similarities as shown in Figs. 15 and 16. Such a pattern is also found for other sight-lines, W31C and W49N (Neufeld et al. 2015). In agreement with Neufeld et al. (2015), we find the abundances of these two sulfur-bearing species to peak in regions of larger molecular fraction

rather than in regions traced by C$^+$ and the hydride ions OH$^+$, H$_2$O$^+$, and ArH$^+$.

Third, the vectors for CH and OH lie very close to each other in all the h-plots shown in Figs. 13 and 14. Their correlation coefficients exceed 99.9 % (Figs. 15 and 16). In addition, these molecules lie reasonably close to oxygen in the h-plots. The vectors corresponding to these three species lie between the neutral and ion molecules in both the h-plots, with the vectors for CH and OH located closer to those for the other neutral species and the vector for O located closer to those for the ionized species. CH is considered a good tracer for H$_2$ because it is present in gas dominated by both atoms and molecules (Gerin et al. 2010; Wiesemeyer et al. 2018; Jacob et al. 2019). On the other hand,
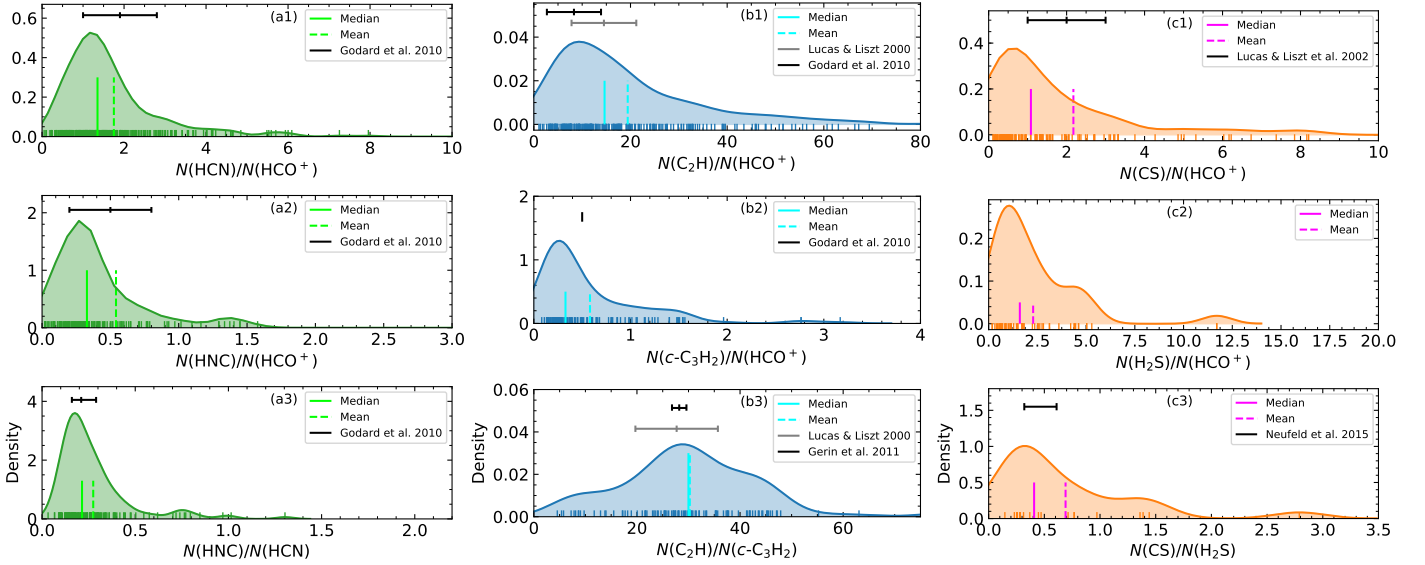
Fig. 19: Kernel density estimate (KDE) distributions of the channel-wise column density ratios. Black and gray bars indicate unweighted mean ratio values measured from previous studies of absorption lines (Lucas & Liszt 2000, 2002; Godard et al. 2010; Gerin et al. 2011; Neufeld et al. 2015). Median and mean values of the KDE distributions are marked by solid and dashed vertical lines (in lime, cyan, and fuchsia).

the vector for O tends to lie closer to those of the molecular ions that are found in gas with small molecular fractions.

5.2. Column densities and abundances

In Fig. 17, we compare channel-wise column densities for all sightlines – except for NGC 7538 IRS1 and HGAL0.55−0.85, toward which only HCO^+ is detected – to investigate whether the column densities show a linear relationship and whether there is any noticeable variation associated with specific spiral- or inter-arm regions. Due to high noise levels and contamination by emission lines, we have fewer detections for H_2S and CS. To obtain a reasonable number of data points required for reliable statistical results, we constrain the detection thresholds of their column densities to the 1.5 rms and 2 rms levels for H_2S and CS, respectively, while for the remaining five molecules, we adopt a 2.5 rms threshold to mitigate uncertainties caused by poor sensitivity.

The comparison of $dN(HCN)/dv$ and $dN(HCO^+)/dv$ in Fig. 17 (a) shows the best correlation, with a Pearson correlation coefficient (r) of 0.81. $dN(C_2H)/dv$ in Fig. 17 (c) has the second-best correlation with $dN(HCO^+)/dv$, $r = 0.78$: both these values differ from zero at a very high level of statistical significance. Along the sightlines toward extragalactic sources, both HCN and C_2H also show such good correlations and are considered to be proxies for the total column density of H_2 (Liszt & Lucas 2001; Lucas & Liszt 2000). In Figs. 17 (b) and (d), $dN(HNC)/dv$ and $dN(c-C_3H_2)/dv$ show moderate correlations ($r = 0.66 - 0.71$) with $dN(HCO^+)/dv$. In contrast, the two sulfur-bearing molecules appear to be less correlated ($r = 0.45 - 0.62$) with $dN(HCO^+)/dv$, as shown in Figs. 17 (e) and (f). On the other hand, all the species show better correlations between the same chemical families as seen in the subplots of Fig. 18, with correlation coefficients which are 0.85 for (a) $dN(HCN)/dv$ versus $dN(HNC)/dv$, 0.79 for (b) $dN(C_2H)/dv$ versus $dN(c-C_3H_2)/dv$, and 0.77 for (c) $dN(CS)/dv$ versus $dN(H_2S)/dv$. Such strong correlations between the same chemical families (HCN and HNC, C_2H and $c-C_3H_2$, as well as CS and H_2S, in Fig 18) have also

been found in other diffuse and translucent clouds in the galactic plane and the solar neighborhood (Lucas & Liszt 2000; Liszt & Lucas 2001; Lucas & Liszt 2002; Gerin et al. 2011; Godard et al. 2010; Neufeld et al. 2015).

Table 7: Median, mean and standard deviation of the column density ratios for the seven species studied in this work.

Ratio	Median	Mean	SD[†]
$N(HCN)/N(HCO^+)$	1.37	1.78	1.68
$N(HNC)/N(HCO^+)$	0.33	0.49	0.89
$N(HNC)/N(HCN)$	0.21	0.27	0.20
$N(C_2H)/N(HCO^+)$	14.06	19.81	18.28
$N(c-C_3H_2)/N(HCO^+)$	0.33	0.57	0.53
$N(C_2H)/N(c-C_3H_2)$	29.99	30.26	13.57
$N(CS)/N(HCO^+)$	0.95	1.99	3.33
$N(H_2S)/N(HCO^+)$	1.22	2.07	2.13
$N(CS)/N(H_2S)$	0.56	0.73	0.58

Notes. [†] SD is the standard deviation. For H_2S and CS, the detection threshold lowers to 1.5× rms, and 2× rms levels, respectively, while ratios of the other species are obtained from data restricted by > 2.5× rms level.

In Figs. 17 and 18 the black dotted straight lines have a slope that represents the average column density ratio between any two given species. The red solid lines are the best fits to the data (only including the data points above the detection thresholds), including column density uncertainties, shown as error bars on the plots. The gray areas represent the 2σ confidence interval of the best-fit uncertainties. These uncertainties are obtained by resampling the data points and then iteratively fitting the resampled data sets. Comparing $dN(HCO^+)/dv$ versus $dN(HCN)/dv$, we find that the median value and the best-fit agree fairly well. For the other cases, comparing different chemical groups, the best fit lines are not as steep as the lines representing the median. Such discrepancies become significant when comparing sulfur-containing molecules (CS and H_2S) with HCO^+, shown in plots (e) and (f) of Fig. 17 since their relationships are weakly corre-

Table 8: Derived column densities over specific velocity intervals.

Source	v_{LSR} range (km s^{-1})	$N(H_2)$ (10^{21}cm^{-2})	$N(HCO^+)$ (10^{12}cm^{-2})	$N(HCN)$ (10^{12}cm^{-2})	$N(HNC)$ (10^{12}cm^{-2})	$N(CS)$ (10^{12}cm^{-2})	$N(H_2S)$ (10^{13}cm^{-2})	$N(C_2H)$ (10^{13}cm^{-2})	$N(c\text{-}C_3H_2)$ (10^{12}cm^{-2})
W3 IRS5	−24, −18	$0.37^{+0.10}_{-0.10}$	$1.11^{+0.31}_{-0.30}$	$1.67^{+0.50}_{-0.49}$	...	...	...	$2.17^{+0.80}_{-0.69}$	$0.79^{+0.08}_{-0.08}$
	−6, −1	$0.08^{+0.01}_{-0.01}$	$0.24^{+0.03}_{-0.03}$	...	...	...	...	...	...
	−1, 5	$0.27^{+0.06}_{-0.06}$	$0.82^{+0.18}_{-0.18}$	...	...	...	...	...	...
W3(OH)	−23, −15	$0.07^{+0.03}_{-0.03}$	$0.22^{+0.09}_{-0.09}$	$0.08^{+0.06}_{-0.08}$	...	...	...	$0.30^{+0.01}_{-0.01}$	$0.13^{+0.01}_{-0.13}$
	−14, −7	$0.60^{+0.05}_{-0.05}$	$2.24^{+0.20}_{-0.20}$	$2.71^{+0.22}_{-0.22}$	$0.36^{+0.03}_{-0.03}$	...	...	$1.01^{+0.02}_{-0.02}$	$0.52^{+0.03}_{-0.03}$
	−7, 3	$0.87^{+0.10}_{-0.10}$	$3.44^{+0.48}_{-0.47}$	$3.72^{+0.41}_{-0.36}$	$0.78^{+0.04}_{-0.04}$	$2.67^{+0.15}_{-0.15}$	$0.34^{+0.02}_{-0.02}$	$4.57^{+0.41}_{-0.41}$	$1.36^{+0.10}_{-0.10}$
NGC 6334 I	0, 12^a	$4.79^{+2.32}_{-2.56}$	$25.84^{+15.39}_{-15.39}$	$9.17^{+0.53}_{-0.53}$	$1.35^{+0.15}_{-0.14}$	...	...	$1.98^{+0.43}_{-0.40}$	$0.72^{+0.25}_{-0.23}$
HGAL0.55−0.85	−14, −4^a	$0.56^{+0.28}_{-0.29}$	$2.04^{+1.26}_{-1.18}$	...	...	...	...	...	...
G09.62+0.19	9, 20	$46.14^{+45.78}_{-32.94}$	$922.76^{+915.66}_{-658.84}$	$13.4^{+0.56}_{-0.56}$	$4.20^{+0.64}_{-0.64}$	...	$5.66^{+17.06}_{-4.99}$	...	...
	20, 29	$2.29^{+0.65}_{-0.69}$	$10.82^{+3.72}_{-3.72}$	$24.80^{+3.93}_{-3.93}$	$14.46^{+23.68}_{-13.18}$	...	$2.25^{+0.66}_{-0.66}$	$13.34^{+7.83}_{-7.83}$	...
	62, 73	$0.82^{+0.62}_{-0.59}$	$3.23^{+3.06}_{-2.50}$	...	...	...	...	...	...
G10.47+0.03	−18, −9	$0.54^{+0.14}_{-0.14}$	$1.61^{+0.42}_{-0.42}$	$3.59^{+1.13}_{-1.13}$	...	...	...	...	...
	−9, 3	$2.00^{+0.82}_{-0.89}$	$9.21^{+4.63}_{-4.63}$	$15.95^{+7.50}_{-7.50}$	...	$2.65^{+0.32}_{-0.32}$	...	...	...
	3, 7	$0.65^{+0.15}_{-0.16}$	$2.45^{+0.69}_{-0.69}$	$7.18^{+7.31}_{-5.63}$	$1.17^{+0.32}_{-0.32}$	$4.46^{+0.82}_{-0.82}$	...	$1.85^{+0.27}_{-0.27}$	...
	7, 14	$2.64^{+0.59}_{-1.01}$	$12.83^{+5.58}_{-5.58}$	$20.99^{+12.26}_{-12.26}$	$3.38^{+0.82}_{-0.82}$	$5.44^{+0.81}_{-0.81}$	...	$12.51^{+4.56}_{-4.47}$	...
	14, 19	$0.95^{+0.20}_{-0.21}$	$3.83^{+0.96}_{-0.96}$	$3.62^{+4.78}_{-2.53}$	$1.54^{+0.39}_{-0.39}$	...	...	$2.49^{+1.45}_{-1.24}$	...
	19, 28	$1.52^{+0.38}_{-0.40}$	$6.70^{+2.01}_{-2.01}$	$9.57^{+7.96}_{-7.81}$	...	...	...	$17.59^{+2.06}_{-1.82}$	...
	28, 32	$1.71^{+0.75}_{-0.82}$	$7.67^{+4.11}_{-4.11}$	$7.92^{+3.76}_{-3.76}$	...	...	...	$11.05^{+1.20}_{-1.20}$	...
	32, 44	$2.53^{+0.74}_{-0.78}$	$12.20^{+4.31}_{-4.31}$	$36.84^{+22.83}_{-22.79}$	$4.87^{+1.38}_{-1.38}$	...	...	$22.93^{+8.24}_{-5.39}$	...
	44, 51	$0.06^{+0.03}_{-0.06}$	$0.18^{+0.08}_{-0.18}$	...	...	...	...	...	...
	82, 94	$0.23^{+0.07}_{-0.05}$ ^{b}	$0.70^{+0.20}_{-0.14}$	$22.05^{+2.23}_{-2.23}$	...	...	...	...	...
	114, 133	$1.26^{+0.27}_{-0.28}$ ^{b}	$5.36^{+1.38}_{-1.38}$	$9.75^{+3.56}_{-3.56}$	...	$9.58^{+0.96}_{-0.96}$	...	...	...
	137, 151	$0.85^{+0.15}_{-0.16}$	$3.37^{+0.73}_{-0.73}$	$7.05^{+2.11}_{-2.11}$	...	$13.44^{+2.94}_{-2.93}$	...	...	...
	151, 159	$4.02^{+1.47}_{-1.57}$	$21.02^{+9.33}_{-9.33}$	$19.50^{+13.7}_{-13.7}$	$3.08^{+0.92}_{-0.92}$	$13.78^{+2.30}_{-2.30}$	...	$4.23^{+1.43}_{-1.41}$	...
	159, 164	$0.24^{+0.06}_{-0.06}$	$0.71^{+0.18}_{-0.18}$	$1.81^{+0.47}_{-0.47}$	...	$4.49^{+0.54}_{-0.54}$	...	...	...
	164, 175	$0.22^{+0.04}_{-0.04}$	$0.65^{+0.13}_{-0.13}$	$1.15^{+0.81}_{-0.54}$	...	$7.44^{+1.02}_{-1.02}$	...	...	...

Notes. $N(H_2)$ is derived using $N(HCO^+)$; $N(H_2) = N(HCO^+)/3 \times 10^{-9}$ for a case with $N(HCO^+) < 2.8 \times 10^{12}$ cm^{-2}, $N(H_2) = N(HCO^+)/2 \times 10^{-8}$ for a case with $N(HCO^+) > 9.4 \times 10^{13}$ cm^{-2}, and an interpolated value between these two ranges of $N(HCO^+)$, $\log(N(H_2)) = \log(N(HCO^+)) \times \mathbf{1.64}$. The column densities derived for each species toward the remaining sources is tabulated in Appendix B. The velocity intervals are defined, based on HCO$^+$ absorption line profiles.
^{a} refers to the velocity intervals corresponding to molecular gas components associated with the background continuum sources, and thus the derived column densities of these velocity intervals indicate lower limits.
^{b} indicates the $N(H_2)$ for the velocity intervals belonging to the GC region where likely have higher $X(HCO^+)$ ($> 3.9 \times 10^{-9}$ for the central molecular zone (Riquelme et al. 2018)) than the Galactic disk regions.

lated. In addition, each color represents a different spiral-arm or intermediate arm region, or an unassigned foreground clouds, as tabulated in Table 6. For HCN, HNC, and the two small hydrocarbons, there is no apparent difference in column densities between clouds associated with the different environments. However, in panel (e) of Fig. 17 for CS, the cloud components belonging to the 135 km s^{-1} arm, marked in blue-green color, have higher $dN(CS)/dv$ compared to the other spiral arms that have $dN(HCO^+)/dv \approx 1 - 9 \times 10^{11}$ cm^{-2} km^{-1} s.

In panel (b) of Fig. 18, the two small hydrocarbons, have a nonlinear relationship for values of $dN(C_2H)/dv < 1 \times 10^{13}$ cm^{-2} km^{-1} s, which plateaus as $dN(c\text{-}C_3H_2)/dv$ increases ($\approx 1 - 4 \times 10^{11}$ cm^{-2} km^{-1} s). As $dN(C_2H)/dv$ increases beyond the inflection point from $\approx 1 \times 10^{13}$ cm^{-2} km^{-1} s to higher C_2H column densities, the column densities of these small hydrocarbons follow a linear relationship. Taking into account fitting uncertainties, the flat slope between the column densities of the two small hydrocarbons at lower values of $N(C_2H)$ remains constant.

Figure 19 shows kernel density estimate (KDE) plots to examine distributions of channel-wise column density ratios. With the KDE method the probability density function of sample data can be estimated based on kernels as weights. KDE provides smooth profiles of the density, unlike histograms. Here we used a Gaussian kernel placed on each ratio data point as marked by the short vertical lines (in green, blue, and orange colors). The KDEs, shown as solid curves, are the sum of all kernels at

each column density ratio. The solid and dashed vertical lines are median and mean values, respectively, of the distributions. The values for the median and mean as well as the standard deviations (SDs) are listed in Table 7. We compare the values with ratios obtained from previous absorption line studies (Lucas & Liszt 2000, 2002; Godard et al. 2010; Gerin et al. 2011; Neufeld et al. 2015), which are marked by black and gray bars. From this work we get mean ratios of 1.78, 0.49, and 0.27 for $N(HCN)/N(HCO^+)$, $N(HNC)/N(HCO^+)$ and $N(HNC)/N(HCN)$, respectively. The mean ratios of $N(HCN)/N(HCO^+)$ (Fig. 19 (a1)) and $N(HNC)/N(HCO^+)$ (Fig. 19 (a2)) are very similar to values from the previous studies, while the mean ratio of $N(HNC)/N(HCN)$ (Fig. 19 (a3)) is slightly higher than that derived by Liszt & Lucas (2001) and Godard et al. (2010) of (0.21±0.71) but within the error range. The median $N(HNC)/N(HCN)$ ratio of 0.22 from this survey agrees well with the other studies. According to Liszt & Lucas 2001, a small $N(HNC)/N(HCN)$ ratio such as 0.2 is expected to indicate warmer gas at higher A_v or denser gas conditions. In addition, this ratio distribution is very similar to the distribution of HNC/HCN, between 0.01 and 1.0, toward star-forming regions (e.g., Graninger et al. 2014) and Orion-KL/the OMC regions (e.g., Schilke et al. (1992) and Hacar et al. 2020; HNC/HCN $\sim$ 0.013 − 0.2). Toward some sightlines, $N(HNC)/N(HCN)$ ratios are between 0.2 and 1.0. This range might imply that the observed HCN and HNC trace warmer regions and/or inner parts
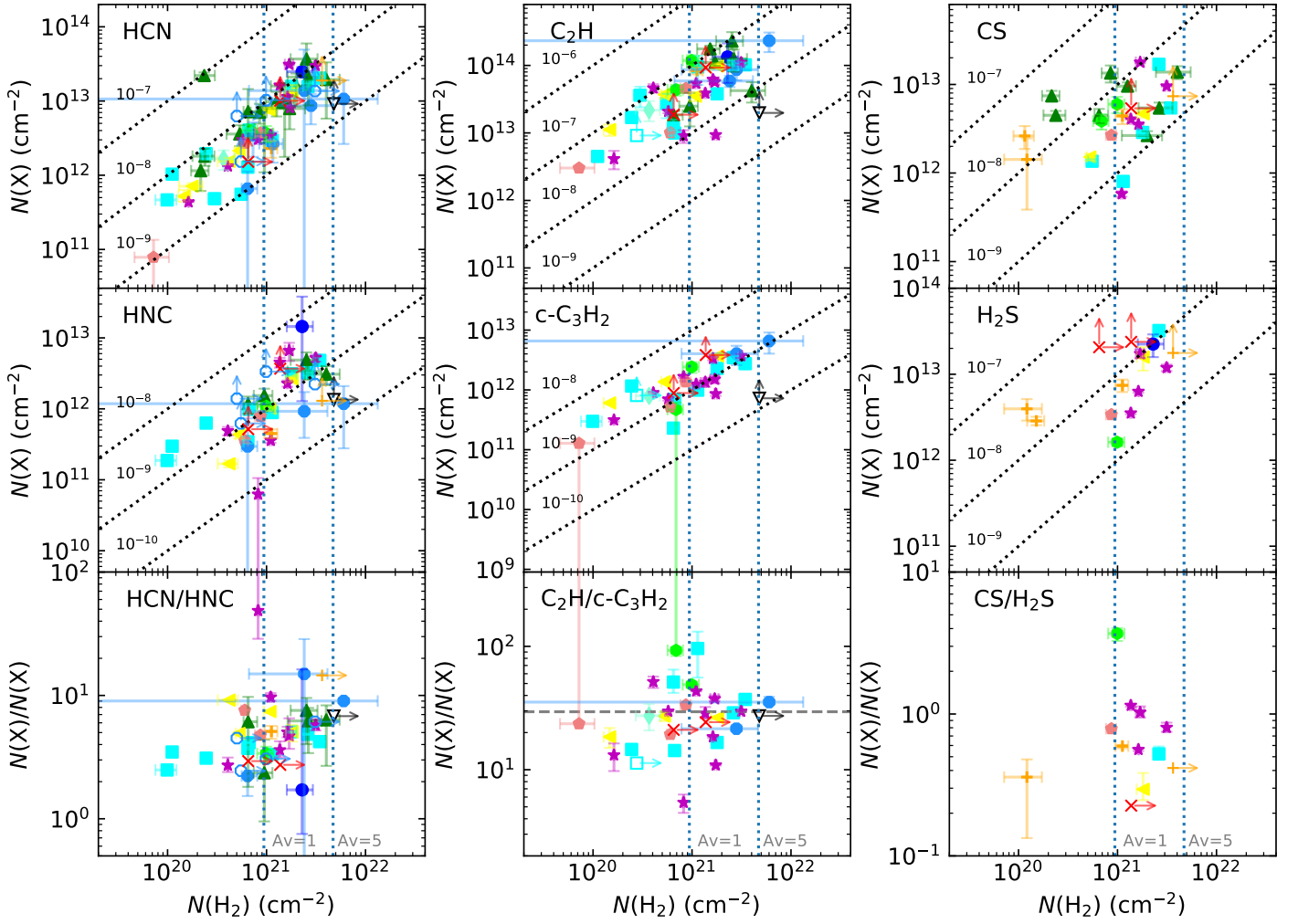
Fig. 20: Comparison of the column density of the presented molecular species and $N(H_2)$. Each colored symbol represents different individual clouds in the sightline toward the observed background continuum sources (DR21: Red X, G09.62+0.19: Blue circle, G10.47+0.03: Green up-triangle, G19.61−0.23: Cyan square, G29.96−0.02: Yellow left-triangle, G31.41+0.31: Lime hexagon, G32.80+0.19: Magenta star, G45.07+0.13: Orange cross, NGC 6334 I: Black down-triangle, W3 IRS5: Aquamarine thin diamond, W3(OH): Light-coral pentagon, W43 MM1: Dodger-blue octagon). Filled and unfilled markers indicate foreground components and molecular envelope components, respectively. For the molecular envelope components, only lower limits are marked by arrows instead of fitting uncertainty bars. Black diagonal dotted lines represent abundances of given molecules on the y-axis relative to $N(H_2)$ with their values labeled. In each panel, two vertical blue dotted lines indicate the visual extinction of 1 and 5, respectively. In the plot of $N(C_2H)/N(c\text{-}C_3H_2)$, the gray horizontal dashed line indicates a mean value of 30.26 in the column density ratio.

of diffuse molecular clouds since the high ratio of these two molecules are found toward TMC-1 (ratio of 1, Ohishi et al. 1992).

The mean ratios of the column densities of C_2H and $c\text{-}C_3H_2$ to $N(HCO^+)$ (Figs. 19 (b1) and (b2)) and $N(C_2H)/N(c\text{-}C_3H_2)$ (Fig. 19 (b3)) are 19.81, 0.57, and 30.26. The mean value of the column density ratios of the two small hydrocarbons agrees well with previously measured values of 27.7±0.8 and 28.2±1.4 from Lucas & Liszt (2000) and Gerin et al. (2011), as shown in Fig. 19 (b3). For $N(CS)$ versus $N(HCO^+)$, $N(H_2S)$ versus $N(HCO^+)$ and $N(CS)$ versus $N(H_2S)$, the mean ratios are 1.99, 2.07, and 0.73, respectively. Like other species, these two sulfur-containing molecules have mean ratios greater than their median values (Figs. 19 c1, c2, and c3, and Table 7). The previously measured mean ratios of 2±1 for $N(CS)/N(HCO^+)$ (Lucas & Liszt 2002) and 0.32−0.61 for $N(CS)/N(H2S)$ (Neufeld et al. 2015) come very close to the measurements obtained here.

The detected absorption features of simple molecular species studied in this work have different velocity components, and some of them have CO emission counterparts, shown in Fig. 10. Therefore, to characterize the properties of individual diffuse and translucent foreground clouds, we integrated column densities over given velocity intervals to identify individual cloud components and list the average column densities for all 14 line-of-sight sources in Tables 8 and B.1. Figure 20 shows the column densities (upper and middle image) of HCN, HNC, C_2H, $c\text{-}C_3H_2$, CS, and H_2S and column density ratios (lower panel) as a function of $N(H_2)$. The H_2 column density is derived from $N(HCO^+)$ using a HCO^+ abundance of 3×10^{-9} relative to H_2 ($N(H_2) = N(HCO^+)/3\times10^{-9}$) (Lucas & Liszt 2000; Liszt et al. 2010) for $N(HCO^+) < 2.8 \times 10^{12}$ cm^{-2}, 2×10^{-8} ($N(H_2) = N(HCO^+)/2 \times 10^{-8}$) for $N(HCO^+) > 9.4 \times 10^{13}$ cm^{-2}, and an interpolated value between these two ranges of $N(HCO^+)$, $\log(N(H_2)) = \log(N(HCO^+))\times1.64$, because $N(HCO^+)$ and $N(H_2)$ does not follow a linear correlation in regions with higher H_2 column den-

Table 9: Median value of abundances relative to H_2 and $N(H_2)$ of each targeted species X observed toward different cloud components.

Species	All clouds[a]			Diffuse cloud			Translucent cloud		
	#	$N(X)/N(H_2)$	$N(H_2)$ (cm^{-2})	#	$N(X)/N(H_2)$	$N(H_2)$ (cm^{-2})	#	$N(X)/N(H_2)$	$N(H_2)$ (cm^{-2})
HCN	64	4.80×10^{-9}	9.69×10^{20}	31	4.49×10^{-9}	5.26×10^{20}	30	6.13×10^{-9}	1.72×10^{21}
HNC	42	1.17×10^{-9}	1.11×10^{21}	16	1.02×10^{-9}	5.77×10^{20}	23	1.40×10^{-9}	1.80×10^{21}
C_2H	46	3.84×10^{-8}	1.09×10^{21}	20	4.11×10^{-8}	5.40×10^{20}	24	3.82×10^{-8}	1.72×10^{21}
c-C_3H_2	33	1.36×10^{-9}	8.68×10^{20}	17	1.93×10^{-9}	5.26×10^{20}	14	1.23×10^{-9}	1.72×10^{21}
CS	28	3.26×10^{-9}	1.20×10^{21}	10	9.28×10^{-9}	5.40×10^{20}	18	2.77×10^{-9}	1.74×10^{21}
H_2S	16	7.67×10^{-9}	1.50×10^{21}	4	2.53×10^{-8}	4.02×10^{20}	11	6.62×10^{-9}	1.69×10^{21}

Notes. [a] includes all cloud types (dense, translucent, and diffuse). The # columns indicate the number of foreground components used for the statistics. All features associated with background sources are excluded in these calculations because the column densities of these features only represent lower limits.

sity (Thiel et al. 2019). Visual extinctions of 1 and 5 are marked with vertical blue dotted lines and estimated using A_v (mag) $= N(H_2)/(9.4 \times 10^{20} \text{ cm}^{-2})$ (Thiel et al. 2019). In Fig. 20, symbols of the same color indicate foreground clouds in the same direction, and the black diagonal lines represent lines of constant abundance for each individual molecular species presented. We exclude the cloud component in the velocity range between 9.0 and 20.2 km s^{-1} for G09.62+0.19 as its extremely large $N(HCO^+)$ value of 9.2×10^{14} cm^{-2} indicates that the component does not originate from either diffuse or translucent clouds.

On the left-hand side of Fig. 20, $N(HCN)$ and $N(HNC)$ increase as $N(H_2)$ (A_v) increases, but slightly nonlinearly. In particular, the HCN abundance increases briefly relative to H_2 at $N(H_2) \gtrsim 10^{21}$ cm^{-2}, regions considered to be translucent clouds. Liszt & Lucas 2001 also reported such nonlinear relationships of the column densities of CN-bearing molecules. They show a rapid increase in abundances of both the CN-bearing molecules detected toward sightlines with $N(HCO^+) \gtrsim 10^{12}$ cm^{-2} equivalent to $N(H_2) \sim 0.3 - 0.5 \times 10^{21}$ cm^{-2} by assuming an abundance of 3×10^{-9} relative to H_2, against extra-galactic continuum sources. The lower-left panel shows the column density ratios of HCN and HNC as a function of $N(H_2)$, and these ratios tend to increase slightly toward higher molecular hydrogen column densities, tracing higher visual extinction regions of molecular clouds.

As expected, in the middle plots of Fig. 20, the column densities of the two small hydrocarbons (C_2H and c-C_3H_2) show tight linear correlations with $N(H_2)$, and their abundance varies only a little across different environments from diffuse ($A_v < 1$) gas to dense molecular gas ($A_v > 5$), through translucent molecular gas regions in between. The C_2H abundance measured here lies in an approximate range from 10^{-8} to 10^{-7}, while that of c-C_3H_2 is pretty much within $10^{-9} - 10^{-8}$. These abundances relative to H_2 agree well with the $X(C_2H) \sim 4 - 7 \times 10^{-8}$ (Lucas & Liszt 2000; Gerin et al. 2011) and X(c-C_3H_2) $\sim 2 - 3 \times 10^{-9}$ (Liszt et al. 2012) in diffuse gas, measured in previous absorption line studies. As seen in the bottom plot, the $N(C_2H)/N$(c-C_3H_2) ratios in individual cloud components of our targets are constant over the values of $N(H_2)$ probed, with an average column density ratio of $N(C_2H)/N$(c-C_3H_2) ~ 30.26 indicated by the gray horizontal dashed line. This average ratio agrees well with the values obtained by Lucas & Liszt 2000.

As already seen in Fig. 17, $N(CS)$ and $N(H_2S)$ also show poor correlations with $N(H_2)$ in Fig. 20, in contrast to the column densities of HCN, HNC, C_2H and c-C_3H_2, although $N(CS)$ has some degree of correlation with $N(H_2)$. The abundances of CS and H_2S derived in diffuse clouds are higher $> 10^{-8}$ than those in

translucent clouds ($10^{-9} <$ abundance $< 10^{-8}$). However, apart from the fitting uncertainties, the derived column densities of CS and H_2S probably contain higher uncertainties than the lines of the other species, for example, due to poor sensitivities, as seen in Fig 8. Therefore, it is difficult to conclude that the abundance of these sulfur-bearing species is higher toward diffuse clouds than toward translucent clouds. We need more observational data points with higher sensitivity toward more diffuse clouds to confirm this hypothesis since we only have a small sample (10 for CS and 4 for H_2S). The CS abundances toward the Galactic translucent clouds are in good agreement with X(CS) $\sim 4 \times 10^{-9}$ determined for high latitude diffuse clouds in the solar neighborhood (Lucas & Liszt 2002) in spite of the sulfur chemistry being different in these environments. Likewise, the abundances of H_2S are similar with $X(H_2S)$ determined from diffuse clouds in different parts of the Galactic plane (Neufeld et al. 2015). In the plot of $N(CS)/N(H_2S)$, a majority of the foreground clouds with detections for both these molecules are identified as translucent clouds but still associated with relatively less dense regions ($A_v \sim 1 - 3$ mag). In addition, the column density ratios do not show any correlation with the total hydrogen column density in the sightlines studied here.

### 5.3. Variation of abundances along the sightline

Figures 21, E.1 and E.2 show variations in molecular abundance relative to $N(H_2)$ in the lower panel and $N(H_2)$ in the upper panel as a function of velocity along 12 sightlines. Two sightlines, HGAL0.55−0.85 and NGC 7538 IRS1, are not plotted here because only the HCO^+ transition is seen in absorption toward these two sources. The column density of H_2 and the abundance of the molecules relative to H_2 are average values over given velocity ranges (see tables 8 and B.1). In the upper panel, visible extinctions of 1 and 5 are indicated with horizontal dotted lines separating the three types of molecular gas clouds; diffuse clouds below $A_v < 1.0$, translucent clouds in $1.0 < A_v < 5.0$, while regions with $A_v > 5$ are considered to be dense molecular clouds. The black arrows imply that the derived column densities and abundances may be underestimated within the velocity ranges marked with gray shaded areas that are affected by spectral emission features. Abundances of the considered species are shown in the lower panels with different colored markers; green circles for HCN, purple asterisks for HNC, orange up triangles for CS, red left triangles for H_2S, cyan cross for C_2H, and gray hexagons for c-C_3H_2.

Overall, some variations in abundance along the selected sightlines are found. These variations are not attributed to vari-
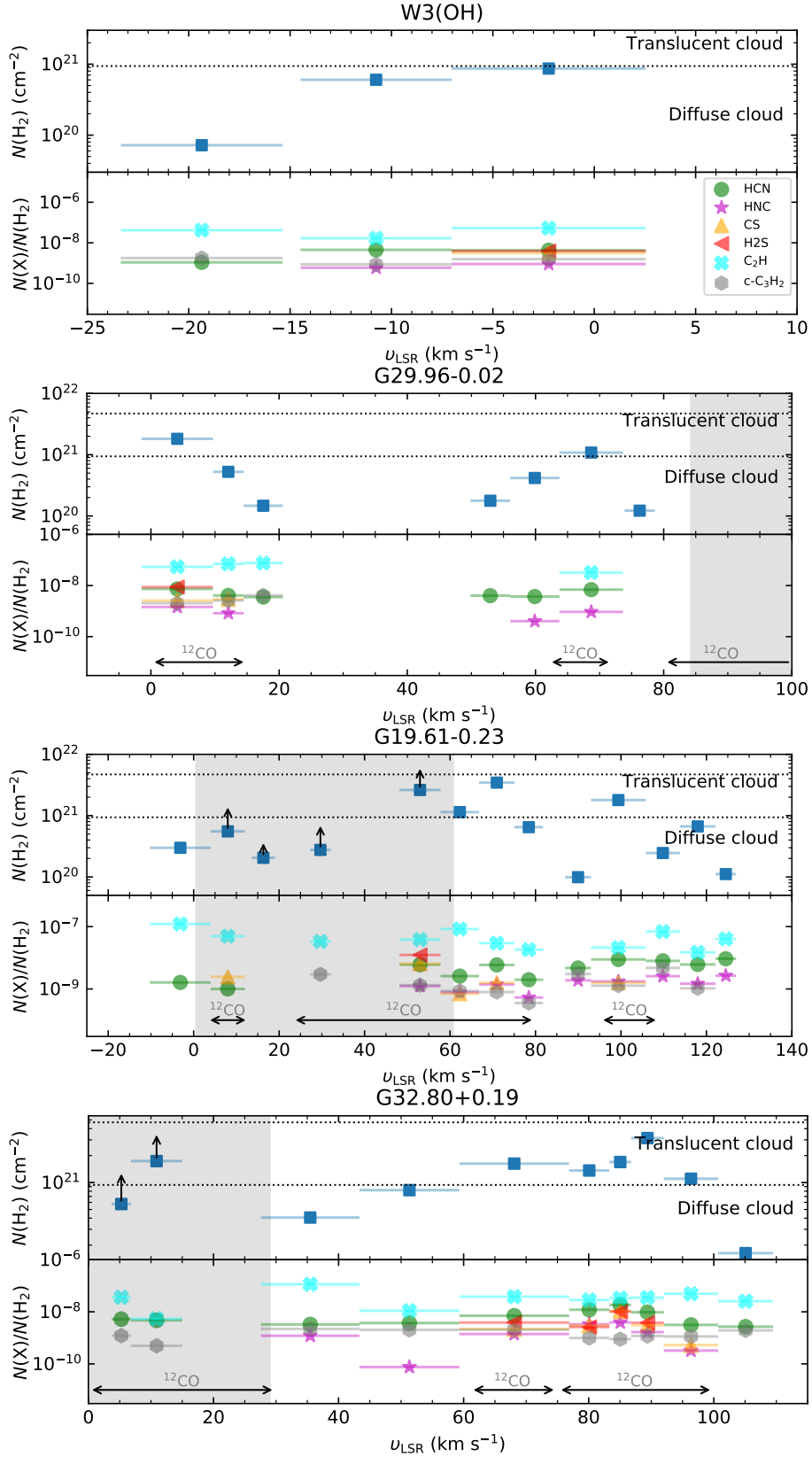
Fig. 21: $N(H_2)$ and $N(X)/N(H_2)$ ratio integrated over specific velocity intervals from top to bottom toward W3(OH), G29.96−0.02, G19.61−0.23, and G32.80+0.19. Different species are labeled with different symbols and colors as shown in the legend displayed in the right-hand corner of the top panel. The gray areas indicate the velocity ranges of the emission lines. In the upper panels, the dotted horizontal lines correspond to A_v of 1 and 5, respectively. In the lower panels, the black horizontal arrows indicate the velocity ranges in which CO emission features have been detected from archival data at its given sensitivity. All the other sources are displayed in Figs. E.1 and E.2.
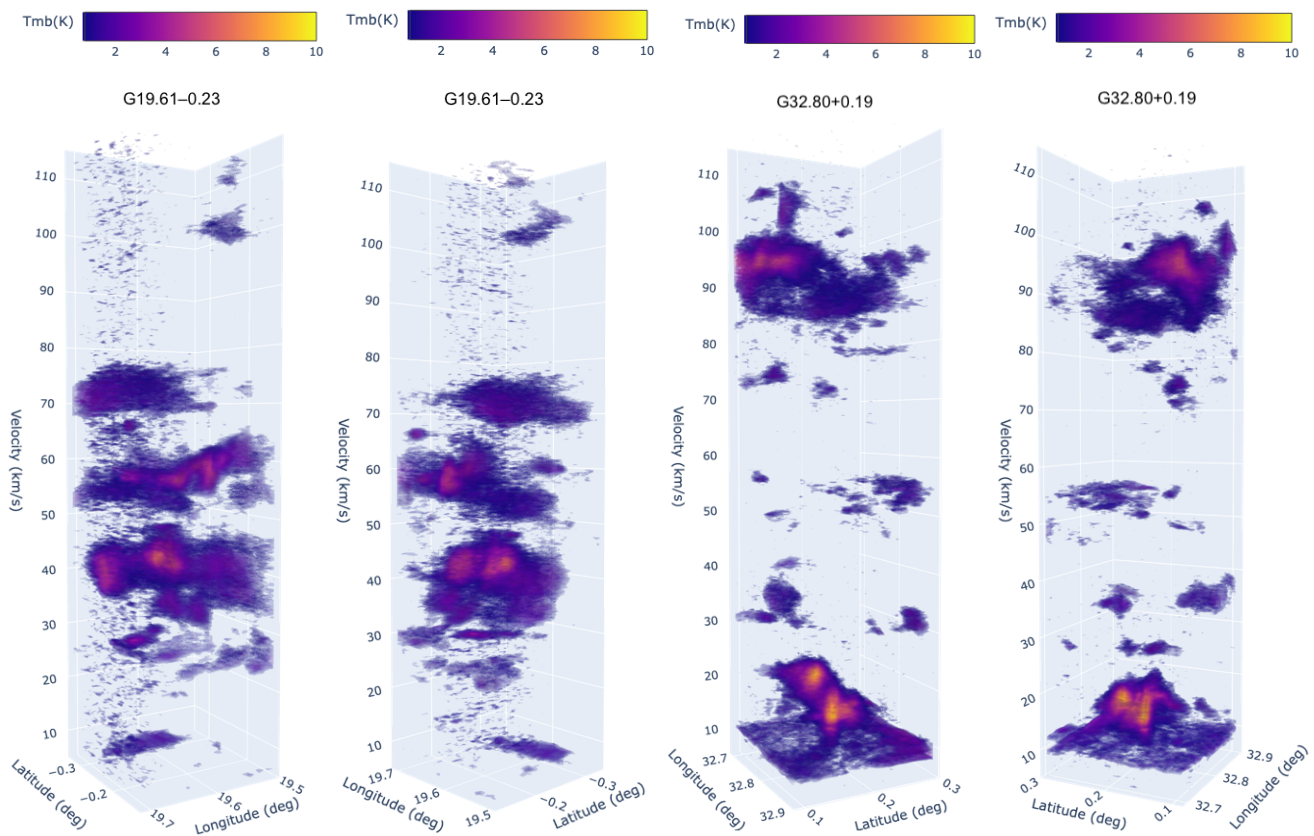
Fig. 22: Position-position-velocity images of ^{13}CO emission using data taken from the GRS survey toward two selected sightlines; G19.61−0.23 (approximately 90° angle difference between left two images) and G32.80+0.19 (approximately 90° angle difference between right two images).

able rms levels since the variability of abundances appears in all the sightlines, nor fitting uncertainties. Despite potential uncertainties, the abundances of C_2H and c-C_3H_2 change little and are instead consistent in both velocity ranges or between diffuse and translucent clouds. In Table 9 the mean abundances of these small hydrocarbons are surprisingly similar, while $N(H_2)$ of diffuse clouds is smaller than that of translucent clouds by a factor of 4. We note that all calculations for the median values do not include the absorption features associated with background continuum sources. The median abundances of HCN and HNC do not show significant changes from diffuse to translucent clouds. In contrast, we note that $X(H_2S)$ (with a median of 2.5×10^{-8}) and $X(CS)$ (with a median of 9.3×10^{-9}) in diffuse clouds are significantly higher than in translucent clouds; median values of $X(H_2S)$ and $X(CS)$ are 2.8×10^{-9} and 6.6×10^{-9}, respectively. These species' higher abundances in diffuse clouds are already noticeable in Figs. 20, 21, E.1, and E.2. Overall, the mean or median abundances of the discussed species fit well within the ranges of values derived for high-altitude clouds or other clouds in the Galactic plane, considering the uncertainties. The abundance variations toward individual clouds may signify the influences of their environments which might be affected by, for example, pristine infalling gas in low metallicity (De Cia et al. 2021), the high UV fields ($\sim 5 \times 10^5$ in Habing units, Rizzo et al. 2003) from embedded massive star-forming regions, or outflows, or the feedback from young high mass stars at the late stage of molecular clouds (e.g., influence of turbulence and shocks caused by expanding HII regions and stellar winds). All these effects could, to different degrees, mix gas from star-forming re-

gions with diffuse or/and translucent gas, and result in significant time dependent chemistry (e.g., Pilleri et al. 2013).

To understand the abundance variations along the sightlines in relation to molecular gas structures, we plot position-position-velocity images of two selected sightlines (G19.61−0.23 and G32.80+0.19). Compared with other sightlines, these two sightlines have absorption features well separated from the background emission lines. As a result, absorption lines of all seven transitions are clearly detected (see Fig. 9). Figure 22 displays position-position-velocity images of ^{13}CO emission extracted over an area of $12' \times 12'$ from the GRS survey with the original spectral resolution ($0.2 \, \mathrm{km \, s^{-1}}$). Toward both sightlines, we notice complex structures of dense molecular gas rather than simple shapes like spheres or cylinders. We can clearly see dense and clumpy molecular gas structures at the systemic velocities of these sightlines (for G19.61−0.23, $v_{sys} = 41.8 \, \mathrm{km \, s^{-1}}$, and for G32.80+0.19, $v_{sys} = 15 \, \mathrm{km \, s^{-1}}$). Some foreground clouds (velocity ranges of $28 - 40 \, \mathrm{km \, s^{-1}}$ and $58.5 - 70.8 \, \mathrm{km \, s^{-1}}$ for G19.61−0.23 and $90 - 110 \, \mathrm{km \, s^{-1}}$ for G32.80+0.19) show an open ring structure. We need to study the association and interaction between diffuse material filling voids of dense molecular gas and the dense material by combining absorption and emission spectral analyses to address the abundance variations found in this work.

5.4. UV-dominated chemistry

We used the Meudon PDR code[4] (Le Petit et al. 2006; Goicoechea & Le Bourlot 2007; Gonzalez Garcia et al. 2008) to study the physical conditions of diffuse and translucent clouds in which the molecules are studied in this investigation and are produced. The Meudon PDR code simulates a plane-parallel slab cloud illuminated on both sides by assuming that the cloud is in a static state. Throughout the model cloud, the thermal and chemical profiles are computed by assuming thermal and chemical equilibrium for every location. All models simulated here are isobaric models that consider constant thermal pressure. The calculated temperature and density profiles show that the temperature in the cloud decreases with increasing density. Self and mutual shielding for H, H_2, CO, isotopologues of CO (i.e., ^{13}CO and ^{18}CO), and HD becomes vital for models of diffuse clouds. Thus, toward the foreground clouds studied in this work, the H/H_2 transition should be considered in PDR models in detail with regard to the shielding processes. Therefore, we have applied an exact radiative transfer method described in (Goicoechea & Le Bourlot 2007) to the PDR models rather than the analytical approximation to the self-shielding process in a line, described by Federman et al. (1979) (FGK approximation). In the exact method, the spherical harmonics method (Goicoechea & Le Bourlot 2007) is implemented to solve for the far-ultraviolet (FUV) radiation fields in externally and internally illuminated clouds, considering gas absorption and scattering properties by dust grains.

Table 10: Input parameters of the Meudon PDR isobaric models.

Fixed parameters	
Oxygen abundance	3.2×10^{-4}
Carbon abundance	1.3×10^{-4}
Nitrogen abundance	7.5×10^{-5}
Sulfur abundance	1.9×10^{-5}
$R_v = A_v/E(B-V)$	3.1
Gas to Dust ratio	100
Grain size distribution index	3.5
Minimum grain radius (μm)	0.003
Maximum grain radius (μm)	0.3
Free parameters	
Radiation field G_0	1 & 100
Cosmic ray ionization rate ζ (s^{-1})	5×10^{-17}, 10^{-16} & 10^{-15}
$A_{v,max}$ (mag)	0.1, 1, 5 & 10
Pressure (K cm^{-3})	10^3, 3×10^3, 5×10^3 & 10^4

Notes. The carbon and sulfur atoms are in their ionized form in the chemical file. The UV interstellar radiation field is in Mathis unit; $G_0 = 1$ corresponds to a flux of 3.03×10^{-4} ergs cm^{-2}s^{-1}.

Table 10 shows the fixed and free parameters used in the simulated PDR models. We used default values for initial abundances of elements, extinction curve (R_v), and dust properties and considered them to be fixed parameters. However, we have changed the values for the interstellar radiation field (G_0 in Mathis units), which for the solar neighborhood is $G_0 = 1$ and for FUV illuminated PDRs such as the Horsehead Nebula is $G_0 =$100 (Pety et al. 2005). The value of G_0 only changes on the observer side and is fixed to 1 for the backside of the cloud in all models. Since the observed galactic sightlines pass over different parts of the Milky Way, we assume that diffuse clouds along the sightlines are controlled by various cosmic ray ionization rate (ζ) values where ζ is the total ionization rate by cosmic rays per H_2 molecule. Therefore, we varied ζ to 5×10^{-17}, 1×10^{-16}
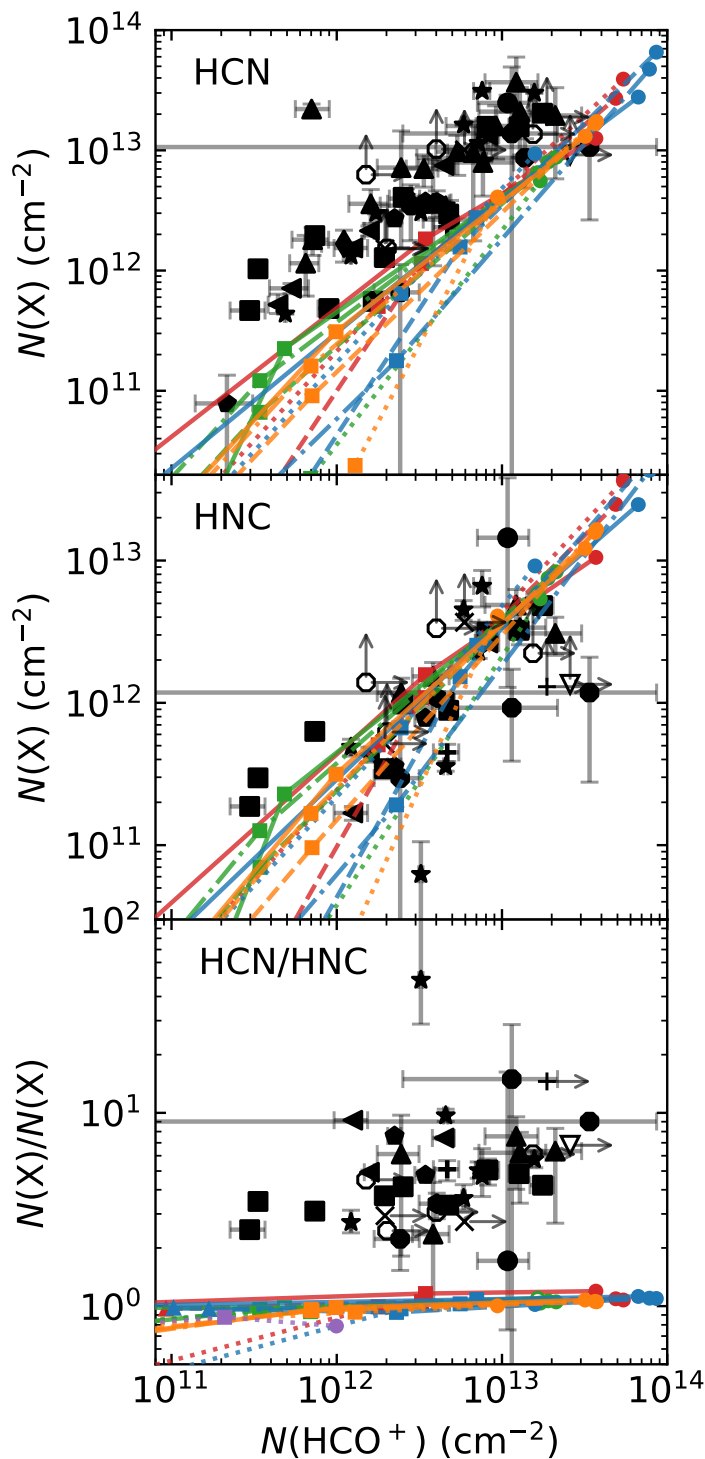
---

[4] https://ism.obspm.fr/pdr.html

---

and 1×10^{-15} s^{-1} in our models. In addition, we have assumed typical values of interstellar pressure in diffuse and translucent clouds of 1000, 3000, 5000, and 10 000 K cm^{-3} and chosen total extinctions along the plane-parallel slab of $A_v = 0.1, 1, 5$, and 10 mag. We note that in the Meudon PDR isobaric models, each velocity-integrated component listed in Tables 8 and B.1 is a separate cloud (diffuse or translucent clouds) with a uniform pressure.

Figures 23, 24 and 25 show comparisons of $N(X)$ for each species X studied and column density ratios with $N(HCO^+)$, from top to bottom, and the predicted column densities and ratios from isobaric PDR models are marked with colored symbols and lines. For the predicted values from the models, different colors indicate various radiation field strengths and cosmic-ray ionization rates; $G_0 = 1$ and $\zeta = 5 \times 10^{-17}$ s^{-1} in red, $G_0 = 100$ and $\zeta = 5 \times 10^{-17}$ s^{-1} in green, $G_0 = 1$ and $\zeta = 1 \times 10^{-16}$ s^{-1} in blue, $G_0 = 100$ and $\zeta = 1 \times 10^{-16}$ s^{-1} in orange, and $G_0 = 100$ and $\zeta = 1 \times 10^{-15}$ s^{-1} in purple. Initial pressures of 1000, 3000, 5000, and 10 000 K cm^{-3} are indicated with dotted-, dashed-, dashed-dotted-, and solid-lines, respectively. In addition, the results with different visual extinctions are represented by colored triangles ($A_v = 1$ mag), colored squares ($A_v = 5$ mag), and colored circles ($A_v = 10$ mag). We note that all the predicted column densities at $A_v = 0.1$ mag fall outside the range of column densities shown in Figs 23, 24 and 25.

5.4.1. HCO$^+$, HCN, and HNC

The top and middle plots of Fig. 23 show comparisons of two CN-bearing molecules (i.e., HCN and HNC) with $N(HCO^+)$ as well as the column densities predicted from the isobaric PDR models. For HCN, most of the models underestimate the observed quantities, only those models with $\zeta = 5 \times 10^{-17} - 1 \times 10^{-16}$ s^{-1} and an initial pressure of 10 000 K cm^{-3} result in values close to the lower limit of the observed column densities by a factor of a few higher. The modeled gas conditions are at $n_H \sim 1400 - 2000$ cm^{-3} and decrease in gas temperature at $A_v \sim 1$ mag. For HNC, all models fit reasonably within the observed column density ranges. In addition, models with $G_0 = 1$ (red and blue colors) make better predictions than those with $G_0 = 100$. The predicted $N(HCN)$, $N(HNC)$, and $N(HCO^+)$ from the isobaric models result from regions of higher visual extinction between 1 and 10 mag. In contrast, the estimated H_2 column densities from the observations correspond to lower than $A_v \le 5$ mag. These models provide reasonable predictions of column densities of these species. However, the models underestimate column densities by roughly an order of magnitude, especially for HCN and HCO$^+$. The modeled $N(HCN)/N(HNC)$ against $N(HCO^+)$ as shown in the bottom-left panel of Fig. 23, is lower than the ratios from the observations due to an underestimation of $N(HCN)$ in the isobaric PDR models.

In the isobaric PDR models, there are two main formation pathways for HCO$^+$ and the two CN-bearing molecules (see Godard et al. 2009; Gerin & Liszt 2021 for details). For HCO$^+$, the first one involves the chains, from OH + C$^+ \rightarrow$ CO$^+$ + H to CO$^+$ + $H_2 \rightarrow$ HCO$^+$ + H, and the second pathway is via H_2O + C$^+ \rightarrow$ HCO$^+$ + H. The latter reaction can also lead to the production of HOC$^+$ that can produce HCO$^+$ via hydrogenation. The formation of HCN and HNC involves nitrogen via the reaction NH + C$^+ \rightarrow$ CN$^+$ + H_2 or H $\rightarrow$ HCN$^+$ or HNC$^+$ + $H_2 \rightarrow$ HCNH$^+$; NH$_2$ + C$^+ \rightarrow$ HCN$^+$ + $H_2 \rightarrow$ HCNH$^+$. The dissociative recombination of HCNH$^+$ forms HCN and HNC. Additionally, HCN can be produced via the neutral-neutral reaction of CH$_2$ + N. As seen in Fig. 23, the chemistry involving only the UV-dominated

chemistry cannot reproduce the observed column densities of these species in diffuse and translucent clouds. In the turbulence-dominated chemistry (Godard et al. 2009, 2010, 2014) involving turbulent dissipation rate, relaxation and ion-neutral drift (Valdivia et al. 2017), several crucial endoenergetic reactions can significantly increase the abundances of important precursors of HCN, HNC, and HCO^+, such as CH^+, CH_2^+, CH_3^+ as well as NH. The TDR models from Godard et al. (2009, 2014) show a considerable increase in the formation of these three species via ion-neutral reactions, $CH^+ + N \rightarrow CN^+ + H_2 \rightarrow HCN^+$ or $HNC^+ + H_2 \rightarrow HCNH^+$; $CH_2^+ + N \rightarrow HCN^+ + H_2 \rightarrow HCNH^+$; $CH_3^+ + N \rightarrow HCNH^+$; $CH_3^+ + O \rightarrow HCO^+ + H_2$. Additionally, the reaction of CH^+ with oxygen enhances the abundance of CO^+, leading to HCO^+.

5.4.2. C_2H and $c-C_3H_2$

Figure. 24 shows comparisons between column densities predicted from isobaric PDR models and observations for C_2H and $c-C_3H_2$. Similar to the HCN and HCO^+ results, the models underestimate the column densities of these two small hydrocarbons in these foreground cloud components. Nevertheless, their observed column densities are in better agreement with values from the isobaric models corresponding to low-density gas in $n_H \approx 100 - 500 \, cm^{-3}$ up to $1000 \, cm^{-3}$. The $N(C_2H)$ toward the diffuse clouds with $N(HCO^+) < 2 \times 10^{12} \, cm^{-2}$ (corresponding to an observed $A_v \sim 1$) is close to the column densities from the isobaric models with moderate pressure values (dashed and dash-dotted green lines) of $3000 - 5000 \, K \, cm^{-3}$ giving $n_H \approx 500 - 1000 \, cm^{-3}$ and strong UV radiation of $G_0 = 100$ and $\zeta = 5 \times 10^{-17} \, s^{-1}$, for less shielded regions $A_v < 5$ (colored square symbols). By contrast, in denser regions having $N(HCO^+) > 2 \times 10^{12} \, cm^{-2}$, the low-density models (dashed lines, $n_H \approx 100 - 500 \, cm^{-3}$) with lower G_0 of 1 (red and blue colors) at high $A_v > 5$ mag seem to fit the observed column densities better. For $c-C_3H_2$, the low-density PDR models with $G_0 = 1$ only in the direction of translucent clouds predict results near the low end of the column densities obtained from the observational data, as in the case of C_2H. The comparison between $N(C_2H)/N(c-C_3H_2)$ and $N(HCO^+)$ for the models and observations show a better match than those for $N(HCN)/N(HNC)$ versus $N(HCO^+)$ but still have some discrepancy. Overall, the models with lower density and the solar neighborhood G_0 generate column densities of these hydrocarbons close to the observed values, unlike the cases of HCN, HNC, and HCO^+ which are associated better with high density gas materials. Nevertheless, the predicted column densities of the small hydrocarbons are underestimated by a factor of a few. In particular, for $c-C_3H_2$, toward diffuse clouds with $N(c-C_3H_2) < 2 \times 10^{12} \, cm^{-2}$, the discrepancy is more than about a factor of 10. In the isobaric PDR models, the predicted column densities of $c-C_3H_2$ are total column densities of ortho and para species without separate spin symmetries (with a spin-weight ratio of 3/1 for ortho/para). Thus, with consideration of this fact, the discrepancies between the observations and the models become larger.

In the PDR chemistry, C_2H is mainly produced by the recombination of $C_2H_2^+$ and $C_2H_3^+$ with electrons (e.g., Godard et al. 2009; Mookerjea et al. 2012). In addition, it is formed by the photodissociation of C_2H_2 (Lee 1984) as well as by the neutral-neutral reaction of CH_2 with atomic carbon (Turner et al. 2000; Sakai et al. 2010). For the formation of $c-C_3H_2$, once C_3H^+ is formed by reactions of C_2H_2 with C^+, C_3H^+ produces the linear and cyclic $C_3H_3^+$ isomers via reactions with H_2 (Maluendes et al. 1993). The resulting isomers produce linear and cyclic-C_3H_2 by

Fig. 23: Column densities of HCN and HNC and their column density ratio as a function of $N(HCO^+)$, with predictions from isobaric PDR models overlaid. Filled and unfilled black markers indicate foreground components and molecular envelope components observed, respectively. The arrows refer to lower limits of $N(X)$, and the markers are as same as Fig 20. Each color represents different radiation field strengths and cosmic-ray ionization rates; red: $G_0 = 1$ and $\zeta = 5 \times 10^{-17} \, s^{-1}$, green: $G_0 = 100$ and $\zeta = 5 \times 10^{-17} \, s^{-1}$, blue: $G_0 = 1$ and $\zeta = 1 \times 10^{-16} \, s^{-1}$, orange: $G_0 = 100$ and $\zeta = 1 \times 10^{-16} \, s^{-1}$, and purple: $G_0 = 100$ and $\zeta = 1 \times 10^{-15} \, s^{-1}$. Initial pressures of 1000, 3000, 5000, 10 000 K cm^{-3} are indicated with dotted-, dashed-, dashed-dotted-, and solid-lines, respectively. $A_v = 1$, 5, and 10 mag are marked with colored triangles, squares, and circles, respectively.
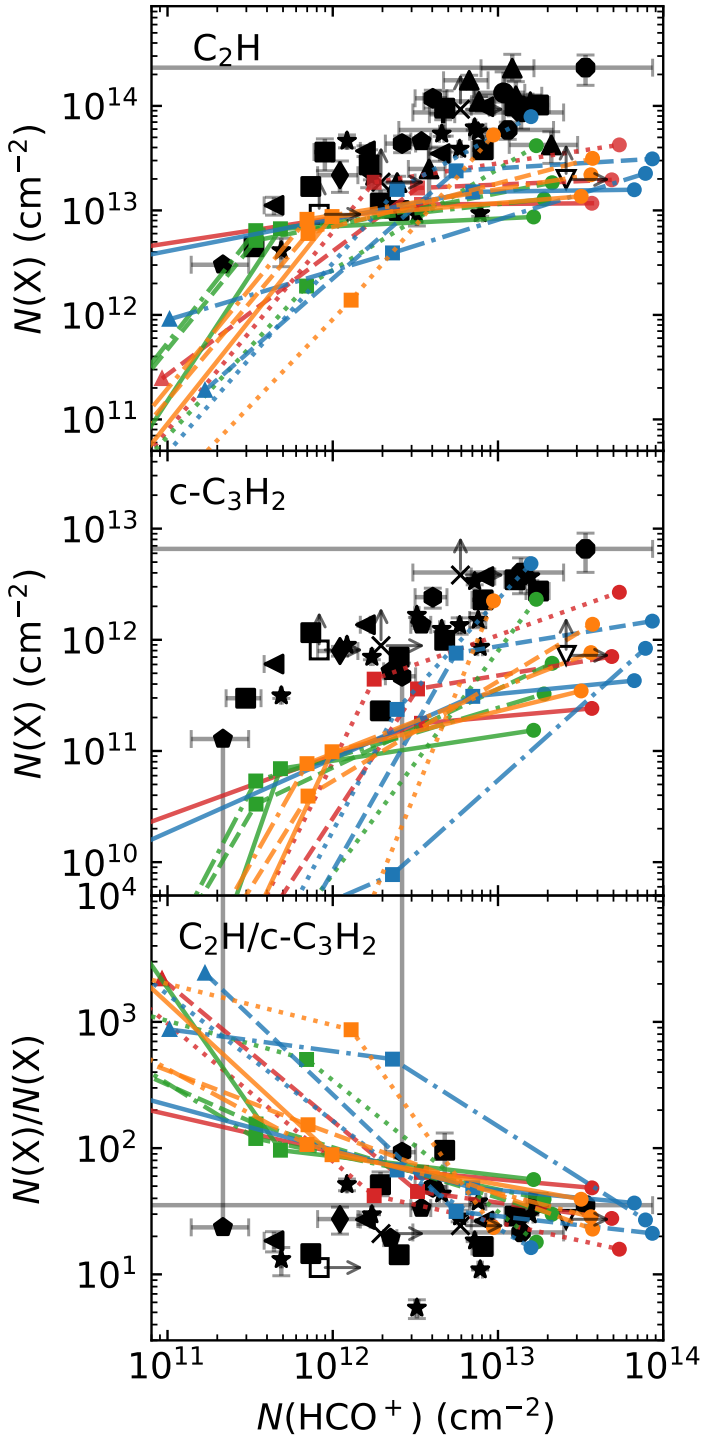
Fig. 24: Column densities of C_2H and c-C_3H_2 and their column density ratio as a function of $N(HCO^+)$, with predictions from isobaric PDR models overlaid. All symbols and lines used to represent the models are the same as Fig. 23.

dissociative recombination (Fossé et al. 2001). In addition, the recombination of C_3H^+ also contributes to the abundances of C_2H (Guzmán et al. 2015).

Similar to HCN, HNC, and HCO^+, turbulence-dominated chemistry can considerably increase the abundances of C_2H and c-C_3H_2 by enhancing abundances of their precursor, C_2H^+ which is formed from CH_2 via hydrogenation reactions. Not only that, but also the endoenergetic reaction of $C_2^+ + H_2$ with

$-\Delta E/k = 1260$ K (Godard et al. 2009) increases the abundance of C_2H. Aside from the contribution of turbulent dissipation, the formation of small hydrocarbons possibly involves the top-down hydrocarbon chemistry that describes polycyclic aromatic hydrocarbons (PAHs) and small carbonaceous grains being broken down by UV erosion into small hydrocarbons that react in the gas phase (e.g., Pety et al. 2005; Gerin et al. 2011; Guzmán et al. 2015).

5.4.3. CS and H_2S

Figure 25 shows comparisons of the column densities of the two sulfur-bearing species and their column density ratios with $N(HCO^+)$. The top panel shows a good agreement between the predicted and derived column densities of CS. All the models with a wide range of physical parameters ($G_0 =1$ and 100, $\zeta = 5 \times 10^{-17}$ and 1×10^{-16} s^{-1}, and gas pressures of 1000–10 000 K cm^{-3}) broadly fit the derived column densities. In particular, toward translucent cloud components, the models with $G_0 = 1$, $\zeta = 1 \times 10^{-16}$ s^{-1}, and pressure of $3000 - 5000$ K cm^{-3} (blue dashed- and dashed-dotted-lines) well fit the derived values from the observations. The primary pathway of CS formation is the dissociative recombination reaction of HCS^+ and electrons, which, however, leads to CS + H in 19 % of reactions (Montaigne et al. 2005). There are two formation routes for HCS^+, either through $CH + S^+ \rightarrow CS^+$; $CS^+ + H_2 \rightarrow HCS^+$ in the PDR route or through $S + CH_3 \rightarrow HCS^+$ in the TDR route (Neufeld et al. 2015). We have found that the results of our PDR models are obtained in more shielded gas ($n_H \sim 100 - 1000$ cm^{-3} and $A_v > 1$ mag) compared to the more diffuse gas ($n_H = 50$ cm^{-3} and $A_v = 0.4$ mag) considered in the TDR and shock models presented in Neufeld et al. (2015). The destruction of CS reacting with H_3^+ directly contributes to the formation of HCS^+ alongside other CS destruction pathways driven by photoionization and ion-exchange reactions.

The middle panel in Fig. 25 shows that the isobaric PDR models underestimate the observed column densities of H_2S. We also note that, as in the case of c-C_3H_2, the H_2S column densities predicted from the models show the total column densities of both ortho and para species, while the observational measurements refer to the column densities of only ortho-H_2S. In UV-dominated chemistry, reactions of $S^+ + H_2 \rightarrow H_2S^+ + e^- \rightarrow H_2S$ is the main pathway to form H_2S. However, in low A_v (< 0.5 mag) regions, the endothermic reaction of $SH + H_2 \rightarrow H_2S + h\nu$ (with $-\Delta E/k = 6862$ K) becomes the predominant formation pathway for H_2S (e.g., Sternberg & Dalgarno 1995; Neufeld et al. 2015). In addition, the abundances of H_2S^+, which is the precursor of H_2S, can be enhanced by two other endothermic reactions: $SH^+ + H_2 \rightarrow H_2S^+ + H$ ($-\Delta E/k = 6380$ K), and $S^+ + H_2 \rightarrow H_2S^+ + h\nu$ ($-\Delta E/k = 9860$ K). Similar to the species discussed in the previous sections, these endothermic reactions activated by turbulent dissipation or shocks (Neufeld et al. 2015) could significantly enhance the abundances of H_2S toward the observed sightlines. However, TDR or shock models alone cannot address the high observed column densities (Neufeld et al. 2015). This implies that another route for the formation of H_2S is needed. This route could be related to dust grain-surface chemistry (e.g., Navarro-Almaida et al. 2020; Cazaux et al. 2022). Sulfur is depleted onto dust grains (Ruffle et al. 1999) because sulfur mainly exists as S^+ (Sternberg & Dalgarno 1995) and most dust grains are negatively charged. According to the gas-grain models of Navarro-Almaida et al. (2020), the chemical desorption of H_2S (via solid-H + solid-HS → H_2S) can explain the high H_2S abundances observed in translucent clouds (cloud
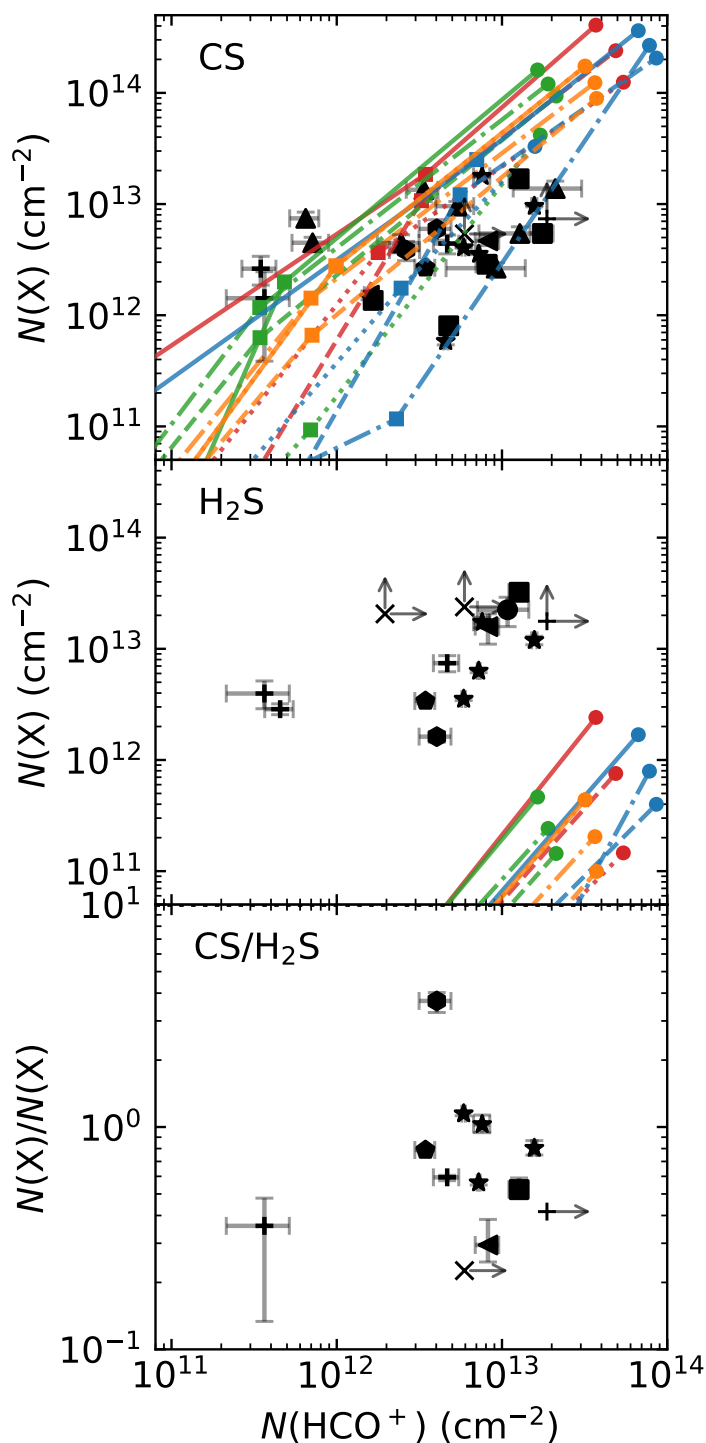
Fig. 25: Column densities of CS and H$_2$S and their column density ratio as a function of N(HCO$^+$), with predictions from isobaric PDR models overlaid. All markers and lines for the models are same as Fig. 23.

6. Summary and conclusions

Using the IRAM 30 m telescope, we have studied seven simple molecular species – HCO$^+$, HCN, HNC, C$_2$H, c-C$_3$H$_2$, CS, and H$_2$S – in absorption toward 15 submillimeter sources in the Milky Way. We have detected HCO$^+$ absorption lines in the direction of all 14 sources that show detectable millimeter wave continuum radiation, identifying 78 foreground gas components. A significant number of sightlines also have detectable absorption lines of HCN (12 sightlines), HNC (11 sightlines), C$_2$H (12 sightlines), and c-C$_3$H$_2$ (9 sightlines), CS (8 sightlines) and H$_2$S (6 sightlines). Our sensitivity to CS and H$_2$S is reduced by the presence of significant emission line contamination near the CS frequency and the poorer S/N ratios achieved at the higher H$_2$S transition frequency.

Using principal component analysis to investigate correlations among the species observed with the IRAM 30 m telescope and 7 other species observed with SOFIA (Paper I), we find that C$^+$ and the hydride ions OH$^+$, H$_2$O$^+$, and ArH$^+$ are poorly correlated with neutral molecules and HCO$^+$. Sulfur-bearing molecules, CS and H$_2$S, appear to be better correlated with the neutral molecules than with hydride ions, which are tracers of gas with small molecular fractions. In addition, CH, OH, and O tend to be partially associated with both mostly molecular and predominantly atomic gas.

For the column densities, we find that N(HCN) and N(HNC) increase nonlinearly with N(H$_2$). While the abundances of the two molecules increase linearly in diffuse clouds ($A_v < 1$), their abundances suddenly increase in regions with N(H$_2$) $\gtrsim$ 10^{21} cm^{-2}, where gas is further shielded against ultraviolet radiation. In contrast, C$_2$H and c-C$_3$H$_2$ do not increase as rapidly, and their column densities show a close correlation with N(HCO$^+$). Moreover, the column density ratios of the two small hydrocarbons remain constant over the N(H$_2$) range probed and lie close to the ratios measured previously toward external galaxies. Interestingly, we find that the abundances of CS and H$_2$S in diffuse clouds are 5 – 10 times higher than in translucent clouds ($A_v \approx 1$). This might imply the onset of sulfur depletion at around A_v of 1. Variations in the abundances of observed species along sightlines exist, but finding specific patterns is difficult as the abundances are influenced by the surrounding environment.

We reasonably reproduce column densities of HNC and CS using isobaric PDR models, but the column densities of the other molecular species observed here, except for H$_2$S, are underestimated by a factor of 2 – 10. Any of the models failed to reproduce the column densities of H$_2$S. As explored in previous studies on diffuse clouds, TDR models, which include pathways involving endoenergetic chemical reactions, could explain the discrepancy between the predicted and observed column densities of HCN, HCO$^+$, C$_2$H, and c-C$_3$H$_2$. For H$_2$S, additional formation routes, for example grain-surface production and chemical desorption of H$_2$S, may play an important role in increasing the abundance of H$_2$S in diffuse and translucent clouds.

edges, n(H$_2$) < 10^4 cm^{-3}) surrounding the dark clouds TMC-1 and Barnard 1b. Although the clouds in our sample have different physical conditions to these objects, the addition of chemical desorption may also help explain the high H$_2$S abundances derived toward the Galactic sightlines in our sample.

References

Araya, E., Hofner, P., Churchwell, E., & Kurtz, S. 2002, ApJS, 138, 63

Bellomi, E., Godard, B., Hennebelle, P., et al. 2020, A&A, 643, A36

Bialy, S. & Burkhart, B. 2020, ApJ, 894, L2

Bialy, S., Burkhart, B., & Sternberg, A. 2017, ApJ, 843, 92

Bialy, S., Neufeld, D., Wolfire, M., Sternberg, A., & Burkhart, B. 2019, ApJ, 885, 109

Bialy, S. & Sternberg, A. 2019, ApJ, 881, 160

Cazaux, S., Carrascosa, H., Muñoz Caro, G. M., et al. 2022, A&A, 657, A100

De Cia, A., Jenkins, E. B., Fox, A. J., et al. 2021, Nature, 597, 206

Elia, D., Merello, M., Molinari, S., et al. 2021, MNRAS, 504, 2742

Elia, D., Molinari, S., Schisano, E., et al. 2017, MNRAS, 471, 100

Endres, C. P., Schlemmer, S., Schilke, P., Stutzki, J., & Müller, H. S. P. 2016, Journal of Molecular Spectroscopy, 327, 95

Federman, S. R., Glassgold, A. E., & Kwan, J. 1979, ApJ, 227, 466

Fish, V. L., Reid, M. J., Wilner, D. J., & Churchwell, E. 2003, ApJ, 587, 701

Flagey, N., Goldsmith, P. F., Lis, D. C., et al. 2013, ApJ, 762, 11

Fossé, D., Cernicharo, J., Gerin, M., & Cox, P. 2001, ApJ, 552, 168

Furuya, R. S., Cesaroni, R., & Shinnaga, H. 2011, A&A, 525, A72

Gerin, M., de Luca, M., Goicoechea, J. R., et al. 2010, A&A, 521, L16

Gerin, M., Kaźmierczak, M., Jastrzebska, M., et al. 2011, A&A, 525, A116

Gerin, M. & Liszt, H. 2021, A&A, 648, A38

Gerin, M., Liszt, H., Neufeld, D., et al. 2019, A&A, 622, A26

Gerin, M., Neufeld, D. A., & Goicoechea, J. R. 2016, ARA&A, 54, 181

Godard, B., Falgarone, E., Gerin, M., Hily-Blant, P., & de Luca, M. 2010, A&A, 520, A20

Godard, B., Falgarone, E., & Pineau Des Forêts, G. 2009, A&A, 495, 847

Godard, B., Falgarone, E., & Pineau des Forêts, G. 2014, A&A, 570, A27

Goicoechea, J. R. & Le Bourlot, J. 2007, A&A, 467, 1

Gonzalez Garcia, M., Le Bourlot, J., Le Petit, F., & Roueff, E. 2008, A&A, 485, 127

Gorai, P., Das, A., Shimonishi, T., et al. 2021, ApJ, 907, 108

Graninger, D. M., Herbst, E., Öberg, K. I., & Vasyunin, A. I. 2014, ApJ, 787, 74

Guzmán, V. V., Pety, J., Goicoechea, J. R., et al. 2015, ApJ, 800, L33

Hacar, A., Bosman, A. D., & van Dishoeck, E. F. 2020, A&A, 635, A4

Hogerheijde, M. R., de Geus, E. J., Spaans, M., van Langevelde, H. J., & van Dishoeck, E. F. 1995, ApJ, 441, L93

Hunter, T. R., Phillips, T. G., & Menten, K. M. 1997, ApJ, 478, 283

Jackson, J. M., Rathborne, J. M., Shah, R. Y., et al. 2006, The Astrophysical Journal Supplement Series, 163, 145

Jacob, A. M., Menten, K. M., Wiesemeyer, H., et al. 2019, A&A, 632, A60

Jacob, A. M., Menten, K. M., Wyrowski, F., Winkel, B., & Neufeld, D. A. 2020, A&A, 643, A91

Jacob, A. M., Neufeld, D. A., Schilke, P., et al. 2022, ApJ, 930, 141

Kolpak, M. A., Jackson, J. M., Bania, T. M., Clemens, D. P., & Dickey, J. M. 2003, ApJ, 582, 756

Le Petit, F., Nehmé, C., Le Bourlot, J., & Roueff, E. 2006, ApJS, 164, 506

Lee, L. C. 1984, ApJ, 282, 172

Liszt, H., Gerin, M., Beasley, A., & Pety, J. 2018, ApJ, 856, 151

Liszt, H., Gerin, M., & Grenier, I. 2019, A&A, 627, A95

Liszt, H. & Lucas, R. 2001, A&A, 370, 576

Liszt, H. & Lucas, R. 2004, A&A, 428, 445

Liszt, H., Sonnentrucker, P., Cordiner, M., & Gerin, M. 2012, ApJ, 753, L28

Liszt, H. S., Lucas, R., & Pety, J. 2006, A&A, 448, 253

Liszt, H. S., Pety, J., Gerin, M., & Lucas, R. 2014, A&A, 564, A64

Liszt, H. S., Pety, J., & Lucas, R. 2010, A&A, 518, A45

Liu, T., Evans, N. J., Kim, K.-T., et al. 2020, MNRAS, 496, 2790

Liu, T., Lacy, J., Li, P. S., et al. 2017, ApJ, 849, 25

Lucas, R. & Liszt, H. S. 2000, A&A, 358, 1069

Lucas, R. & Liszt, H. S. 2002, A&A, 384, 1054

Maluendes, S. A., McLean, A. D., Yamashita, K., & Herbst, E. 1993, J. Chem. Phys., 99, 2812

Margulès, L., Lewen, F., Winnewisser, G., Botschwina, P., & Müller, H. S. P. 2003, Phys. Chem. Chem. Phys., 5, 2770

Molinari, S., Schisano, E., Elia, D., et al. 2016, A&A, 591, A149

Möller, T., Bernst, I., Panoglou, D., et al. 2013, A&A, 549, A21

Möller, T., Endres, C., & Schilke, P. 2017, A&A, 598, A7

Montaigne, H., Geppert, W. D., Semaniak, J., et al. 2005, ApJ, 631, 653

Mookerjea, B., Hassel, G. E., Gerin, M., et al. 2012, A&A, 546, A75

Müller, H. S. P., Schlöder, F., Stutzki, J., & Winnewisser, G. 2005, Journal of Molecular Structure, 742, 215

Müller, H. S. P., Thorwirth, S., Roth, D. A., & Winnewisser, G. 2001, A&A, 370, L49

Navarro-Almaida, D., Le Gal, R., Fuente, A., et al. 2020, A&A, 637, A39

Neufeld, D. A., Godard, B., Gerin, M., et al. 2015, A&A, 577, A49

Nony, T., Louvet, F., Motte, F., et al. 2018, A&A, 618, L5

Ohishi, M., Irvine, W. M., & Kaifu, N. 1992, in Astrochemistry of Cosmic Phenomena, ed. P. D. Singh, Vol. 150, 171

Pety, J. 2005, in SF2A-2005: Semaine de l'Astrophysique Francaise, ed. F. Casoli, T. Contini, J. M. Hameury, & L. Pagani, 721

Pety, J., Teyssier, D., Fossé, D., et al. 2005, A&A, 435, 885

Pickett, H. M., Poynter, R. L., Cohen, E. A., et al. 1998, J. Quant. Spectr. Rad. Transf., 60, 883

Pilleri, P., Treviño-Morales, S., Fuente, A., et al. 2013, A&A, 554, A87

Polehampton, E. T., Menten, K. M., Brünken, S., Winnewisser, G., & Baluteau, J. P. 2005, A&A, 431, 203

Reid, M. J., Menten, K. M., Brunthaler, A., et al. 2019, ApJ, 885, 131

Riquelme, D., Amo-Baladrón, M. A., Martín-Pintado, J., et al. 2018, A&A, 613, A42

Rizzo, J. R., Fuente, A., Rodríguez-Franco, A., & García-Burillo, S. 2003, ApJ, 597, L153

Ruffle, D. P., Hartquist, T. W., Caselli, P., & Williams, D. A. 1999, MNRAS, 306, 691

Sakai, N., Saruwatari, O., Sakai, T., Takano, S., & Yamamoto, S. 2010, A&A, 512, A31

Schilke, P., Neufeld, D. A., Müller, H. S. P., et al. 2014, A&A, 566, A29

Schilke, P., Walmsley, C. M., Pineau Des Forets, G., et al. 1992, A&A, 256, 595

Schneider, N., Csengeri, T., Bontemps, S., et al. 2010, A&A, 520, A49

Schuller, F., Urquhart, J. S., Csengeri, T., et al. 2021, MNRAS, 500, 3064

Snow, T. P. & McCall, B. J. 2006, ARA&A, 44, 367

Sormani, M. C. & Magorrian, J. 2015, MNRAS, 446, 4186

Sternberg, A. & Dalgarno, A. 1995, ApJS, 99, 565

Thiel, V., Belloche, A., Menten, K. M., et al. 2019, A&A, 623, A68

Turner, B. E., Herbst, E., & Terzieva, R. 2000, ApJS, 126, 427

Umemoto, T., Minamidani, T., Kuno, N., et al. 2017, PASJ, 69, 78

Ungerechts, H., Bergin, E. A., Goldsmith, P. F., et al. 1997, ApJ, 482, 245

Valdivia, V., Godard, B., Hennebelle, P., et al. 2017, A&A, 600, A114

van der Wiel, M. H. D., Naylor, D. A., Makiwa, G., Satta, M., & Abergel, A. 2016, A&A, 593, A37

Widicus Weaver, S. L., Laas, J. C., Zou, L., et al. 2017, ApJS, 232, 3

Wiesemeyer, H., Güsten, R., Menten, K. M., et al. 2018, A&A, 612, A37

Appendix A: Channel-wise column density spectra of the detected molecular species

Figures A.1–A.5 show the column density per velocity interval for each detected molecular species in each observed source.
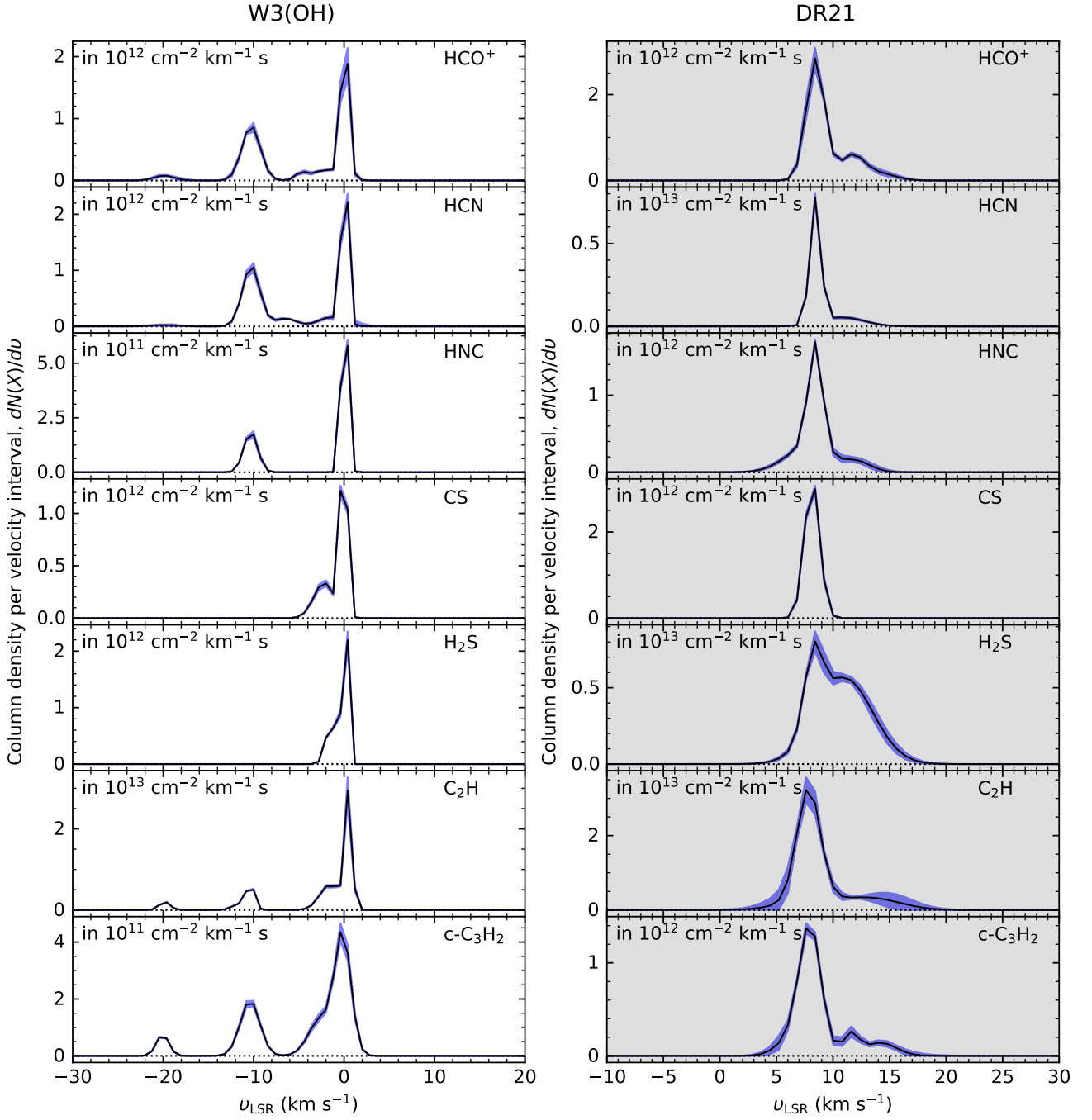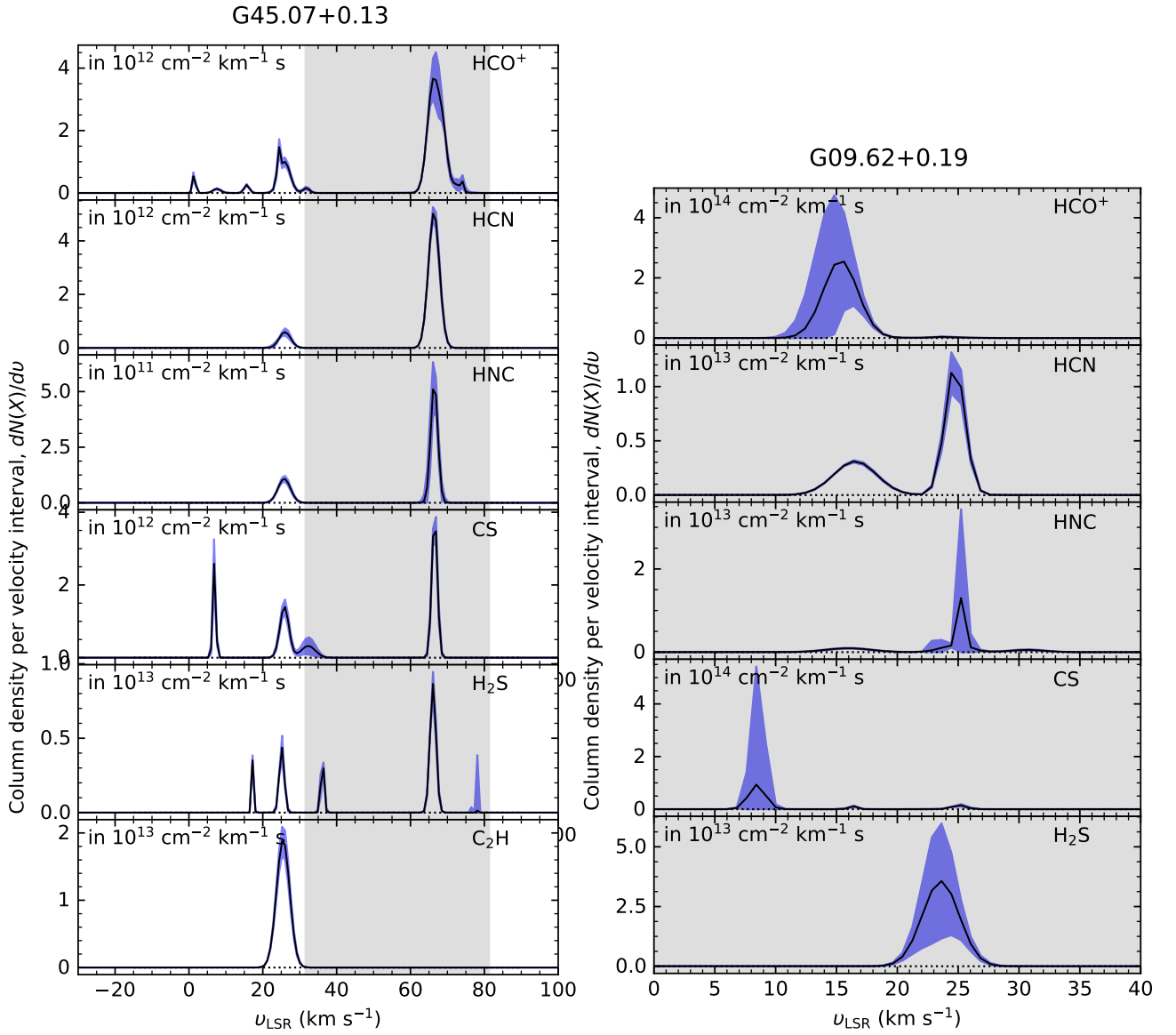

Fig. A.1: Channel-wise column density spectra (dN/dv) as a function of velocity toward W3(OH) and DR21. The dN/dv in each panel shows HCO$^+$, HCN, HNC, CS, H$_2$S, C$_2$H, and c-C$_3$H$_2$ from top to bottom. The gray shaded area indicates dispersion of HCO$^+$ emission lines from continuum sources, and the blue shaded regions represent 2σ confidence intervals for the derived column densities (per velocity interval).
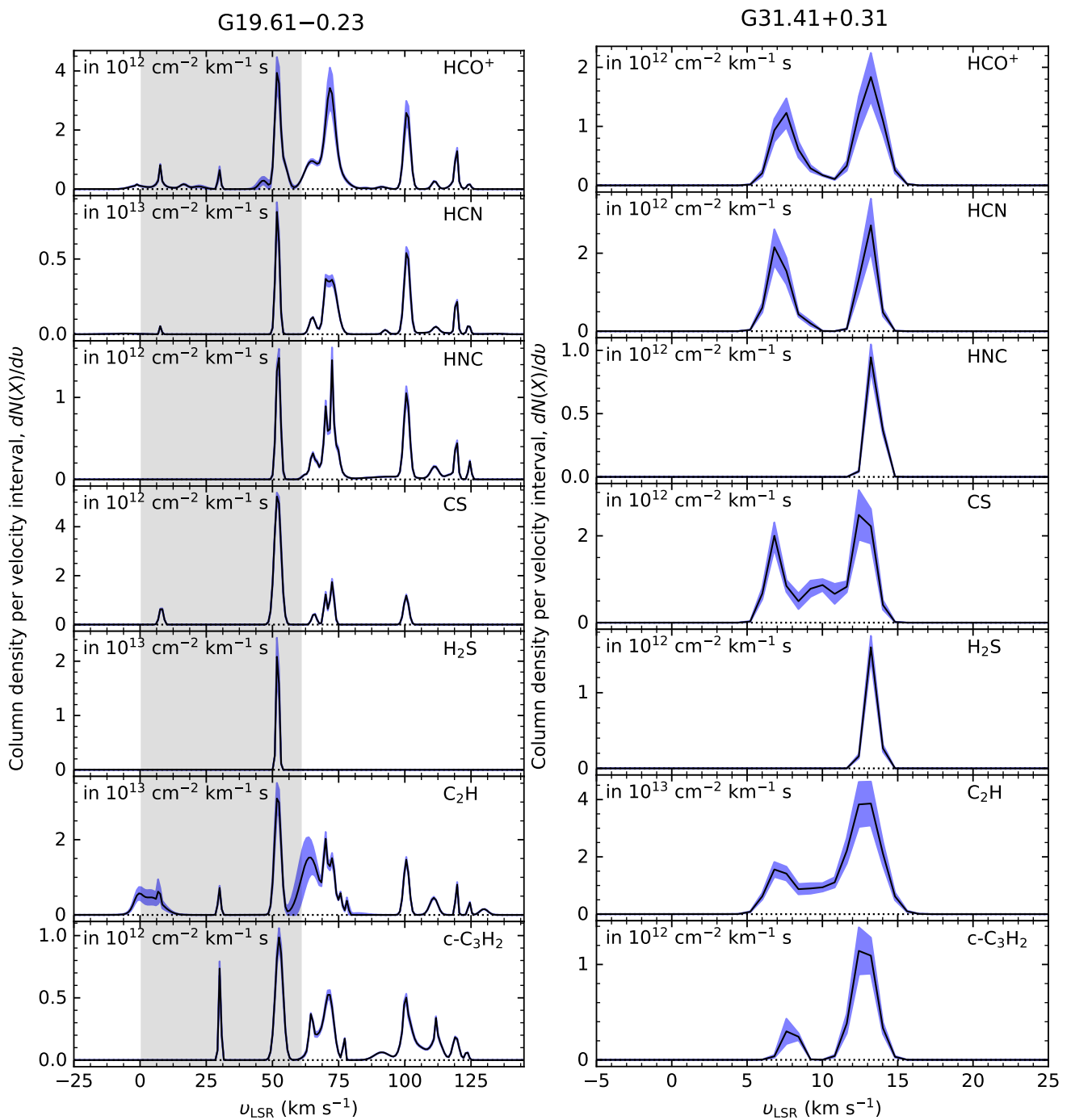
Fig. A.2: Channel-wise column density spectra (dN/dv) as a function of velocity toward G19.61−0.23 and G31.41+0.31 The dN/dv in each panel shows HCO$^+$, HCN, HNC, CS, H$_2$S, C$_2$H, and c-C$_3$H$_2$ from top to bottom. The gray shaded area indicates dispersion of HCO$^+$ emission lines from continuum sources, and the blue shaded regions represent 2σ confidence intervals for the derived column densities (per velocity interval).

Fig. A.3: Channel-wise column density spectra (dN/dv) as a function of velocity toward G45.07+0.13 and G09.62+0.19. The dN/dv in each panel shows HCO$^+$, HCN, HNC, CS, H$_2$S, and C$_2$H from top to bottom, but no C$_2$H toward G09.62+0.19. The gray shaded area indicates dispersion of HCO$^+$ emission lines from continuum sources, and the blue shaded regions represent 2σ confidence intervals for the derived column densities (per velocity interval).

Fig. A.4: Channel-wise column density spectra (dN/dv) as a function of velocity toward W43 MM1 and NGC 6334 I. The dN/dv in each panel shows HCO^+, HCN, HNC, CS, and H_2S from top to bottom. The gray shaded area indicates dispersion of HCO^+ emission lines from continuum sources, and the blue shaded regions represent 2σ confidence intervals for the derived column densities (per velocity interval).
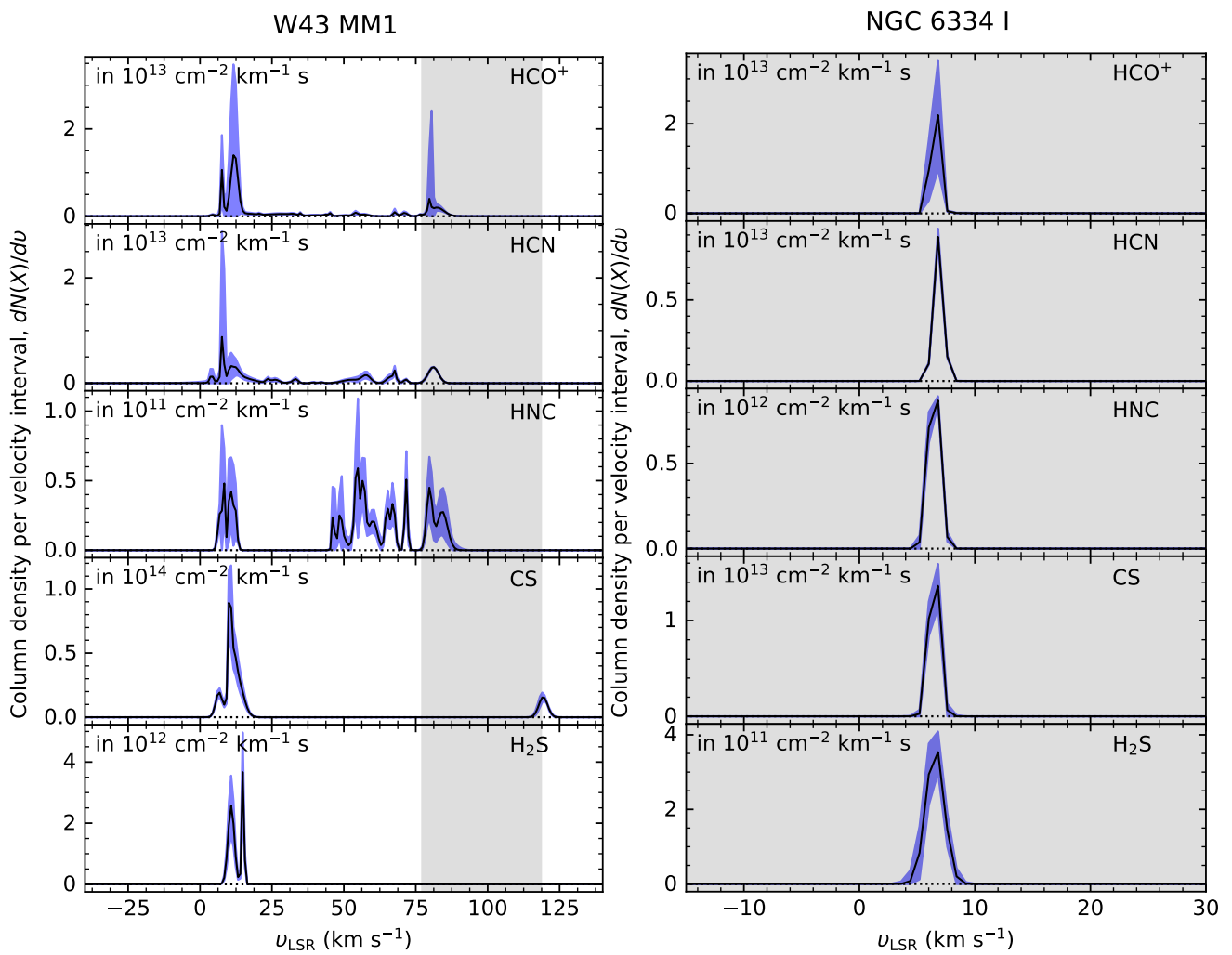
Fig. A.5: Channel-wise column density spectra (dN/dv) as a function of velocity toward NGC 7538 IRS1, HGAL0.55−0.85, and W3 IRS5. Toward NGC 7538 IRS1 and HGAL0.55−0.85, HCO$^+$ is only detected. For W3 IRS5, the dN/dv in each panel shows HCO$^+$, HCN, C$_2$H, and c-C$_3$H$_2$ from top to bottom. The gray shaded area indicates dispersion of HCO$^+$ emission lines from continuum sources, and the blue shaded regions represent 2σ confidence intervals for the derived column densities (per velocity interval).
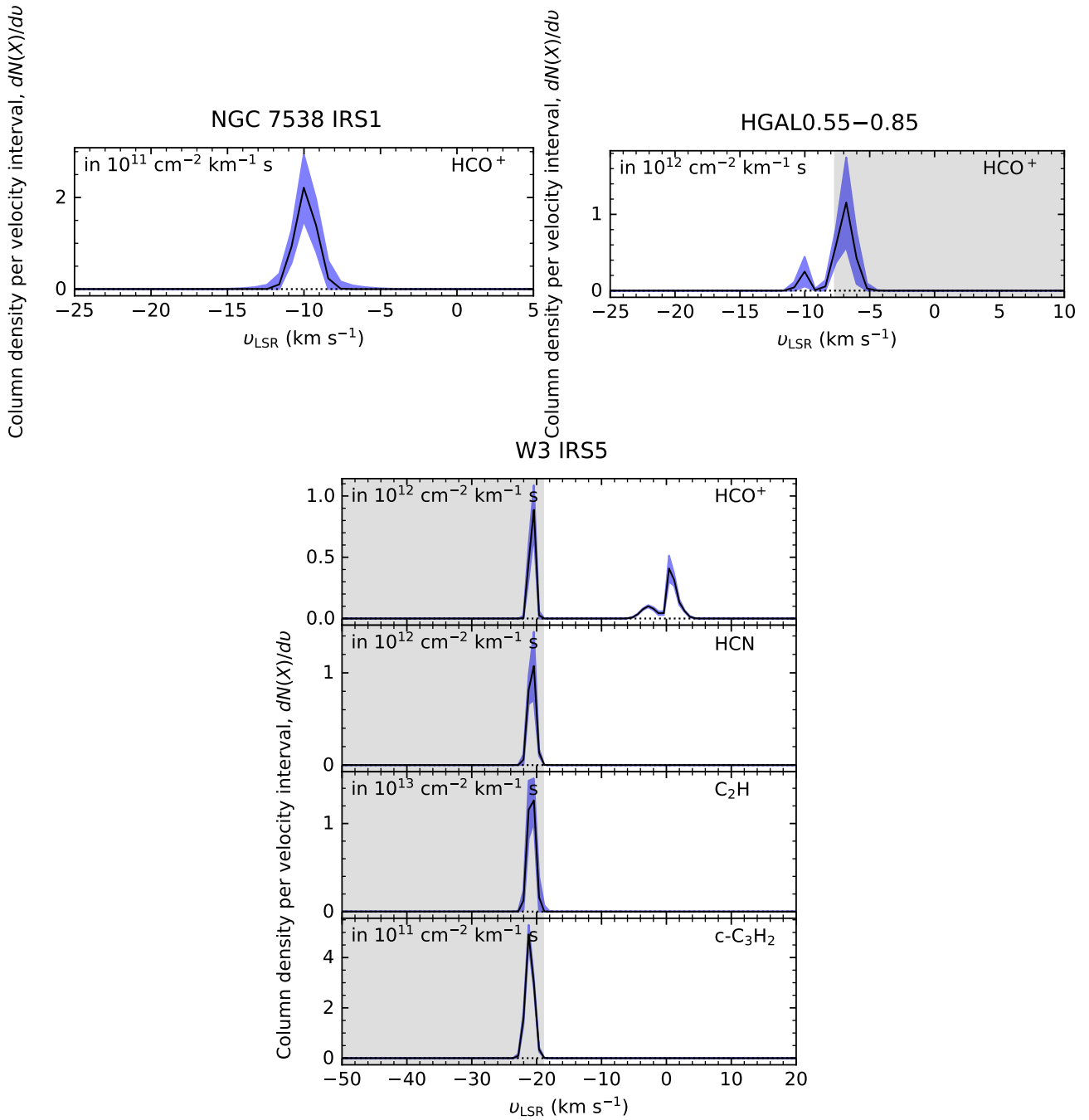
# Appendix B: Derived column densities of the detected molecular species

Table B.1 lists integrated column densities over given velocity interval for each detected molecule in each observed source.

Table B.1: Continuation of Table 8.

Source	v_{LSR} range (km s⁻¹)	$N(H_2)$ (10^{21}cm⁻²)	$N(HCO^+)$ (10^{12}cm⁻²)	$N(HCN)$ (10^{12}cm⁻²)	$N(HNC)$ (10^{12}cm⁻²)	$N(CS)$ (10^{12}cm⁻²)	$N(H_2S)$ (10^{13}cm⁻²)	$N(C_2H)$ (10^{13}cm⁻²)	$N(c\text{-}C_3H_2)$ (10^{12}cm⁻²)
G19.61−0.23	−10, 4	$0.30^{+0.04}_{-0.04}$	$0.90^{+0.13}_{-0.13}$	$0.48^{+0.01}_{-0.01}$	⋯	⋯	⋯	$3.62^{+1.22}_{-1.22}$	⋯
	4, 12	$0.55^{+0.05}_{-0.05}$	$1.66^{+0.15}_{-0.15}$	$0.55^{+0.01}_{-0.01}$	⋯	$1.36^{+0.07}_{-0.07}$	⋯	$2.73^{+1.08}_{-1.08}$	⋯
	14, 19	$0.21^{+0.03}_{-0.03}$	$0.62^{+0.08}_{-0.08}$	⋯	⋯	⋯	⋯	⋯	⋯
	27, 32[a]	$0.28^{+0.06}_{-0.06}$	$0.83^{+0.18}_{-0.18}$	⋯	⋯	⋯	⋯	$0.92^{+0.08}_{-0.08}$	$0.81^{+0.07}_{-0.07}$
	48, 58	$2.62^{+0.29}_{-0.30}$	$12.69^{+1.68}_{-1.68}$	$15.68^{+1.56}_{-1.56}$	$3.23^{+0.29}_{-0.29}$	$16.89^{+0.88}_{-0.88}$	$3.23^{+0.51}_{-0.51}$	$10.03^{+1.75}_{-1.58}$	$3.47^{+0.25}_{-0.25}$
	58, 67	$1.14^{+0.07}_{-0.07}$	$4.76^{+0.34}_{-0.34}$	$2.95^{+0.07}_{-0.07}$	$0.89^{+0.07}_{-0.07}$	$0.80^{+0.05}_{-0.05}$	⋯	$9.51^{+4.43}_{-4.37}$	$0.99^{+0.07}_{-0.07}$
	67, 75	$3.46^{+0.46}_{-0.47}$	$17.59^{+2.81}_{-2.81}$	$20.36^{+1.62}_{-1.62}$	$4.82^{+0.41}_{-0.41}$	$5.43^{+0.51}_{-0.51}$	⋯	$10.20^{+1.03}_{-1.03}$	$2.75^{+0.19}_{-0.19}$
	75, 82	$0.65^{+0.08}_{-0.08}$	$1.95^{+0.24}_{-0.24}$	$1.28^{+0.05}_{-0.05}$	$0.34^{+0.02}_{-0.02}$	⋯	⋯	$1.18^{+0.38}_{-0.26}$	$0.23^{+0.01}_{-0.01}$
	87, 93	$0.10^{+0.02}_{-0.02}$	$0.30^{+0.07}_{-0.07}$	$0.47^{+0.01}_{-0.01}$	$0.19^{+0.01}_{-0.01}$	⋯	⋯	⋯	$0.30^{+0.01}_{-0.01}$
	93, 106	$1.80^{+0.22}_{-0.22}$ [b]	$8.12^{+1.16}_{-1.16}$	$15.85^{+1.55}_{-1.55}$	$3.13^{+0.25}_{-0.25}$	$2.87^{+0.19}_{-0.19}$	⋯	$3.80^{+0.19}_{-0.19}$	$2.29^{+0.14}_{-0.14}$
	106, 114	$0.25^{+0.02}_{-0.02}$	$0.74^{+0.07}_{-0.07}$	$1.95^{+0.03}_{-0.03}$	$0.63^{+0.04}_{-0.04}$	⋯	⋯	$1.69^{+0.11}_{-0.11}$	$1.16^{+0.06}_{-0.06}$
	114, 122	$0.67^{+0.05}_{-0.05}$ [b]	$2.52^{+0.21}_{-0.21}$	$4.07^{+0.24}_{-0.24}$	$0.98^{+0.06}_{-0.06}$	⋯	⋯	$1.00^{+0.09}_{-0.09}$	$0.70^{+0.03}_{-0.03}$
	122, 127	$0.11^{+0.01}_{-0.01}$ [b]	$0.33^{+0.02}_{-0.02}$	$1.03^{+0.03}_{-0.03}$	$0.3^{+0.02}_{-0.02}$	⋯	⋯	$0.45^{+0.05}_{-0.05}$	⋯
G29.96−0.02	−1, 10	$1.81^{+0.25}_{-0.25}$	$8.22^{+1.34}_{-1.34}$	$13.34^{+3.13}_{-3.13}$	$2.63^{+0.22}_{-0.22}$	$4.67^{+0.44}_{-0.44}$	$1.58^{+0.48}_{-0.48}$	$9.82^{+0.89}_{-0.89}$	$3.71^{+0.23}_{-0.23}$
	10, 14	$0.53^{+0.04}_{-0.04}$	$1.58^{+0.11}_{-0.11}$	$2.14^{+0.21}_{-0.21}$	$0.43^{+0.05}_{-0.05}$	$1.52^{+0.13}_{-0.13}$	⋯	$3.71^{+0.43}_{-0.43}$	$1.37^{+0.04}_{-0.04}$
	14, 21	$0.15^{+0.02}_{-0.02}$	$0.44^{+0.06}_{-0.06}$	$0.52^{+0.12}_{-0.08}$	⋯	⋯	⋯	$1.12^{+0.22}_{-0.22}$	$0.61^{+0.01}_{-0.01}$
	50, 56	$0.18^{+0.05}_{-0.05}$	$0.53^{+0.14}_{-0.14}$	$0.71^{+0.07}_{-0.07}$	⋯	⋯	⋯	⋯	⋯
	56, 64	$0.42^{+0.10}_{-0.10}$	$1.25^{+0.29}_{-0.29}$	$1.54^{+0.17}_{-0.17}$	$0.17^{+0.02}_{-0.02}$	⋯	⋯	⋯	⋯
	64, 74	$1.08^{+0.14}_{-0.14}$	$4.47^{+0.68}_{-0.68}$	$7.47^{+0.64}_{-0.64}$	$1.01^{+0.07}_{-0.07}$	⋯	⋯	$3.50^{+0.54}_{-0.54}$	⋯
	74, 79	$0.12^{+0.04}_{-0.04}$	$0.37^{+0.13}_{-0.12}$	⋯	⋯	⋯	⋯	⋯	⋯
W43 MM1	1, 9	$2.40^{+1.72}_{-1.74}$	$11.46^{+10.23}_{-8.95}$	$13.81^{+35.52}_{-13.81}$	$0.92^{+0.80}_{-0.53}$	⋯	⋯	$5.89^{+1.10}_{-1.10}$	⋯
	9, 13	$6.02^{+7.27}_{-6.02}$	$33.88^{+52.39}_{-33.88}$	$10.65^{+8.42}_{-8.01}$	$1.18^{+0.91}_{-0.90}$	⋯	⋯	$23.22^{+7.49}_{-7.49}$	$6.57^{+2.53}_{-2.53}$
	13, 21	$2.81^{+1.84}_{-2.03}$	$13.79^{+11.17}_{-10.73}$	$8.66^{+3.81}_{-3.81}$	⋯	⋯	⋯	$8.66^{+2.66}_{-2.66}$	$4.03^{+1.43}_{-1.43}$
	21, 27	$0.73^{+0.21}_{-0.22}$	$2.81^{+0.98}_{-0.98}$	$3.47^{+1.7}_{-1.7}$	⋯	⋯	⋯	⋯	⋯
	27, 39	$1.16^{+0.30}_{-0.31}$	$4.85^{+1.51}_{-1.51}$	$2.65^{+1.18}_{-1.17}$	⋯	⋯	⋯	⋯	⋯
	39, 47	$0.64^{+0.16}_{-0.17}$	$2.42^{+0.74}_{-0.74}$	$0.66^{+0.46}_{-0.66}$	$0.30^{+0.44}_{-0.30}$	⋯	⋯	⋯	⋯
	47, 61[a]	$0.99^{+0.33}_{-0.35}$	$4.01^{+1.64}_{-1.64}$	$10.24^{+4.82}_{-4.82}$	$3.34^{+1.93}_{-1.84}$	⋯	⋯	⋯	⋯
	61, 69[a]	$0.5^{+0.33}_{-0.33}$	$1.50^{+0.99}_{-0.99}$	$6.27^{+2.89}_{-2.82}$	$1.39^{+0.59}_{-0.58}$	⋯	⋯	⋯	⋯
	69, 75[a]	$0.55^{+0.20}_{-0.22}$	$2.01^{+0.90}_{-0.90}$	$1.53^{+0.65}_{-0.58}$	$0.62^{+0.26}_{-0.26}$	⋯	⋯	⋯	⋯
	75, 87[a]	$3.09^{+4.86}_{-1.68}$	$15.40^{+31.62}_{-9.30}$	$13.64^{+0.89}_{-0.89}$	$2.23^{+1.30}_{-1.30}$	⋯	⋯	⋯	⋯
G31.41+0.31	3, 10	$0.69^{+0.12}_{-0.12}$	$2.63^{+0.55}_{-0.55}$	$3.97^{+0.83}_{-0.83}$	⋯	$3.85^{+0.76}_{-0.76}$	⋯	$4.36^{+0.79}_{-0.79}$	$0.47^{+0.15}_{-0.47}$
	10, 18	$0.99^{+0.18}_{-0.19}$	$4.03^{+0.88}_{-0.88}$	$3.68^{+0.92}_{-0.92}$	$1.09^{+0.11}_{-0.11}$	$5.98^{+1.25}_{-1.25}$	$0.16^{+0.02}_{-0.02}$	$11.83^{+2.30}_{-2.30}$	$2.42^{+0.49}_{-0.49}$
G32.80+0.19	4, 7	$0.57^{+0.01}_{-0.01}$	$1.72^{+0.03}_{-0.03}$	$3.00^{+0.04}_{-0.04}$	⋯	⋯	⋯	$2.08^{+0.12}_{-0.12}$	$0.70^{+0.04}_{-0.04}$
	7, 15	$1.74^{+0.05}_{-0.05}$	$7.81^{+0.25}_{-0.25}$	$8.15^{+0.13}_{-0.13}$	⋯	⋯	⋯	$0.93^{+0.06}_{-0.06}$	$0.86^{+0.06}_{-0.06}$
	28, 43	$0.41^{+0.01}_{-0.01}$	$1.22^{+0.01}_{-0.01}$	$1.33^{+0.0}_{-0.0}$	$0.49^{+0.07}_{-0.07}$	⋯	⋯	$4.62^{+0.65}_{-0.65}$	$0.90^{+0.03}_{-0.03}$
	43, 59	$0.82^{+0.02}_{-0.02}$	$3.23^{+0.10}_{-0.10}$	$3.04^{+0.01}_{-0.01}$	$0.06^{+0.04}_{-0.06}$	⋯	⋯	$0.90^{+0.19}_{-0.19}$	$1.67^{+0.08}_{-0.08}$
	59, 77	$1.63^{+0.03}_{-0.03}$	$7.23^{+0.15}_{-0.15}$	$11.47^{+0.04}_{-0.04}$	$2.28^{+0.23}_{-0.23}$	$3.55^{+0.04}_{-0.04}$	$0.63^{+0.02}_{-0.02}$	$6.19^{+0.31}_{-0.31}$	$3.35^{+0.23}_{-0.23}$
	77, 83	$1.36^{+0.03}_{-0.03}$	$5.86^{+0.15}_{-0.15}$	$16.3^{+0.16}_{-0.16}$	$4.51^{+0.71}_{-0.71}$	$4.06^{+0.04}_{-0.04}$	$0.35^{+0.01}_{-0.01}$	$3.86^{+0.24}_{-0.24}$	$1.35^{+0.23}_{-0.23}$
	83, 87	$1.69^{+0.16}_{-0.16}$	$7.58^{+0.85}_{-0.85}$	$31.1^{+0.30}_{-0.30}$	$6.62^{+1.90}_{-1.90}$	$17.8^{+0.34}_{-0.34}$	$1.73^{+0.19}_{-0.19}$	$5.66^{+0.53}_{-0.53}$	$1.51^{+0.22}_{-0.22}$
	87, 92	$3.14^{+0.10}_{-0.10}$	$15.69^{+0.59}_{-0.59}$	$29.97^{+0.22}_{-0.22}$	$5.22^{+0.59}_{-0.59}$	$9.57^{+0.12}_{-0.12}$	$1.19^{+0.10}_{-0.10}$	$10.99^{+0.8}_{-0.8}$	$3.70^{+0.30}_{-0.30}$
	92, 101	$1.10^{+0.03}_{-0.03}$	$4.57^{+0.14}_{-0.14}$	$3.46^{+0.01}_{-0.01}$	$0.36^{+0.03}_{-0.03}$	$0.58^{+0.04}_{-0.04}$	⋯	$5.41^{+0.29}_{-0.29}$	$1.25^{+0.06}_{-0.06}$
	101, 109	$0.16^{+0.01}_{-0.01}$	$0.49^{+0.01}_{-0.01}$	$0.44^{+0.01}_{-0.01}$	⋯	⋯	⋯	$0.41^{+0.13}_{-0.12}$	$0.31^{+0.02}_{-0.02}$
G45.07+0.13	−1, 3	$0.21^{+0.05}_{-0.05}$	$0.62^{+0.15}_{-0.15}$	⋯	⋯	⋯	⋯	⋯	⋯
	3, 11	$0.12^{+0.03}_{-0.03}$	$0.35^{+0.08}_{-0.08}$	⋯	⋯	$2.62^{+0.77}_{-0.75}$	⋯	⋯	⋯
	12, 19	$0.15^{+0.03}_{-0.03}$	$0.45^{+0.09}_{-0.09}$	⋯	⋯	⋯	$0.29^{+0.03}_{-0.03}$	⋯	⋯
	21, 30	$1.12^{+0.16}_{-0.17}$	$4.66^{+0.81}_{-0.81}$	$2.29^{+0.60}_{-0.57}$	$0.45^{+0.06}_{-0.06}$	$4.41^{+0.85}_{-0.85}$	$0.74^{+0.12}_{-0.12}$	$8.33^{+0.96}_{-0.96}$	⋯
	30, 38	$0.12^{+0.05}_{-0.05}$	$0.36^{+0.15}_{-0.15}$	⋯	⋯	$1.42^{+1.04}_{-1.04}$	$0.40^{+0.12}_{-0.11}$	⋯	⋯
	63, 71[a]	$3.64^{+0.48}_{-0.49}$	$18.71^{+2.91}_{-2.91}$	$18.88^{+1.11}_{-1.11}$	$1.30^{+0.47}_{-0.42}$	$7.37^{+0.93}_{-0.93}$	$1.77^{+0.18}_{-0.18}$	⋯	⋯
	71, 80[a]	$0.34^{+0.24}_{-0.20}$	$1.02^{+0.73}_{-0.59}$	⋯	⋯	⋯	⋯	⋯	⋯
DR21	0, 10[a]	$1.38^{+0.10}_{-0.10}$	$5.93^{+0.53}_{-0.53}$	$10.08^{+0.36}_{-0.36}$	$3.68^{+0.17}_{-0.17}$	$5.38^{+0.21}_{-0.21}$	$2.38^{+0.20}_{-0.20}$	$9.29^{+1.71}_{-1.54}$	$3.83^{+0.33}_{-0.32}$
	10, 17[a]	$0.65^{+0.09}_{-0.09}$	$1.96^{+0.27}_{-0.27}$	$1.52^{+0.18}_{-0.18}$	$0.52^{+0.17}_{-0.16}$	⋯	$2.06^{+0.21}_{-0.21}$	$1.86^{+0.81}_{-0.78}$	$0.89^{+0.22}_{-0.22}$
NGC 7538 IRS1	−13, −5	$0.13^{+0.07}_{-0.05}$	$0.39^{+0.22}_{-0.16}$	⋯	⋯	⋯	⋯	⋯	⋯

## Appendix C: Principal component analysis toward W3 IRS5

Figure C.1 shows the principal components in the left panel, and in the right panel, the rescaled column density profiles of observed absorption line (black curves) and the reproduced column density profiles (red and blue dotted lines) for each detected species, toward W3 IRS5.
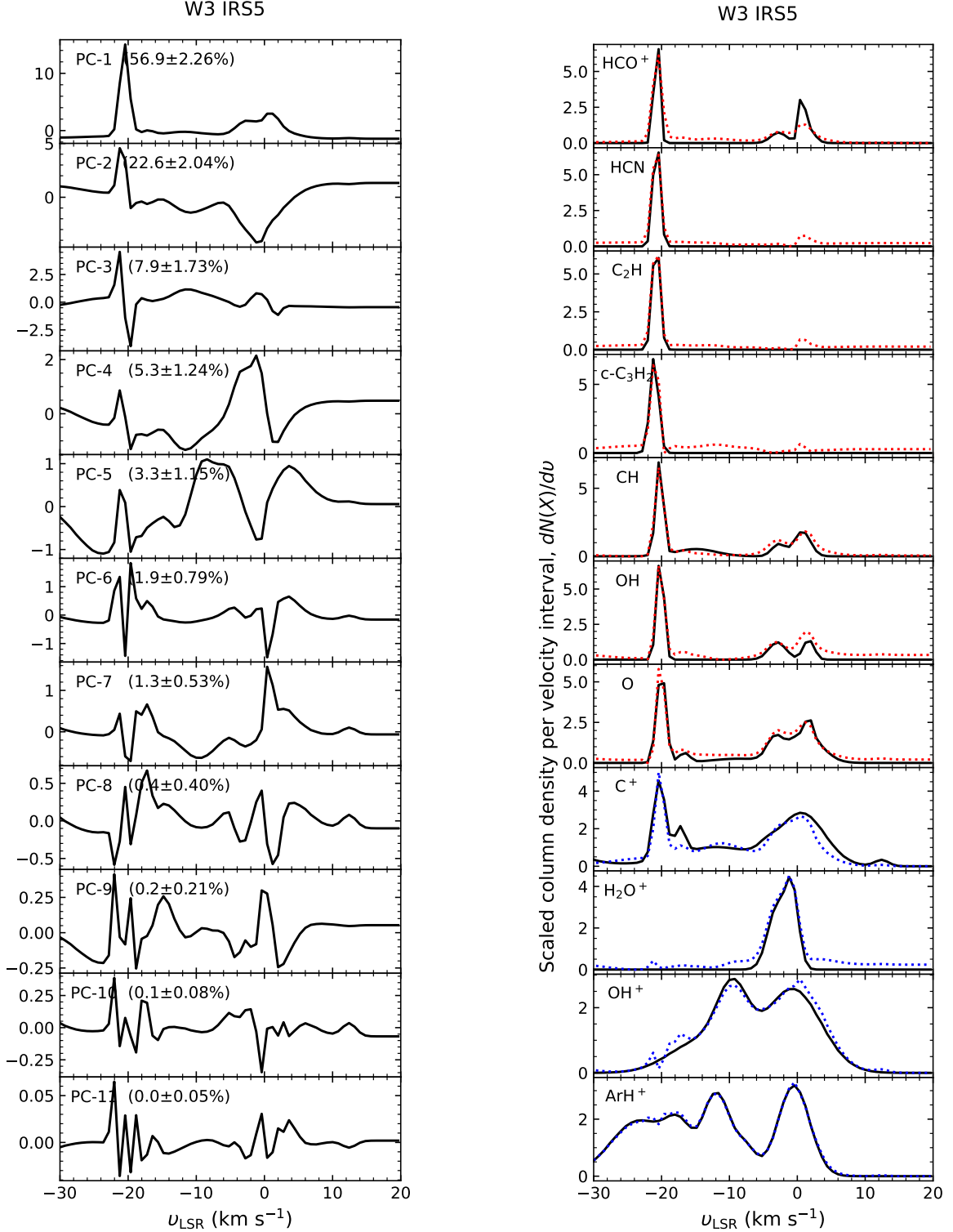
Fig. C.1: *Left*: Eigen spectra of the eleven principle components with percentage of variances as well as uncertainties, toward W3 IRS5. *Right*: Scaled channel-wise column density spectra of the eleven species (HCO^+, HCN, C_2H, $c-C_3H_2$, CH, OH, O, C^+, H_2O^+, OH^+, and ArH^+) as a function of v_{LSR}. Black curves represent the observational data, and red dotted curves are the spectra reproduced with only the first three principal components (PC-1, PC-2, and PC-3). For C^+, H_2O^+, OH^+, and ArH^+, the reproduced spectra indicated by blue dotted curves include one or two more PCs, i.e., PC-4 and PC-5.

Appendix D: H-plots for the ten considered species (HCO⁺, HCN, C₂H, c-C₃H₂, CH, OH, O, C⁺, H₂O⁺, and OH⁺) toward W3(OH) and W3 IRS5

Figure D.1 shows the h-plots for ten considered species toward W3(OH) and W3 IRS5 as like as Figs. 13 and 14, but these h-plots only consider ten species that are commonly detected toward these two sightlines.
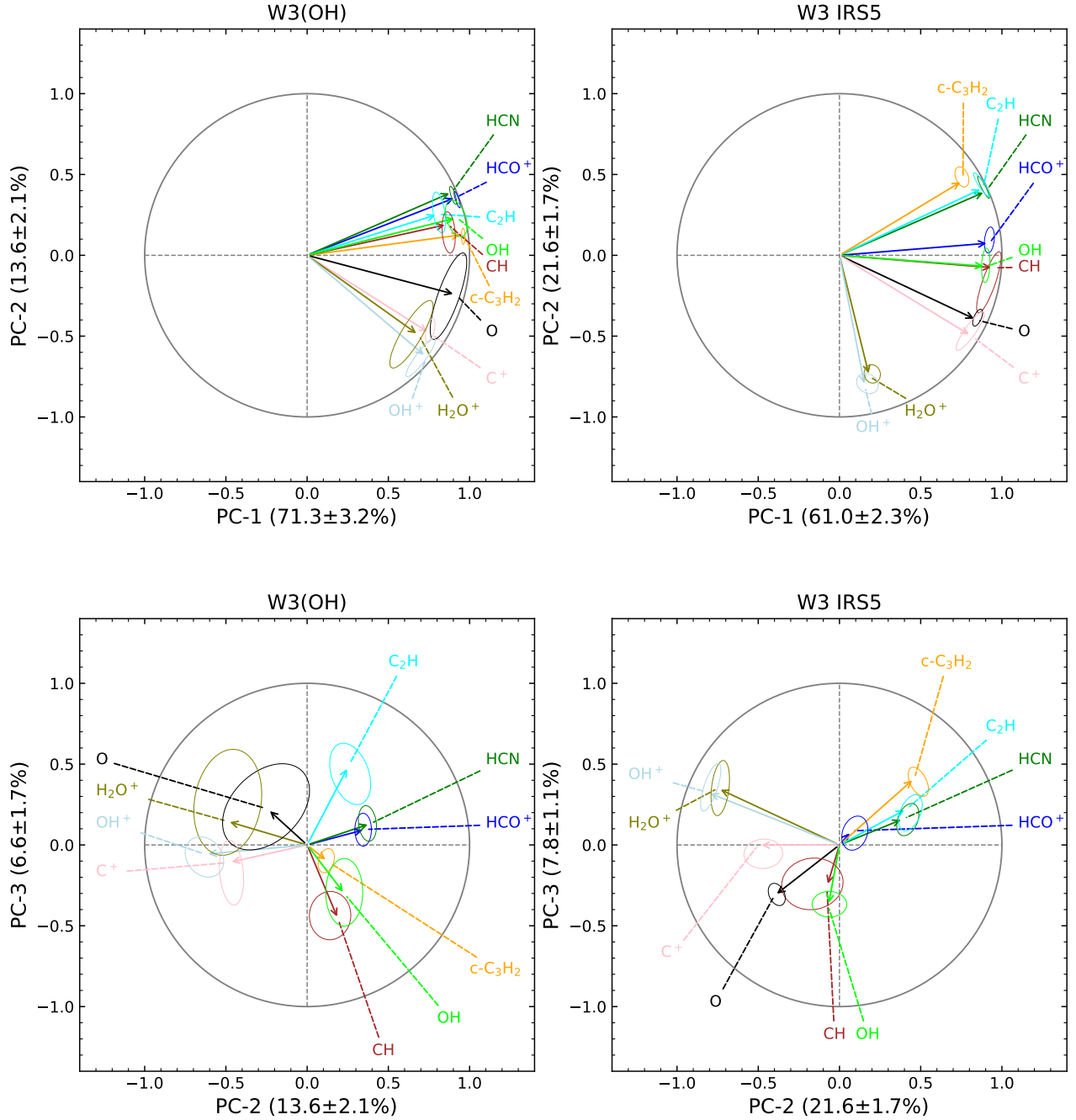
Fig. D.1: *Upper*: Variable correlation circle plots for the first and second PCs toward W3(OH) in the left panel and W3 IRS5 in the right panel. The solid straight lines close to the unit circle imply PC-1 and PC-2 contain the most information about the variables. Different colors are used to denote the different species analyzed. Each colored ellipse is a 2σ confidence interval for the uncertainty of the PCA results for the corresponding species. *Lower*: Same as the upper panel but for the second and third PCs (PC-2 and PC-3) toward the same sources, from left to right.

Appendix E: Variations of $N(H_2)$ and $N(X)/N(H_2)$ ratios

Figures E.1 and E.2 show variations in molecular abundance relative to $N(H_2)$ in the lower panel and $N(H_2)$ in the upper panel as a function of velocity in each source.
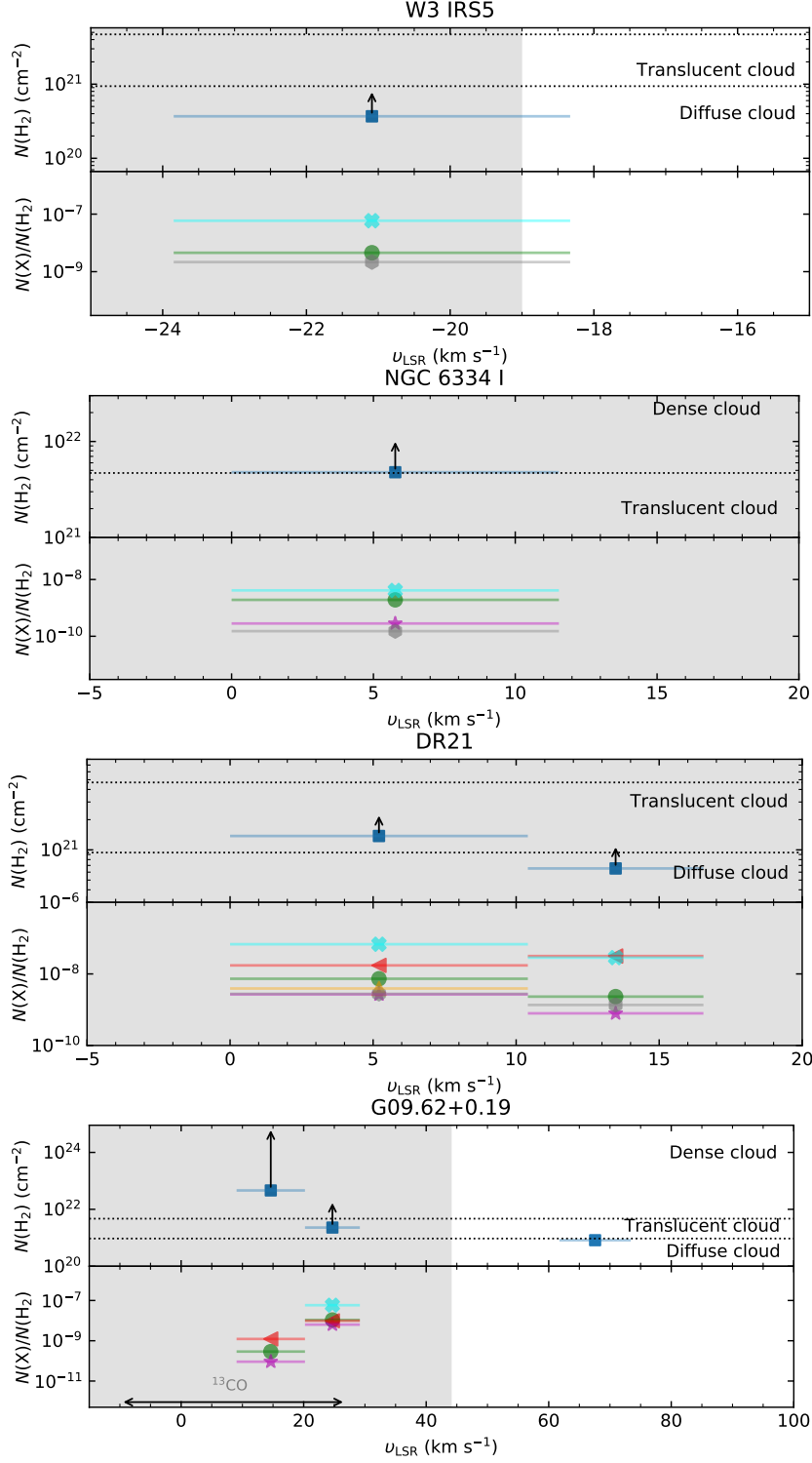
Fig. E.1: $N(H_2)$ and $N(X)/N(H_2)$ ratio integrated over specific velocity intervals from top to bottom toward W3 IRS5, NGC 6334 I, DR21, and G09.62+0.19. Different species are labeled with different symbols and colors as shown in the legend displayed in the right corner of the W3(OH) diagram. The gray areas indicate the velocity ranges of the emission lines. In the upper panels, the dotted horizontal lines correspond to A_v of 1 and 5, respectively. In the lower panels, the black horizontal arrows indicate the velocity ranges in which CO emission features have been detected from archival data at its given sensitivity.
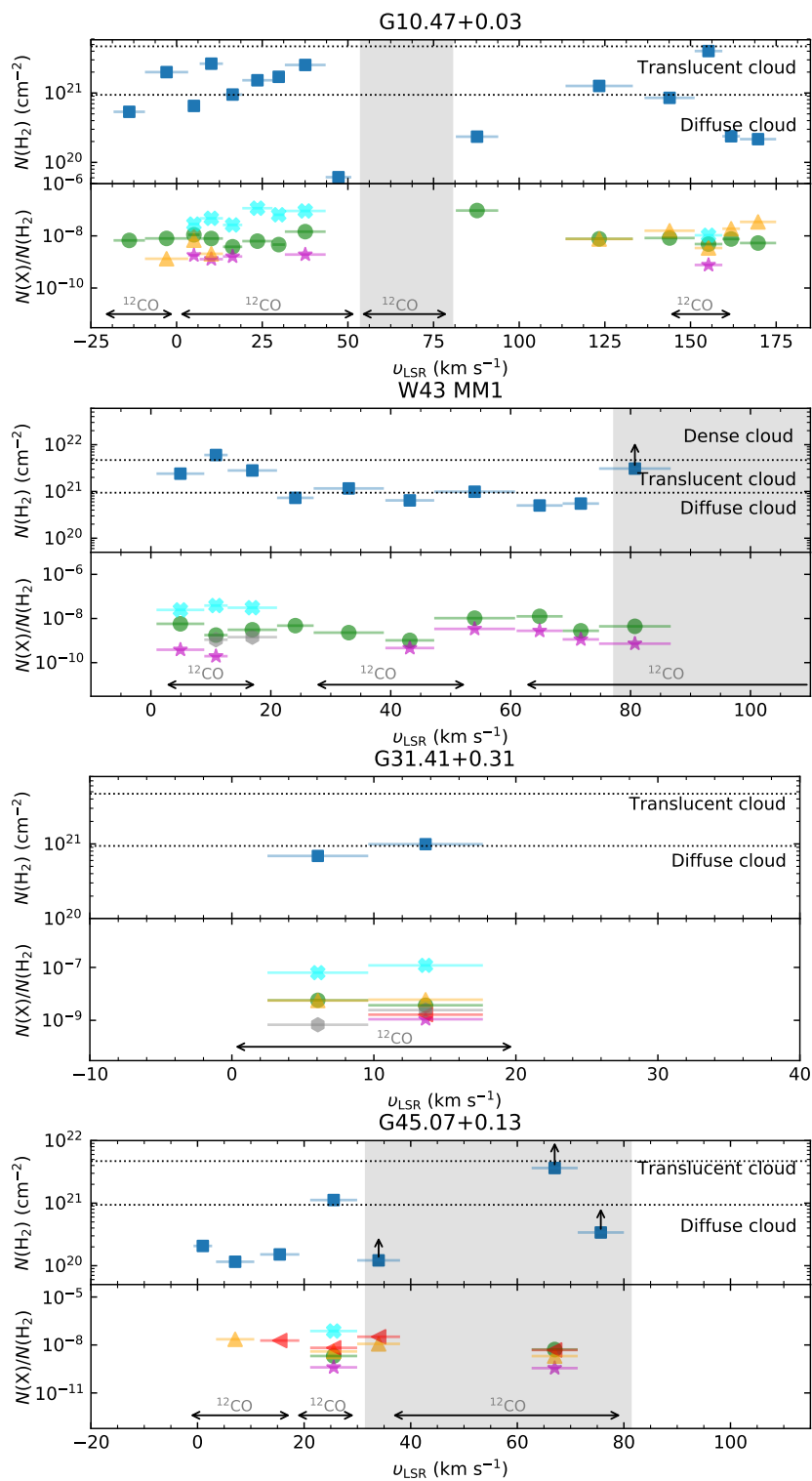
Fig. E.2: $N(H_2)$ and $N(X)/N(H_2)$ ratio integrated over specific velocity intervals from top to bottom, toward G10.47+0.03, W43 MM1, G31.41+0.31, and G45.07+0.13. All symbols and lines are same as Fig. E.1.